DEVELOPMENT OF A DEVICE FOR T-WAVE FEATURE EXTRACTION AND RAPID BASELINE NULLING

By

DAVID WINFIELD SMITH

A thesis submitted to the

Graduate School-New Brunswick

Rutgers, The State University of New Jersey

and

The Graduate School of Biomedical Sciences

University of Medicine and Dentistry of New Jersey

in partial fulfillment of the requirements

for the degree of

Master of Science

Graduate Program in Biomedical Engineering

written under the direction of

Dr. John K-J. Li

and approved by

_____

_____

_____

New Brunswick, New Jersey

October, 2013

ABSTRACT OF THE THESIS

Development of a Device for T-wave Feature Extraction and Rapid Baseline Nulling

by DAVID WINFIELD SMITH

Thesis Director:

Prof. John K-J. Li

The T-wave of the electrocardiogram electrically represents ventricular repolarization – the relaxation phase of the cardiac cycle. Discrete states of abnormal T-wave morphology are known to be associated with both pathologic and non-pathologic causes. The links between causative factors and morphologic effects, however, are described as sensitive, but not specific. This thesis aimed to develop a device that could accurately quantify the T-wave's characteristic morphologic features on a beat-to-beat basis, in real-time, to improve specificity.

T-wave feature data were extracted with minimal noise using a novel analog electronic device design that allowed corrections for baseline drift and motion artifacts. T-wave morphologies were then approximated by geometric composite figures constructed from each T-wave's constituent data, namely, its height and leading and trailing edge slopes. It was hypothesized that the T-wave approximation figures would convey clinically relevant information to an observer, notwithstanding their composition from highly compressed data.

Simulated T-wave monitor designs were tested on 2,604 T-waves from thirty-two real and synthetic ECG data sources. Results from the study concluded that over 88% of the geometric composite figures were reasonable approximations of T-wave morphology. Noise on the T-wave signal was the primary cause for less-than-reasonable approximations. Feature accuracies were found to have less than 3% error when tested against a smaller subset of 260 T-wave controls. Clinical meaningfulness of the composite figures was demonstrated by observation of T-wave alternans and the effects of oxygen saturation levels on T-wave morphology. Average baseline drift was held to within 0.010 mV across a wide variety of input conditions. Complete transient response recovery from ±300 mV input pulses sometimes occurred in less than one heartbeat.

The present novel methodology employed in the successfully tested T-wave monitor design can be extended to other ECG components, and has the potential to improve the accuracy of arrhythmia detection and classification in future applications.

Acknowledgement

It is with deep appreciation that I extend thanks to my professor and thesis advisor, Dr. John K-J. Li. His shared time, support, faith, expertise, and patience have been instrumental to many of my most meaningful biomedical experiences. In particular, concepts for this thesis were initiated under his direction and completed with the tools and other resources he generously provided. It is hard to overstate their contribution to this effort or my gratitude to Dr. Li for allowing me unfettered access to them.

I sincerely thank the other members of my defense committee, Dr. George K. Shoane and Dr. Gary M. Drzewiecki, for their efforts on my behalf and their support over the past several years. Both have shared their experience and expertise with many and I am honored to be among them. I especially thank Dr. Shoane for acting as my Senior Design advisor. It was a great experience and I learned much.

Along with the late Dr. Evangelia Micheli-Tzanakou, I thank the members of my defense committee and all others who dared to be there during the formative years of the Biomedical Engineering department at Rutgers. Your courage and tenacity added the concrete possibility to my academic dreams.

My thanks also go out to the rest of the Rutgers Biomedical Engineering department faculty, the staff, and my fellow students. I very much appreciate your willing acceptance and unfailing support. Thanks for having me!

Dedication

I dedicate this thesis to my parents, Harold and Jenneth Smith. Their thirst for knowledge was tireless, their supportiveness, endless, and their love, boundless. May I strive to live similarly.

I dedicate my degree to my wife, Heather. Her continued support made this degree possible in spite of the many discouragements and great odds against it. I thank her for her patience and her ongoing efforts. May we now continue our walk together, hand in hand, for all our days to come.

TABLE OF CONTENTS

List of Tables

List of Illustrations

List of Abbreviations

AAMI	Association for the Advancement of Medical Instruments
ANSI	American National Standards Institute
BPM	Beats Per Minute
CAD	Coronary Artery Disease
CMR	Common-Mode Rejection
CMV	Common-Mode Voltage
CO	Cardiac Output
DA	Difference Amplifier
ECG	Electrocardiograph
EDV	End Diastolic Volume
GA	Gain Amplifier
HPF	High-pass Filter
HR	Heart Rate
IA	Instrumentation Amplifier
LA	Left Arm
LBBB	Left Bundle Branch Block
LPF	Low-pass Filter
MTWA	Microvolt T-wave Alternans
RA	Right Arm
RFI	Radio Frequency Interference
RLD	Right-Leg Drive
S&H	Sample and Hold

SCD	Sudden Cardiac Death
SV	Stroke Volume
TWA	T-wave Alternans
VF	Ventricular Fibrillation
VT	Ventricular Tachycardia

CHAPTER 1

1. INTRODUCTION

1.1. Background

Perhaps second only to the stethoscope, the electrocardiograph (ECG) is one of the most widely used and universally recognized medical devices in clinical and investigative cardiology (Fuster et al. 2011; Longo et al. 2012). Since the introduction of what is considered modern ECG technology by Willem Einthoven in the early 20th century (1908), ECGs have progressed from having three bipolar (standard) limb leads to those that regularly include twelve or more leads, or axes of cardiac measurement (Malmivuo and Plonsey 1995; Fuster et al. 2011; Macfarlane et al. 2011; Longo et al. 2012). While additional axes can provide a more comprehensive assessment of cardiac function and health, this work will focus primarily on the ECG signals of standard limb leads I and II (Widmaier et al. 2006). More specifically still, the T-wave segment, representing the repolarization of the ventricles, is the portion of the ECG signal under primary investigation here (Widmaier et al. 2006; Fuster et al. 2011; Longo et al. 2012). Figure 1.1 shows a typical ECG record annotated to indicate major features, along with standard intervals and segments [Fig 4-2, h]. Because the presence of morphologic variability within the T-wave segment is considered a clinically relevant indicator of cardiac health, the objective of this research was to develop and test a biomedical device and an associated signal processing algorithm that could be used to quantitatively describe beat-to-beat T-wave morphology, using a significantly reduced data set, in real-time.

Neurological stimulation of contractions within the myocardium – and the relaxations that follow – creates ionic flows that generate electrical fields throughout the body, as if distributed within a volume conductor (Malmivuo and Plonsey 1995; Macfarlane et al. 2011). Localized depolarizations caused by the rapid cellular influx of positive ions (predominantly sodium, Na^+), produce a wave of transient ionic dipoles within the extracellular environment (Widmaier et al. 2006; Mohrman and Heller 2010). The negative ends of the dipoles appear in depolarized regions due to the temporary relative reduction of positive ion concentrations there (Malmivuo and Plonsey 1995; Fuster et al. 2011). The positive ends of the dipoles reside within regions of quiescent (non-depolarized) or repolarized cells (Malmivuo and Plonsey 1995; Fuster et al. 2011). It is the summation of the electrical fields generated by these dipoles that is measured on the surface of the body by the ECG (Malmivuo and Plonsey 1995; Mohrman and Heller 2010).

Because the direction of ventricular myocardial cell depolarization (endocardium to epicardium) is opposite the direction of their repolarization (epicardium to endocardium), the dipole orientation for contraction and relaxation of the ventricles in the normal heart is the same (Malmivuo and Plonsey 1995; Mohrman and Heller 2010; Fuster et al. 2011; Longo et al. 2012). Endocardium cell delay is responsible for the unexpected direction of repolarization (Malmivuo and Plonsey 1995; Mohrman and Heller 2010; Fuster et al. 2011). Therefore, depolarization of the ventricles, as found in the R-wave segment of the ECG signal, and their repolarization, as found in the T-wave segment, normally have the same orientation in leads I and II (Malmivuo and Plonsey 1995; Mohrman and Heller 2010; Longo et al. 2012). By convention, leads I and II are

configured such that normal adult R-wave and T-wave events are both positive with respect to the isoelectric line of the ECG (Mohrman and Heller 2010; Fuster et al. 2011; Longo et al. 2012). Disregarding any noise content in the ECG signal, the isoelectric line is defined as the electrical potential observed during times of little or no myocardial cell activity, and can be assigned sometime between the end of the T-wave and the beginning of the P-wave that follows (Ezenwa et al. 1988; Plonsey 2007; Mohrman and Heller 2010; Fuster et al. 2011). The PR segment and the middle of the ST segment can also be considered isoelectric in normal ECGs (Mohrman and Heller 2010; Fuster et al. 2011).

The body's internal ionic flows can be transduced into electron flows, or currents, at the biologic interface of an electrode applied to the surface of the skin. The conductive contact surface of the electrode is often coated with Ag/AgCl to lower its impedance, along with the associated risks of electrode polarization and subsequent electrode degradation (Malmivuo and Plonsey 1995; Merrill 2005). Ag/AgCl has increased charge density characteristics that reduce the occurrence of destructive, non-reversible, Faradaic charge transfer reactions within the double-layer environment (Malmivuo and Plonsey 1995; Merrill 2005). Use of an electrolytic gel or paste further enhances conduction at the skin-electrode interface (Malmivuo and Plonsey 1995; Macfarlane et al. 2011).

The body's internal impedances are relatively low. For example, non-bone tissues of the thorax have resistivities ranging from about 1.5 Ω-m to 51 Ω-m at typical bioelectric frequencies (for instance, 1 kHz and below) (Malmivuo and Plonsey 1995; Gordon et al. 1998; Macfarlane et al. 2011). The mean internal impedance of the thorax is about 20 Ω (Malmivuo and Plonsey 1995). The skin-electrode impedance, however, is much higher (several kΩ to hundreds of kΩ) and can vary by more than an order of

magnitude from person-to-person (Cardiac 2002; Prutchi and Norris 2005; Diagnostic 2007). The skin-electrode impedance also tends to decrease with time and is highly sensitive to skin preparation techniques, electrode type and location, and any relative motion within the area of contact (Thomas et al. 1979; Öberg 1982; Pandit 1996; Cardiac 2002; Dozio et al. 2007; Macfarlane et al. 2011). Impedance changes at one electrode site relative to another create a differential-mode noise that contributes to ECG baseline drift, or can appear more radically as a motion artifact (Öberg 1982; Sörnmo 1991; Allen et al. 1994; Pandit 1996; Macfarlane et al. 2011). Additionally, inhalation expands the lungs and thorax, increasing their impedance and rhythmically reducing the ECG signal amplitudes with each breath (Smith et al. 1988; Malmivuo and Plonsey 1995; Cardiac 2002; Diagnostic 2007; Verrier et al. 2011). Tissue impedances decrease, however, as signal frequencies increase (Malmivuo and Plonsey 1995; Cardiac 2002; Ruan et al. 2010).

Static skin-electrode impedance differences that inherently exist, along with the dynamics of skin-electrode impedance, cause the electrical signals of the ECG to present variability that extends well beyond the variability found in the ionic signals at their physiologic source. However, impedance is not the only variable influencing the ECG signal. Muscle contractions originating outside the heart generate a wide range of electrical field amplitudes and frequencies throughout the body. Muscle artifacts represent another type of differential-mode noise that can have devastating effects on the integrity of the ECG signal.

Noise originating outside the body, such as noise conducted or radiated from power and transmission sources, can produce either differential-mode or common-mode

noise within the body or within the ECG instrumentation directly. One of the more troublesome of these is AC power-line noise (Pandit 1996). Oscillating at a fundamental frequency of 60 Hz within the United States, noise from power lines is both nearly ubiquitous and highly problematic because its first and second harmonics are both within the 0.05 Hz to 150 Hz frequency range of ECG signals intended for diagnostic use (Johnson et al. 1999; Diagnostic 2007; Fuster et al. 2011). Ambulatory-grade ECG signals, on the other hand, are defined over the more limited range of 0.67 Hz to 40 Hz (Medical 2001; Cardiac 2002). Consequently, ambulatory ECG equipment can use more aggressive low-pass filters to reduce their susceptibility to power-line and other higher frequency noises. Note also that ambulatory ECG equipment can better protect against offset and baseline drift by using more aggressive high-pass filters. In both cases, however, use of more aggressive filtering tends to distort the ECG waveshape morphologies. Higher frequency noises, such as those from computers and radio sources, are farther outside the ECG signal bandwidth and are, therefore, less likely to affect signal quality adversely when properly filtered.

Interference and the signal distortion caused by the noise sources described above combine to reduce T-wave signal integrity. Improper ECG design, for example, designs that use overly aggressive filters, can also adversely affect the integrity of the T-wave signal (Fuster et al. 2011). Implementation of proper noise reduction methods and careful attention to signal pathway design are, therefore, critical steps toward accurate assessment of any T-wave morphologic differences that may be present.

Abnormal changes in T-wave morphology are generally considered sensitive, but rather non-specific indicators of cardiac health, as will be emphasized shortly (Schindler

et al. 2007; Tintinalli et al. 2011). T-wave morphologies (Figure 1.2) are broadly classified as non-inverted (positive), inverted (negative), and biphasic (or diphasic) (Fuster et al. 2011). T-waves of any of these types can be additionally classified as having flattened, peaked, or bimodal characteristics (Fuster et al. 2011). Unfortunately, morphologic differences in the T-wave have overlapping pathologic causes, or can be unrelated to any known pathology (Fuster et al. 2011). Experimental demonstrations, however, have shown that inducing a delay of repolarization in the endocardium produces a peaked and usually taller T-wave (Fuster et al. 2011). Conversely, inducing a delay of repolarization in the epicardium produces a more flattened or negative T-wave (Fuster et al. 2011). Ischemia is the primary clinical cause for either of these repolarization delays and the associated morphologic changes they impose on the T-wave (Fuster et al. 2011). The onset of ischemia also tends to lengthen the QT interval (Fuster et al. 2011).

Persistent or acute ischemia can lead to myocardial infarction. Non-Q-wave infarction presents flattened or negative T-waves along with ST depressions (Fuster et al. 2011; Longo et al. 2012). Q-wave infarction, on the other hand, presents hyperacute T-waves, followed by T-wave inversions (Fuster et al. 2011; Longo et al. 2012). The ST elevations present in Q-wave infarction are pivotal in the diagnostic decision pathway (Fuster et al. 2011; Longo et al. 2012). Sudden loss of coronary blood flow due to thrombotic occlusion is the most common cause of Q-wave infarction (Longo et al. 2012).

Some non-ischemic causes of heightened or peaked T-waves are: 1) normal population variants, 2) athleticism, 3) acute pericarditis, 4) alcoholism, 5) stroke, 6)

moderate left ventricular hypertrophy, 7) hyperkalemia, and 8) advanced atrioventricular block (Fuster et al. 2011; Longo et al. 2012). Non-ischemic causes of flattened or negative T-waves include: 1) normal population variants, 2) athleticism, 3) pericarditis, 4) alcoholism, 5) stroke, 6) secondary effects of left ventricular hypertrophy or left bundle branch block (LBBB), 7) intermittent LBBB, 8) hyperventilation, 9) pulmonary embolism, 10) myocarditis, 11) mitral valve prolapse, 12) myxedema, 13) certain drugs (for example, prenylamine), 14) hypokalemia, and 15) post-tachycardia (Fuster et al. 2011; Longo et al. 2012). Notably, the first six non-ischemic causes in the more-positive T-wave group are the same as those in the more-negative T-wave group, highlighting the problems of diagnosis when using a non-specific indicator.

T-wave alternans (TWA) and microvolt T-wave alternans (MTWA) are subtle beat-to-beat variations in T-wave morphology. In particular, repeating patterns of T-wave amplitude variations seem to be the dominant alternan feature of clinical interest (Smith et al. 1988; Gold et al. 2000; Chow et al. 2006; Myles et al. 2007). At least one study describes alternans having every-other-beat patterns (ABABAB...) as being the first subharmonic manifestation of a period-doubling effect seen in non-linear systems as they advance toward a chaotic (aperiodic) regime (Smith et al. 1988). In the case of the non-linear excitation of the myocardium, possible chaotic regimes include life threatening arrhythmias, such as ventricular tachycardia (VT) and ventricular fibrillation (VF) (Smith et al. 1988; Gold et al. 2000; Fuster et al. 2011; Tintinalli et al. 2011). Sustained episodes of VT or VF sometimes end in sudden cardiac death (SCD), the leading cause of cardiovascular-related mortality (Smith et al. 1988; Gold et al. 2000; Myles et al. 2007; Fuster et al. 2011; Tintinalli et al. 2011). Linking the presence or type of TWA to SCD

would provide a meaningful and non-invasive predictive tool for use in risk stratification and therapeutic routing (Smith et al. 1988; Gold et al. 2000; Kop et al. 2004; Chow et al. 2006; Myles et al. 2007). Unfortunately, not all studies have found significant correlation between the standalone presence of alternans and the clinical predictability of SCD (Myles et al. 2007; Fuster et al. 2011; Tintinalli et al. 2011; Verrier et al. 2011). Additionally, identifying the presence of alternans in the ECG signal typically requires waveform averaging and can include spectral analysis techniques, neither of which is performed in real-time (Kop et al. 2004; Tintinalli et al. 2011; Verrier et al. 2011).

Acute mental stress has been shown to increase the incidence of TWA, particularly in those patients with coronary artery disease (CAD) that also have known vulnerabilities to ventricular arrhythmias (Kop et al. 2004). Increased QT intervals and increased QT variability have been linked to patients with depression and those suffering from panic disorders (Fuster et al. 2011). Therefore, changes in T-wave morphology might also be useful as an indicator of increased levels of non-ischemic mental stress and depression as well as the ischemic stresses caused by exercise or poor cardiac function.

As previously stated, the T-wave electrically represents the ventricular relaxation phase of the cardiac cycle. The ventricular function curve in Figure 1.3 graphically illustrates that end-diastolic volume (EDV) is positively correlated with stroke volume (SV) (Widmaier et al. 2006; Mohrman and Heller 2010; Fuster et al. 2011). Known as the Frank-Starling mechanism, the relationship between EDV and SV results from intrinsic mechanical properties of the cardiac muscles (Widmaier et al. 2006; Mohrman and Heller 2010; Fuster et al. 2011). Experiments have found that pre-stretching the cardiac muscle fiber sarcomeres slightly beyond their nominal lengths of 2.05 μm to

between 2.2 µm and 2.3 µm produces contractions of peak force (Mohrman and Heller 2010; Fuster et al. 2011). Therefore, enhanced diastole filling due to properly timed and executed ventricular relaxation, along with sufficient ventricular compliance, enhances SV and cardiac output (CO), assuming heart rate (HR) is fixed, by the formula (Widmaier et al. 2006; Mohrman and Heller 2010):

$$CO = HR \times SV \tag{1.1}$$

The examples above of known and possible correlations between T-wave morphology and a variety of cardiovascular pathologies and other forms of physiological stress, lend support to the claim that observation and analysis of T-wave morphology provides valuable, non-invasively obtained, investigative and clinical insight. Consequently, further claimed is that obtaining real-time, beat-to-beat quantification of T-wave morphologic features is a worthwhile pursuit, and one that requires the design of a suitable T-wave monitoring device. Presented herein is believed to be a novel design for such a T-wave monitor.

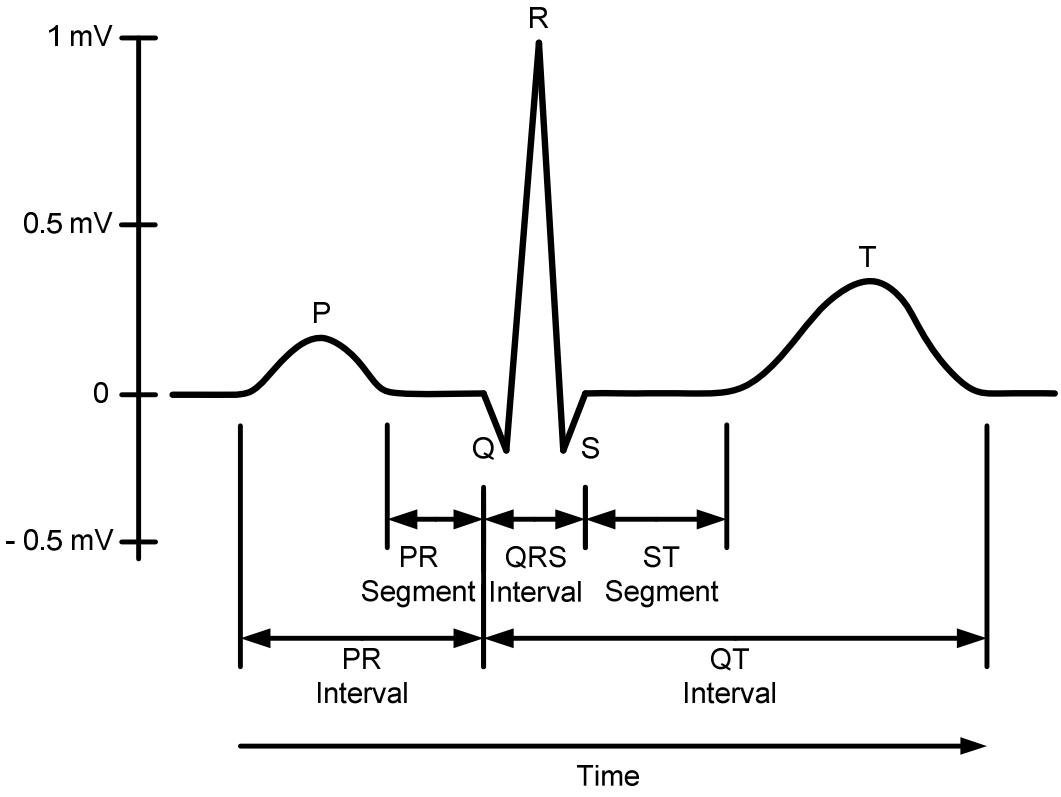

Figure 1.1. Typical electrocardiogram, annotated to show major features, intervals, and segments.

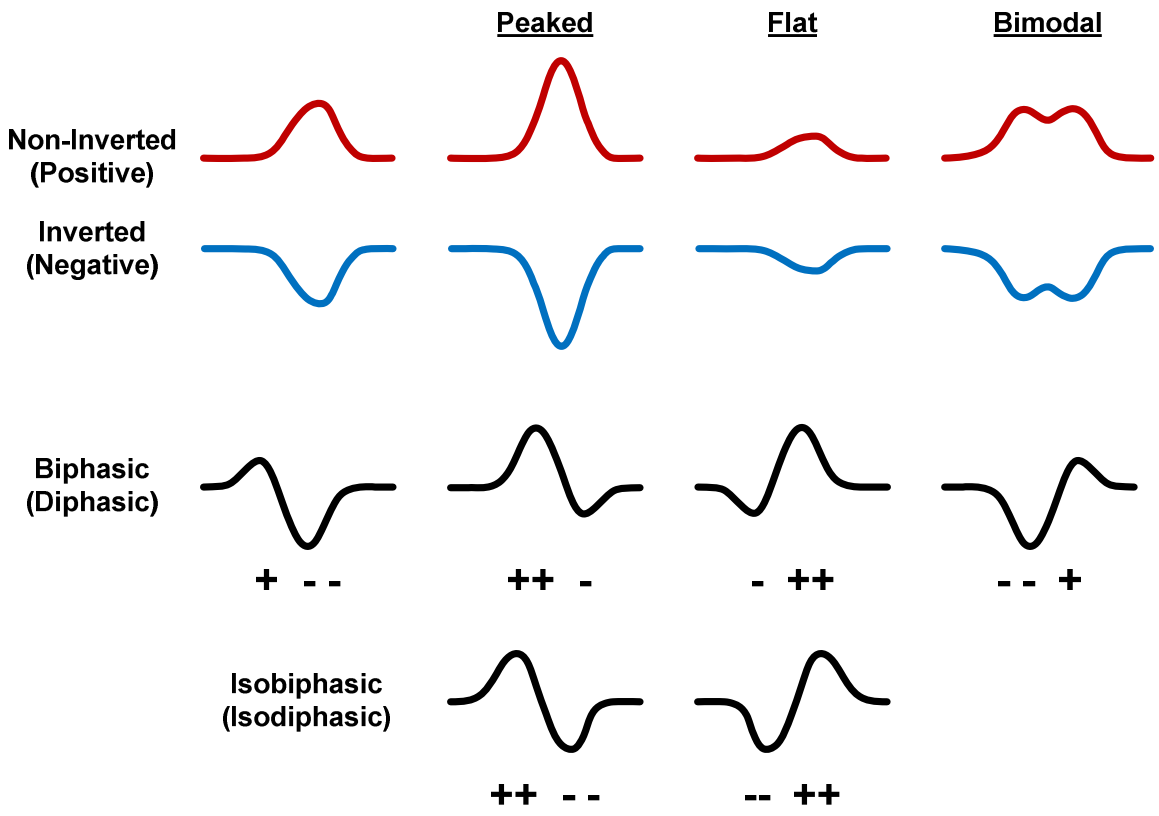

Figure 1.2. Some typical T-wave morphologies.

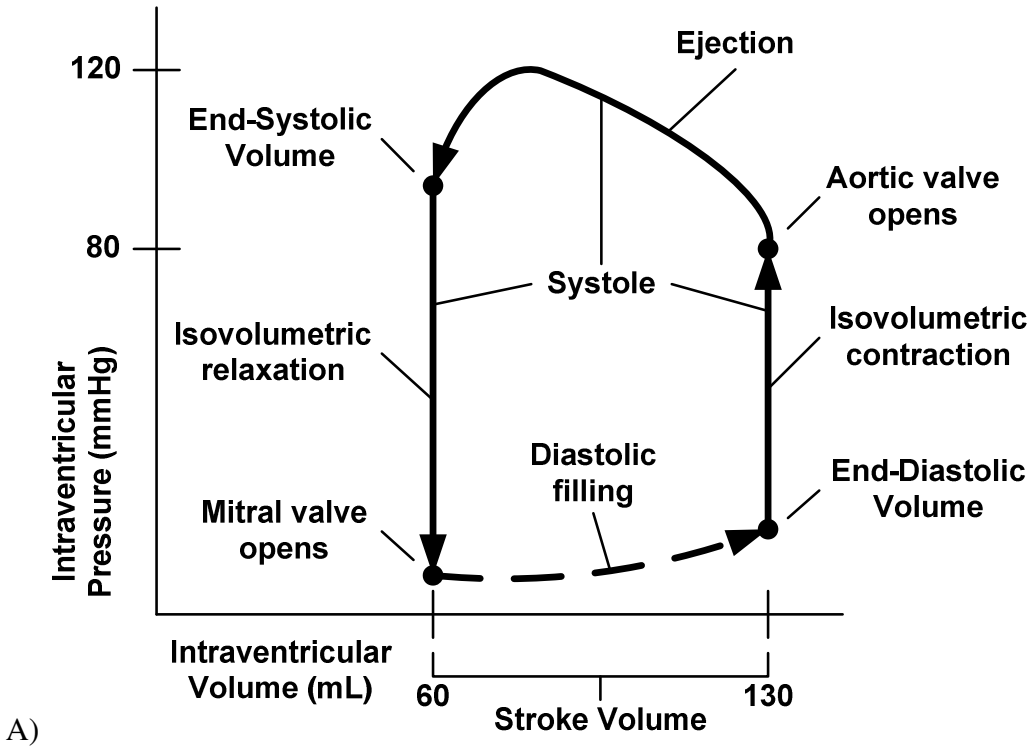

A)

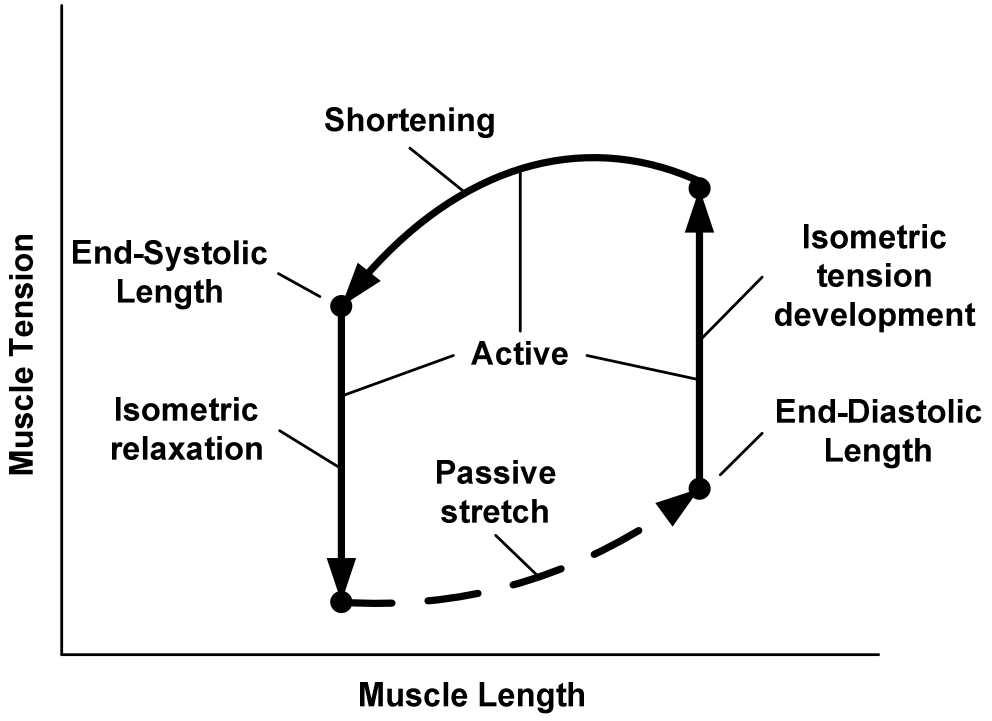

B)

Figure 1.3. A) Left ventricular pressure-volume cycle and B) corresponding muscle length-tension cycle.

1.2. Overview of Design

1.2.1. Motivation

The T-wave and other prominent features of ECG signals are more often described qualitatively than quantitatively in the reference materials reviewed during this research. For example, the evolutionary course of T-wave morphology for a given pathology might be described as proceeding through several characteristic, discrete states exhibiting ST elevation, flattening, inversion, and normalization (Fuster et al. 2011). It is less common to find reference materials that include quantified data describing the precise details of the T-wave for each of these discrete states. It is far less common still to find data describing the transitional phases that occur between each of these T-wave states and their time-course progression.

In some cases, the ECG signals are shown on standard graph grid (1 mm horizontal = 40 ms, 1 mm vertical = 0.1 mV) and, therefore, peak amplitudes and timings can be coarsely determined by graphical observation (Mohrman and Heller 2010). However, even this seemingly rudimentary task becomes tedious after more than just a few heartbeats. Other T-wave features, such as the leading and trailing edge slopes, or the area under the T-wave curve, are more difficult to assess by casual observation. Further, T-wave alternan magnitude variations tend to be very subtle (sometimes in the microvolt range) and so are typically not measurable on the standard ECG grid without a significant degree of interpolation, if visible at all.

The objective, therefore, was to design a T-wave monitor that quantitatively captured a relatively few fundamental beat-to-beat morphological features. It was decided that the four T-wave features of primary interest were: 1) the height, 2) the

dominant leading edge slope, 3) the dominant trailing edge slope, and 4) the area under (or above, if inverted) the T-wave curve, with respect to the isoelectric line. From the magnitudes, signs, and relative timings of the first three of these features, it was hypothesized that a reasonable and meaningful approximation of the T-wave's morphology could be geometrically constructed (Smith et al. 2010). The T-wave approximation would be a composite figure consisting of two trapezoids and a rectangle, combined as shown in Figure 1.4. The area feature captured from the T-wave signal could be useful when assessing whether or not the composite figure reasonably approximates the morphology of the T-wave. For example, if the T-wave signal captured in Lead I or Lead II is normal (non-inverted), then it is expected that the peak amplitude, leading edge slope, and area measurements will have positive signs, and that the trailing edge slope will have a negative sign. If the composite T-wave approximation shares all of these expectations and the calculated area of the geometric figure is similar in magnitude and sign to the actual area measured, it could be said that the geometric approximation is more likely reasonable than if the area metrics did not agree. Of course, other tests are required to determine the integrity of the T-wave approximation more completely. Discussion of the monitor's output algorithm and logic follows in subsequent sections.

Approximation of T-wave morphology using a composite geometric figure derived from just three waveshape features (Figure 1.4) offers the advantage of providing highly compressed and intelligent data for each T-wave event. Generally, finding ways to reduce the amount of data sampled, processed, stored, and transmitted is an important part of a design process. Use of data compression techniques, such as the one developed

here, has the potential to reduce the size, weight, cost, and bandwidth load of the T-wave monitor device, as well as extend the operational lifespan when used in battery-powered applications. For example, at a nominal resting heart rate of 70 BPM, the data, which can include up to twenty (without R-wave min/max data) time and amplitude variables per T-wave event, will be compressed about 21:1 for 250 Hz sample rates and about 86:1 for 1 kHz sample rates. In addition, the data extracted from each T-wave event will have intelligence, meaning that it will include the comparative characteristic magnitudes, signs, and relative timings of the predominant T-wave features. Those tasked with reviewing ECG signals will likely benefit from working with the compressed and intelligent T-wave data output from this design.

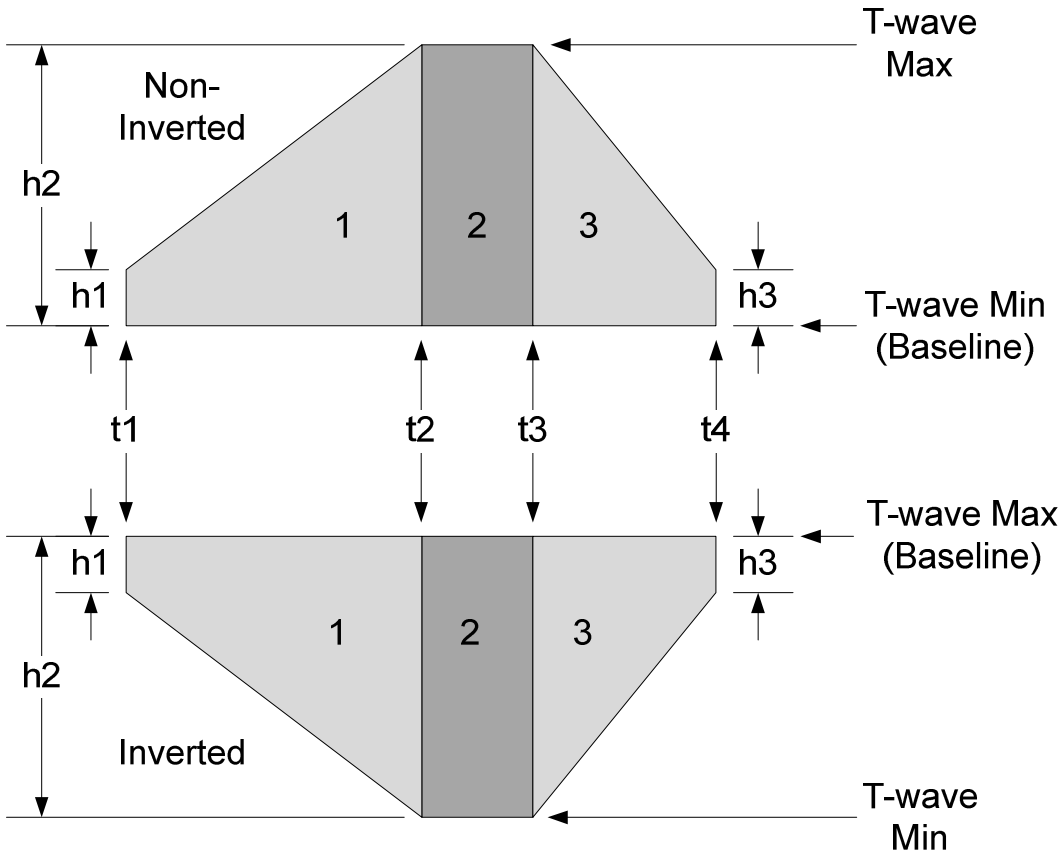

Figure 1.4. Geometric composites used for T-wave approximation.

1.2.2. Hardware

The generalized signal path of the T-wave monitor design is shown in Figure 1.5. As schematically represented, a single bipolar ECG lead is wired across the inputs of two parallel instrumentation amplifiers (IA). IA-1 has a gain of 10 and has a Miller integrator inserted into the positive feedback loop of its integral difference amplifier stage (Sedra and Smith 2004; LT1167 2011). As configured, the Miller integrator is behaving as an inverting, single-pole, low-pass filter (LPF) (Sedra and Smith 2004). Setting the LPF cutoff frequency at about 16 Hz balances the high-frequency noise reduction benefits of signal smoothing with the competing goal of maintaining adequate transient response performance. While inserting the inverting LPF into the positive feedback loop of IA-1's difference amplifier stage produces a high-pass filtering effect on IA-1's output, the output signal of IA-1 is not directly used in the remainder of the design (LT1167 2011). Rather, the output of the inverting LPF is used as the input signal for the Feedback sample and hold (S&H) module. IA-1 also provides the input to a Right-Leg Drive (RLD) circuit. The midpoint value of IA-1's two integral input amplifiers is inverted, amplified, and fed back to the ECG source to improve the common-mode rejection (CMR) of the system. While not shown in Figure 1.5, a shield drive is also provided within the RLD circuit module to reduce potential differential-mode and common-mode errors further.

IA-2 also has a gain of 10 and supplies the ECG signal to the gain amplifier (GA) that follows. Notably, the ECG signal path of IA-2 lacks a continuous high-pass filter (HPF) function. Instead, IA-2 has its Reference pin (REF) wired to the output of the Feedback S&H circuit, one of two S&H modules designed to maintain the ECG baseline

at or near zero volts, relative to the T-wave monitor's power supply potentials. Eliminating continuous high-pass filtering from the ECG signal path avoids filter-imposed distortion of the low frequency content.

The ECG signal of IA-2 passes through the GA where it is amplified about 100 times more. Total signal gain is now around 1,000. A 2-pole, 60 Hz notch filter, with a Q of 0.5, removes much of the first-harmonic power-line noise. A 4-pole Bessel LPF, with a cutoff frequency of 40 Hz, removes additional high frequency noise components. The output of the 4-pole Bessel LPF passes to the non-inverting input of a standalone difference amplifier (DA). The output of the 4-pole Bessel LPF also passes to the input of the Zero-Offset S&H module. The output of the Zero-Offset S&H circuit connects to the inverting input of the DA. The DA subtracts the value held by the Zero-Offset S&H circuit from the filtered ECG signal. If the Zero-Offset S&H circuit samples the ECG along the isoelectric line, the DA nullifies offsets and other undesirable non-zero amplitudes introduced by the source signal or by earlier stages.

However, bringing the isoelectric line to a near-zero potential is a two-step process. First, the Feedback S&H output, sampled from the inverting LPF of IA-1, is applied to the REF pin of IA-2. Sampling occurs 115 ms after the detected onset of an R-wave event – a point during the ST segment – and lasts for 3.5 ms. Applying this inverted and smoothed ECG signal sample to the REF pin of IA-2 has the effect of returning the isoelectric line to near zero prior to the onset of the T-wave segment. Maintaining a signal baseline closer to the power supply midpoint via the REF pin also tends to keep IA-2's integral difference amplifier out of saturation, even when large amounts of differential-mode noise (offset voltages) are present across the IA inputs.

The second step in the isoelectric line nulling process occurs at the end of each T-wave segment. Here, the Zero-Offset S&H circuit samples the output of the 4-pole Bessel LPF along the presumed isoelectric line for a period of 7 ms. The DA uses the newly sampled Zero-Offset S&H value to subtract any non-zero amplitudes from the filtered ECG signal. The corrections made by the Feedback S&H and Zero-Offset S&H sub-circuits are used by the software algorithm to adjust sections of the ECG signal so that the isoelectric line stays closer to zero potential. Isoelectric line correction is particularly important for T-wave height and area measurement accuracies.

The output of the DA passes to analog differentiator and integrator circuit modules. The differentiator determines the instantaneous slopes during T-wave segments. In addition, the output of the differentiator feeds into a full-wave rectifier circuit. The peak output of the full-wave rectifier dynamically sets the threshold for a Schmitt trigger that, when fired by the onset of an R-wave, say, initiates a series of timer controlled events. Full-wave rectification of the differentiator better ensures detection of inverted R-waves and negative polarity artifact signal swings. Dynamic Schmitt trigger thresholding better ensures detection of small R-waves and reduces undesirable non-R-wave triggers. The integrator module finds the area between the ECG signal and zero potential during T-wave segments. The integrator circuit is reset prior to the onset of each T-wave.

The T-wave monitor design includes five timers. Three of the timers – Timer 1, Timer 2, and Timer 3 – are activated when the Schmitt trigger fires. Timer 1 and Timer 2 define the interval over which a presumed T-wave event occurs. Timer 3 sets the delay for Timer 4. Timer 4 controls the Feedback S&H sample update. Timer 5, activated just

after the Timer 1 interval ends, controls the Zero-Offset S&H sample update. Each of the five timers is configured for monostable (one-shot) operation. Figure 1.6 shows the relative locations and durations of each timer event with respect to a typical ECG signal.

The steep slope of the rapid and relatively large signal swing that occurs at the leading edge of an R-wave produces large differentiator outputs. If the differentiator output produced is greater than the dynamically set threshold value, the Schmitt trigger fires, activating Timer 1, Timer 2, and Timer 3. The duration of Timer 1 is heart rate dependent and nominally adjusts to about 309 ms for 190 BPM and about 516 ms for 30 BMP. The relationship between heart rate and the duration of Timer 1 is non-linear and follows the curve shown in Figure 1.7.

The Timer 1 activation interval approximates the QT interval of Figure 1.1, but does not include the relatively brief Q-wave event (normally less than 40 ms) (Khan 2008). Timer 2 activation has a fixed duration of 160 ms. Timer 2 controls the T-wave area integrator reset function. The trailing edge of Timer 2 defines the beginning of the T-wave window interval. The trailing edge of Timer 1 defines the end of the T-wave window interval. Timer 3 activation has a fixed duration of 115 ms. Timer 3 activation interval approximates the RS interval.

Immediately following Timer 3, Timer 4 activates for 3.5 ms. During the Timer 4 interval, the Feedback S&H data is updated and immediately applied to the REF pin of IA-2. Occurring approximately 40 ms prior to the beginning of the T-wave window interval, application of the updated Feedback data to the REF pin of IA-2 step-corrects the differential-mode noise appearing at the input of the integral difference amplifier stage of IA-2. The Timer 4 activation interval provides enough time for reasonable

degrees of large-scale transient recovery while minimizing distortions within the T-wave segment caused by S&H step-changes imposed on the ECG signal.

The trailing edge of Timer 1 activates Timer 5. Timer 5 controls the Zero-Offset S&H data update. Similar to Timer 4, Timer 5's activation interval of 7 ms provides enough time to recover from most transient conditions, but here, instead of avoiding step-change distortion, the competing interest is to complete the timer's function before the onset of the next R-wave. Step-change signal distortions caused by the Zero-Offset S&H are less of a concern because the sample update occurs farther from the T-wave segment timing.

However, because the step-change actions of both S&H updates produce potentially large-magnitude differentiator outputs, the Schmitt trigger must be disabled during Timer 4 and Timer 5 intervals. Further, artifacts occurring anywhere within the Timer 1 activation interval could cause unwanted re-firing of the Schmitt trigger circuit. Fortunately, because Timer 4 is activated within the Timer 1 interval, only Timer 1 and Timer 5 events need be considered when disabling the Schmitt trigger function.

Although initially conceived as triangles, the shift to trapezoids for the outer two geometric shapes of the T-wave approximation arose from the need to accommodate instances where tangent lines to the points of dominant leading and/or trailing edge T-wave slopes intersect the edges of the T-wave interval window (the trailing edge of Timer 2 to the trailing edge of Timer 1) prior to reaching the T-wave baseline. Instances of T-wave window edge intersection can occur, for example, if the ECG signal exhibits ST elevations (flattens the leading edge slope, increasing the tangent lines' y-intercept), if the QRS intervals are abnormally long, or if the QT intervals are abnormally short or long.

Figure 1.8 shows an example of tangent lines drawn along the leading and trailing edges of a typical T-wave signal without window edge intersection. As shown, the trapezoids become triangles again.

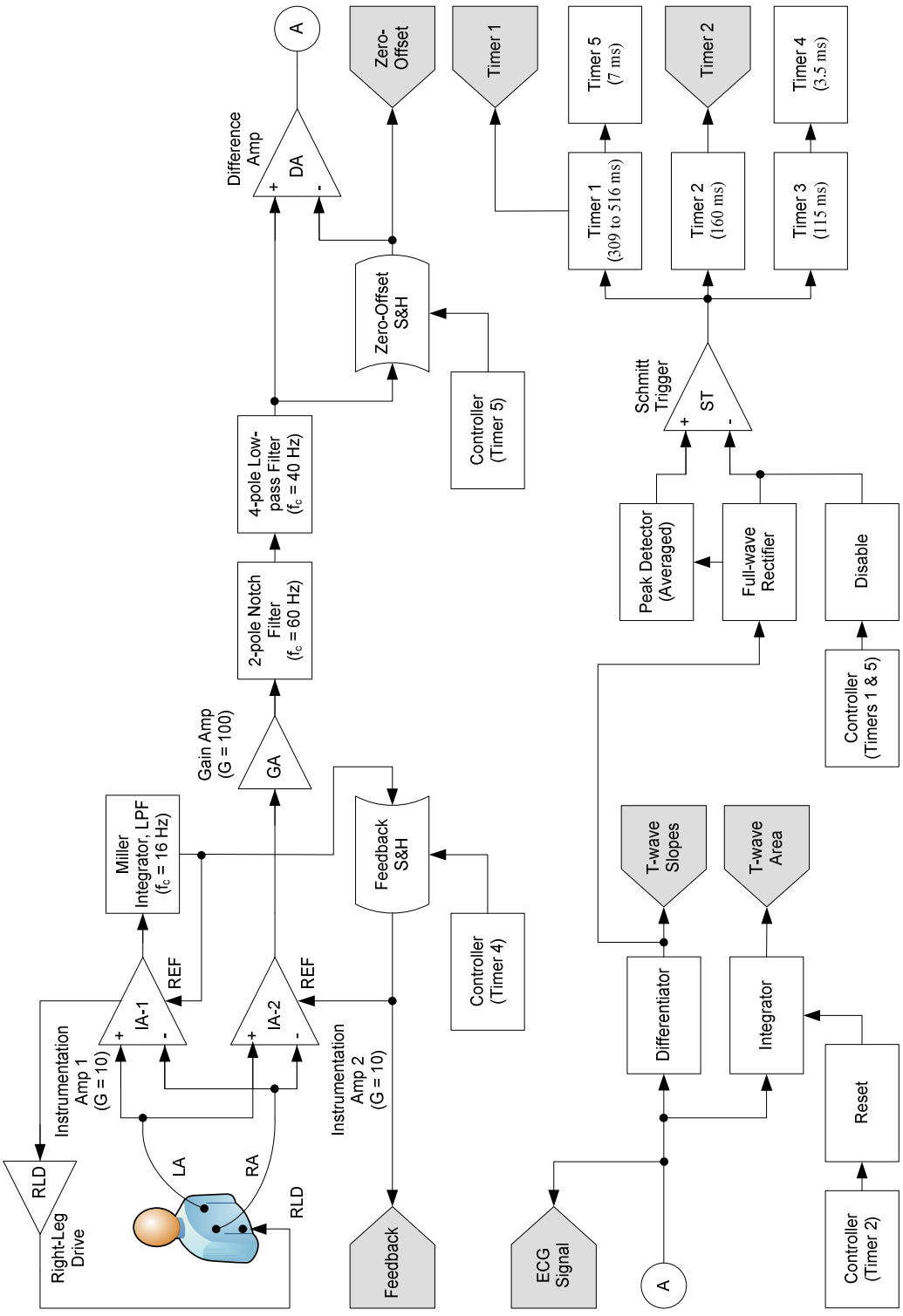

Figure 1.5. Signal-flow diagram of T-wave monitor. Shaded figures denote signal-processor data extraction (ADC).

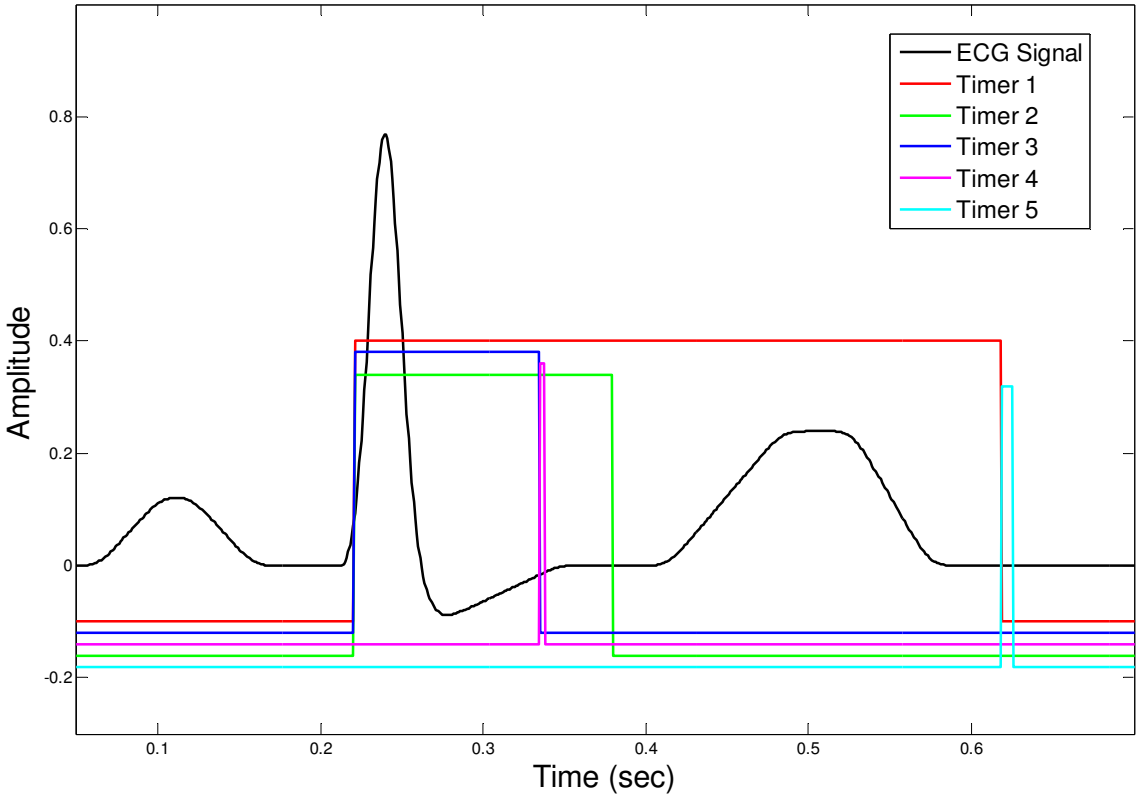

Figure 1.6. Timer 1 (red, approx. 400 ms), Timer 2 (green, 160 ms), Timer 3 (blue, 115 ms), Timer 4 (magenta, 3.5 ms), and Timer 5 (cyan, 7 ms) shown with simulated ECG signal (black, RR = 860 ms). Timer amplitude reduced and horizontal axes offset for clarity.

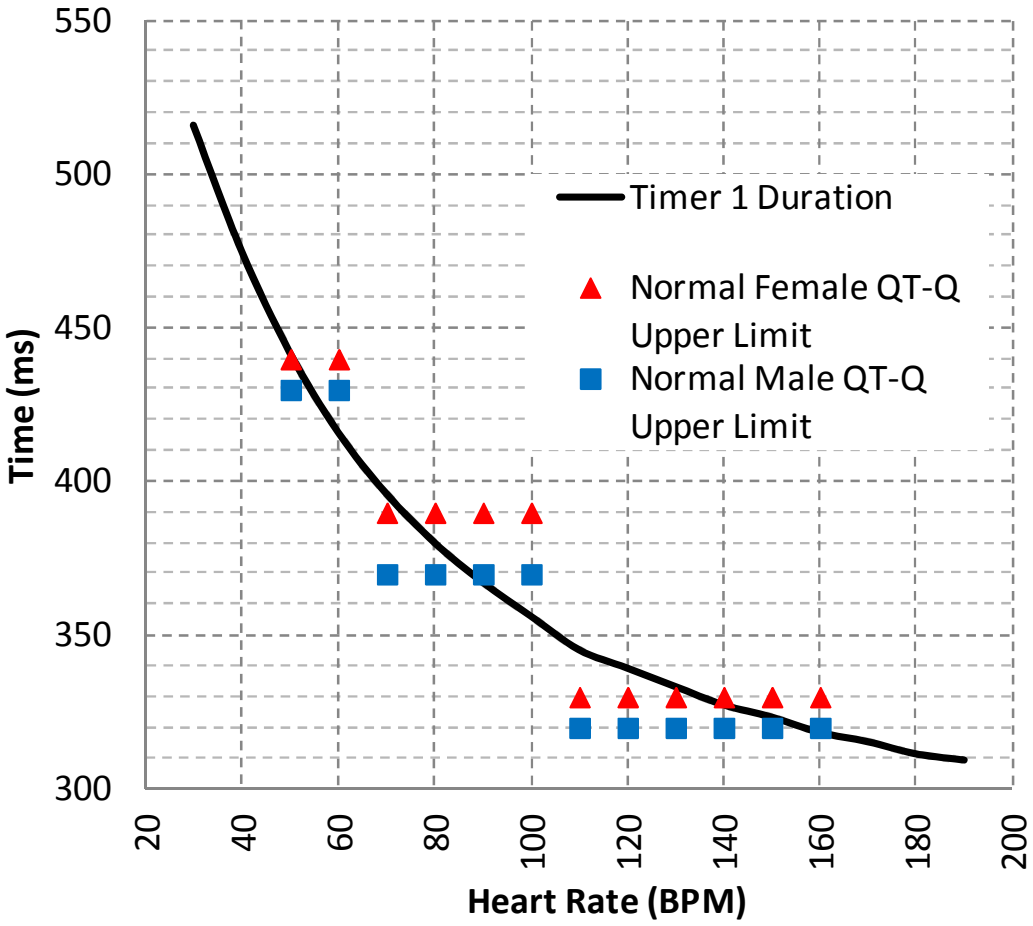

Figure 1.7. Measured Timer 1 duration (line) showing heart rate dependency along with approximation of upper limits for QT interval minus Q-wave (40ms) (markers) from Table 3.1.

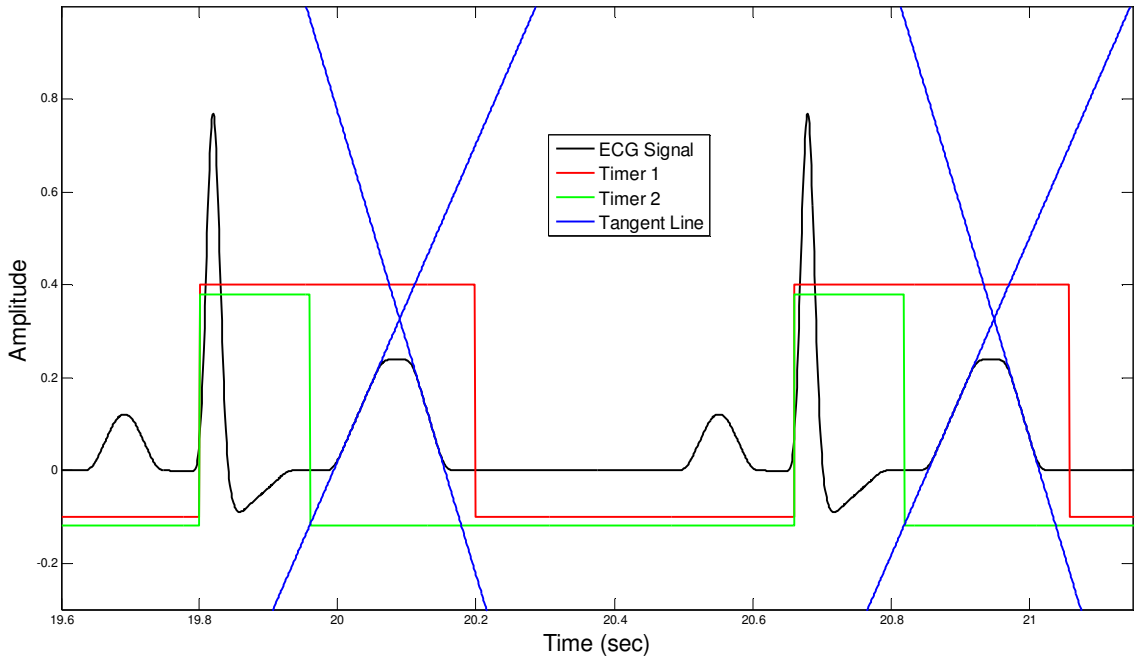

Figure 1.8. Tangent lines to T-wave at points of local maximum or minimum slope. Timer amplitude reduced and horizontal axes offset for clarity.

1.2.3. Software

The ECG signal-processing programs designed to complement the analog portion of the T-wave monitor were written within the MATLAB® (The MathWorks, Natick, MA, USA) environment and provide proof of concept for what could be written as code for an onboard microcontroller. The primary function of the programming is to use data extracted from the analog section of the T-wave monitor to construct the geometric T-wave approximations of Figure 1.4, overlaid onto the T-wave segment of the ECG signal. Goodness of fit assessment is one way to test the tenability of the stated hypothesis that the geometric composite figure is a reasonable and meaningful approximation of beat-to-beat T-wave morphology.

To represent the alignment of the geometric approximation figure with the T-wave of the ECG more accurately, some of the programming amplitude-adjusts discrete sections of the ECG signal to include the step-change corrections made by the analog S&H functions. The reconstructed ECG signal (with isoelectric line corrected) also better demonstrates the benefits and detriments of using step-change correction to keep the isoelectric line near zero potential.

The shaded blocks in Figure 1.5 schematically represent the seven points of analog-to-digital conversion necessary to complete basic programming functions. The ECG signal provides the data for R-wave and T-wave peak amplitudes, as well as the balance of signal information. The differentiator output provides data for the T-wave slopes. The integrator output provides the T-wave area measurement data. Reconstruction of the ECG signal with corrected isoelectric line requires data from the Feedback and Zero-Offset signals in conjunction with the ECG signal. Timer 1 and

Timer 2 signal data defines the T-wave window interval. However, for the purpose of hardware analysis and other operational investigations and reporting, several more signals from various points within the analog T-wave monitor design were imported into the software. The source codes for the relevant MATLAB® programs are included in Appendixes B through E.

CHAPTER 2

2. SPECIFIC AIMS AND SIGNIFICANCE

2.1. Specific Aims

Aim 1 – Design and test an analog ECG circuit that has specific focus on the T-wave segment. Test for frequency and transient response, and noise immunity, as appropriate.

Aim 2 – Design and demonstrate a time-domain based method for mitigating baseline drift, placing the isoelectric line near zero potential, and recovering from artifact transients without the waveshape distortion or recovery delays introduced by typical high-pass filtering methods. Compare the designed method (step-change correction) to typical high-pass filter methods under circumstances that include various forms of baseline drift and transients.

Aim 3 – Extract T-wave height, slope, and area metrics from the ECG signal and use them to construct composite geometric figures consisting of two trapezoids and a rectangle (Figure 1.4).

Aim 4 – Test the hypothesis that the geometric composites of Figure 1.4 are reasonable and meaningful approximations of beat-to-beat T-wave morphology across a range of ECG signals.

a) Determine reasonableness of the geometric composites by statistically assessing how well they represent the observed T-waves of the ECG signal.
b) Determine meaningfulness of the geometric composites by assessing if clinically relevant information, including the presence of alternans and

arrhythmias, can be observed and, perhaps, additionally classified in the time domain using the composite's constituent data exclusively.

2.2. Significance

The non-specificity of T-wave morphology has most significantly inspired the T-wave monitor design presented herein. Because it is evident that at least some descriptive elements of cardiac health are represented within the morphology of the T-wave segment, there is hope that a more quantified analysis of the T-wave will lead to better qualification of its morphologic significance, and, ultimately, to more advanced diagnostic and prognostic conclusions. For example, perhaps more than just the subtle amplitude variations that exist should describe the time domain observations of alternans. It may be that combining T-wave height with slope and area data provides greater insight into the alternans significance.

Further, waveform averaging results and spectral analysis features found by other alternans detection methods are not visually identifiable within the ECG signal tracings typically reviewed by cardiologists. Alternatively, the T-wave monitor of this thesis is designed to extract the beat-to-beat T-wave features that are observable, quantify them, and present them in real-time. In other words, the new T-wave data directly augments what is already typically observed and understood by the clinician, enhancing the chances of acceptance.

The beat-to-beat quantification of T-wave morphology will be useful to those investigators and clinicians committed to improving their understanding of time domain variations that occur within ECG signals. In addition, because the T-wave feature data extracted are highly compressed, the load on the resident systems will be reduced, as

patients with or without pathologies are studied to gather a more comprehensive morphological database. Broad classifications of discrete T-wave states can be improved to include quantified time-course events consisting of several waveshape features, expanding the body of knowledge readily available.

Exploring alternative methods of baseline drift reduction, isoelectric line correction, and artifact transient recovery expands the body of biomedical signal processing knowledge. Even though tailored specifically to improve placement of the T-wave's baseline to near zero potential for this design, the concepts employed and results obtained will be useful for other applications as well.

CHAPTER 3

3. METHODS

3.1. Introduction

Although other approaches to the T-wave monitor design were considered, tested, and eventually discarded due to their unremarkable performance, the signal-flow diagram of Figure 1.5 and the schematics that follow benefit from the investigative experience. Nevertheless, it is understood that the T-wave monitor design as presented is not ideal and represents only research efforts up to the beginning of comparative testing. In addition, some common design elements, such as compensation for op-amp voltage offset errors, were omitted to enhance simulation performance. Before describing sections of the T-wave monitor in more detail, support from literature review will be provided to underpin some of the decisions that shaped operational parameters, such as T-wave detection, ECG signal filtering, and T-wave feature extraction. To begin, a more refined characterization of the relevant features within the ECG signal is required.

3.2. ECG Feature Definition

Key to the success of the T-wave monitor design is finding the T-wave apart from other events in the cardiac cycle of the ECG signal. Unfortunately, the T-wave is not typically the ECG feature of greatest magnitude in Leads I or II. T-wave frequency is also somewhat problematic because its low-ranging spectral content can be highly confused with or disturbed by even moderate baseline drift and artifacts (Mneimneh et al. 2006). The R-wave, on the other hand, has the highest frequency content of the ECG waves and normally presents as the feature of greatest magnitude in the ECG leads of

interest. Therefore, the R-wave was chosen as the ECG feature to be detected. Once detected, the R-wave serves as a temporal reference for finding the T-wave that follows.

Referring back to Figure 1.1, an R-wave has a nominal magnitude of about 1 mV and is expected to be less than 2 mV in Lead I, for example (Malmivuo and Plonsey 1995; Mohrman and Heller 2010; Fuster et al. 2011). Being the largest amplitude ECG feature suggests that R-wave detection is possible using magnitude thresholding in the time domain. In addition, the R-wave has the highest frequency content. Combining the large magnitude and high frequency attributes of the R-wave facilitates its detection, as will be discussed later in this chapter.

Some authors define the nominal QRS interval duration at about 80 – 90 ms (Malmivuo and Plonsey 1995). Others indicate that normal QRS intervals span the slightly wider range of 60 – 100 ms (Mohrman and Heller 2010; Tintinalli et al. 2011). QRS intervals greater than 120 ms are considered abnormal, likely caused by a bundle branch block (Gholam-Hosseini and Nazeran 1998; Khan 2008). Nominal QT interval duration is defined as having a range of 330 – 420 ms (Tintinalli et al. 2011). Some sources link the QT interval to a specific heart rate; for example, defining that the QT interval should be less than 380 ms at 60 beats per minute (BPM) (Mohrman and Heller 2010). However, since the QT interval duration inversely relates to BPM, the interval is better defined when specified over a range of heart rates, as listed in Table 3.1 (Khan 2008).

The T-wave has a nominal magnitude of around 0.2 mV (Malmivuo and Plonsey 1995). With all things normal, it is expected that the T-wave will be less than 0.5 mV in standard limb leads (Khan 2008). The T-wave follows the onset of the QRS interval after

about 200 ms and lasts for about another 200 ms (Malmivuo and Plonsey 1995). The normal Q-wave, on the other hand, should have durations less than 40 ms (Khan 2008). Subtracting the maximum duration Q-wave (40 ms) from the T-wave delay of 200 ms suggests that the T-wave starts around 160 ms after the R-wave. Consequently, Timer 2 was designed to trigger at the onset of the R-wave and is activated for 160 ms so that Timer 2's trailing edge defines the start of the T-wave window interval (Figure 1.6). By the same logic, Timer 1 was designed to perform as a heart-rate dependent QT interval window, minus the 40 ms maximum duration Q-wave (Figure 1.7). The trailing edge of Timer 1, therefore, defines the end of the T-wave window interval (Figure 1.6). T-wave features are extracted from the ECG signal within the T-wave window interval.

Table 3.1. Clinically useful QT upper time limit approximations (data from Khan 2008).

Heart Rate (BPM)	**Male (ms)**	**Female (ms)**
45–65	< 470	< 480
66–100	< 410	< 430
> 100	< 360	< 370

3.3. ECG Filter Design

The QRS complex has frequency content ranging from about 10 – 25 Hz (Castiglioni et al. 2003). Diagnostic electrocardiographic devices are tested for peak height detection accuracy using a 1 mV triangular QRS approximation with a base width of 20 ms (Diagnostic 2007). The test waveshape corresponds to a full-wave QRS frequency of 25 Hz (Diagnostic 2007). One study of 111,738 normal and arrhythmic QRS complexes found maximum spectral energy – after averaging within each subpopulation – at frequencies that ranged from a low of 8.4 Hz up to 20.03 Hz (Darwich and Fokapu 2007). The normal population in the study (72,954 QRS complexes) had, on average, maximum QRS spectral energy at 15.82 Hz (Darwich and Fokapu 2007). While the energy of the R-wave alone was not specifically cited, it is reasonable to suppose that the R-wave is the primary contributor to the spectral energy of the QRS complex and, therefore, that the frequency of maximal spectral energy is representative of the R-wave frequency. With these findings in mind, a nominal R-wave frequency of 20 Hz was chosen to assess the impact of the 2-pole 60 Hz notch filter and the 4-pole Bessel LPF designs on what might be considered a typical ECG signal.

Similar to the R-wave, the frequency content of the T-wave is often buried within reported data or absent altogether. As a first approximation, the 200 ms duration T-wave described above can be considered the half-cycle of a sine wave whose period is twice its duration, or 400 ms, giving the T-wave a fundamental frequency of 2.5 Hz. The T-wave model used in cardiac monitor testing is a half-cycle sine wave of 180 ms duration, giving the model a fundamental frequency of about 2.8 Hz (Cardiac 2002). Ironically, the cardiac monitor tests seek to prove that the T-wave will *not* be detected by the device.

In truth, T-wave morphology is neither sinusoidal nor typically symmetrical. One research study sought to classify patients with myocardial infarction by comparing the spectral energy of their T-waves to those without infarction. While there were statistically significant differences found between the groups, the investigation reported that more than 93% of the T-wave's spectral energy was below 10 Hz in both the diseased (n = 23) and control (n = 23) populations (Giuliani and Burattini 2012). Two other items of interest were observed in their findings. First, around 80% of the T-wave's spectral energy is contained in the frequencies below 5 Hz (Giuliani and Burattini 2012). Second, the spectral energy amounts increase as the frequencies drop toward 0 Hz (Giuliani and Burattini 2012). The first of these two observations lends support to the decision to choose 5 Hz as the nominal T-wave frequency for design assessment. The second supports the effort taken to eliminate high-pass filtering from the ECG signal path, although the influence of 1/f noise on their findings is not discounted (Ward and Greenwood 2007).

It can be derived from the transfer function of equation (3.1) that an active 2-pole 60 Hz notch filter of Twin-T topology and a Q of 0.5 (unity gain) theoretically attenuates 20 Hz sinusoids (R-wave) by 1.938 dB and 5 Hz sinusoids (T-wave) by 0.121 dB (Mancini 2003). At 60 Hz, the frequency response function drops to a gain of zero.

$$H(s) = \frac{1 + \mathrm{s}^2}{1 + 2s + \mathrm{s}^2} \tag{3.1}$$

The transfer function of an active 4-pole Bessel LPF of Sallen-Key topology with unity gain is given by equation (3.2) (Mancini 2003). With a cutoff frequency of 40 Hz, theoretical frequency response attenuation at 20 Hz is 0.705 dB. Attenuation at 5 Hz is a mere 0.043 dB. Attenuation at 60 Hz, on the other hand, is 7.423 dB.

$$H(s) = \left(\frac{1}{1 + a_1 s + b_1 s^2}\right)\left(\frac{1}{1 + a_2 s + b_2 s^2}\right) \tag{3.2}$$

where $a_1 = 1.3397$, $b_1 = 0.4889$, $a_2 = 0.7743$, $b_2 = 0.3890$.

Clearly, theoretical frequency response calculations are needed for comparison with experimental findings. However, it is also fundamentally important to understand the broader effect that filters have on the signals of interest. For example, attenuation of the R-wave potentially affects detection methodologies and may be clinically significant if the peak amplitude of the T-wave is referenced to the R-wave peak, say, as a ratio. For industry perspective, the American National Standards Institute (ANSI) in conjunction with the Association for the Advancement of Medical Instrumentation (AAMI) consider R-wave peak height inaccuracies of up to 10% acceptable for diagnostic ECGs (Diagnostic 2007). Ambulatory-grade devices can have R-wave peak height inaccuracies of up to 25% (Cardiac 2002). The primary concern here, however, is the integrity of the T-wave. So far, notch and low-pass filter attenuation at the chosen nominal T-wave frequency of 5 Hz sums to just 0.164 dB (1.87%), and no high-pass filtering attenuations or distortions have been introduced.

Choosing a Bessel LPF over, say, a Butterworth type minimizes the overshoot, settling time, and ringing that occurs in response to step changes. Particular to the T-wave monitor design presented here, step-change corrections are introduced twice per cardiac cycle. The adverse effects of the step corrections were minimized by using a filter that has optimum square wave transmission response, even though passband flatness and rolloff sharpness were sacrificed to a degree (Horowitz and Hill 1989). Table 3.2 lists some of the key performance characteristics for a few common filter types. By comparison, the Bessel filter's overshoot performance is outstanding.

It is worthwhile to note that the R-wave, especially relative to the other normal cardiac events within the ECG signal, affects the filters like a spike or impulse source – another step-like disturbance. The Bessel filter's reduced overshoot ensures that the S-wave and ST segment features that follow are more accurately depicted than with other common filter types.

Experimental observations of high-pass filtering schemes that use Miller integrators in ways similar to the one connected to IA-1 in Figure 1.5, revealed that the R-wave *pushed*, so to speak, on the integrator's signal average (baseline component), driving it away from its nominal level with every heart beat. The effect was especially pronounced in those designs with cutoff frequencies approaching the 0.67 Hz upper limit of ambulatory-grade ECGs (Medical 2001; Cardiac 2002). The T-wave also *pushes* on the integrator's signal average. In this case, the HPF effect tends to reduce non-inverted T-wave amplitude (relative to zero) and cause other phase-induced morphologic distortions. For example, HPF distortions from either active or passive topologies can create what appear to be potentially pathologic ST depressions and biphasic characteristics in the T-wave. The HPF effect is demonstrated on a simulated ECG signal in Figure 3.1, using a cutoff frequency of 0.67 Hz

For completeness, radio frequency interference (RFI) low-pass filters were designed and included at the front-end of each instrumentation amplifier. With cutoff frequencies in excess of 450 Hz for differential-mode and 9.5 kHz for common-mode operation for all designs presented, the filters have negligible impact on the ECG signal bandwidth. Consequently, these filters will not be discussed in too much detail, other

than to provide the formulas used to derive them (Kitchin and Counts 2006). Referring to Figure 3.6B:

$$f_{Common-Mode} = \frac{1}{2\pi R_{14/19} C_{33/36}} \tag{3.3}$$

$$f_{Differential-Mode} = \frac{1}{2\pi R_{14/19}\left(2C_{34} + C_{33/36}\right)} \tag{3.4}$$

Table 3.2. 4-pole LPF time-domain performance comparison (data from Horowitz and Hill 1989).

Type	Step Rise Time (0 to 90%) (s)	Overshoot (%)	Settling Time (to 0.1%) (s)	Stopband Attenuation ($f = 2f_c$) (dB)
Bessel	0.5	0.8	1.2	13
Butterworth	0.6	11	2.8	24
Chebyshev, 0.5 dB ripple	0.7	18	5.4	31

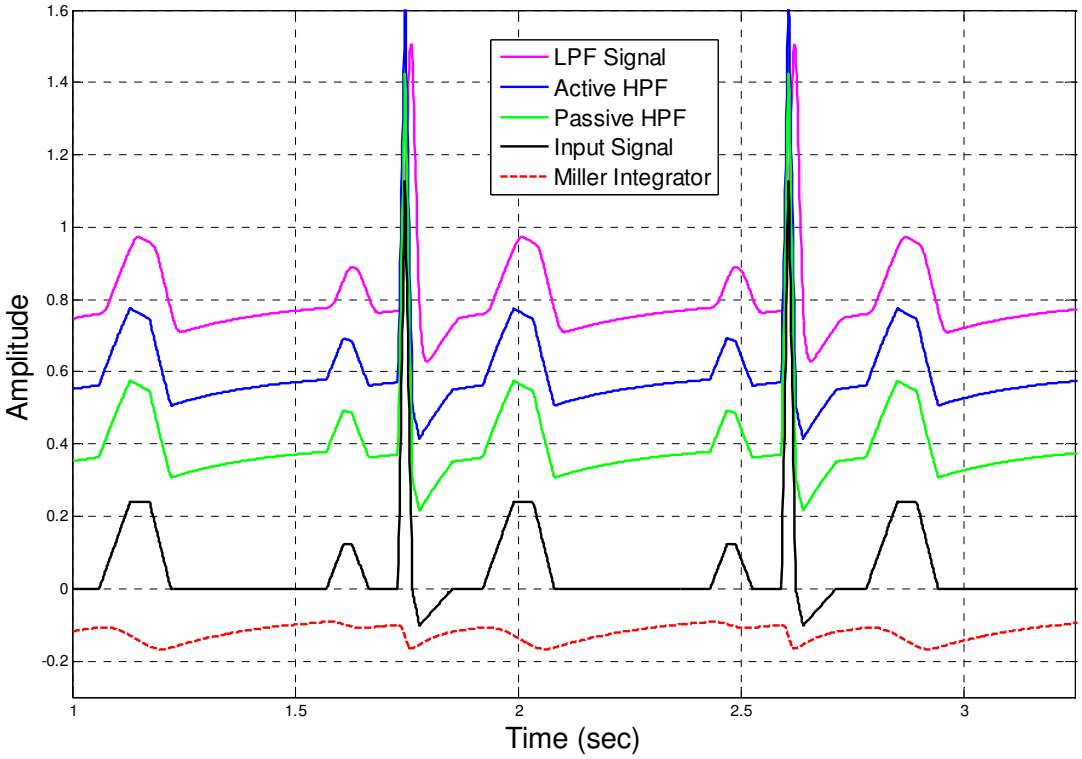

Figure 3.1. Simulated ECG (black) affected by 0.67 Hz HPF (passive = green, active = blue) to show induced ST depression and diphasic-like distortion. Output of Miller integrator (red, dashed) is summed with Input Signal at REF pin of IA-1 to create Active HPF result. LPF Signal (magenta) is Active HPF signal filtered by 2-pole 60 Hz notch and 4-pole 40 Hz Bessel LPF. Horizontal axes offset for clarity.

3.4. Hardware

All hardware designs were implemented and tested using Multisim (National Instruments, Austin, TX, USA) circuit simulation software. Top-level schematics for the T-wave monitor are shown in Figure 3.2 through Figure 3.5. Figure 3.6 through Figure 3.12 show schematics for the sub-circuit blocks, SC1 through SC20. The sub-circuits generally correspond to the functional blocks of Figure 1.5. Discussions found in the Design Overview section of Chapter 1 and the rationales in preceding sections of Chapter 3 should suffice to explain many of the basic functions. However, when it serves to advance the understanding of critical operational elements, sub-circuit design and performance details will be highlighted.

3.4.1. Sample and Hold

The S&H sub-circuit of Figure 3.8A represents SC4: Feedback S&H and its functional equivalent, SC8: Zero-Offset S&H. The SampleIn signal updates the voltage across C39 every heart beat. The heart rate, however, can be as low as about 30 BPM, making for sample hold times that can exceed 2 seconds. Extended hold times imply the use of a large hold capacitor. Fast sample acquisition, on the other hand, implies the use of a small hold capacitor. Sample acquisition must be faster than 3.5 ms (Timer 4 duration) for the Feedback S&H or 7 ms (Timer 5 duration) for the Zero-Offset S&H. Further, the ECG signal at the output of the IA with a gain of 10 is on the order of 10 mV, but artifacts and offset drift can push the baseline signal to ±3 V or more, with ±5V power supplies.

To maintain the sampled baseline correction value constant, the dV/dt across C39 must be minimized, keeping it a small percentage of the 10 mV ECG signal,

regardless of baseline magnitude. One of the primary sources of dV/dt is leakage current flowing through C39. Other leakage sources include op-amp input bias currents, OFF-state currents flowing through the analog switch inputs, and currents through stray capacitive and resistive elements. Making matters worse, leakage current magnitudes are directly related to the applied signal voltage.

In an attempt to reduce dV/dt errors, amplifier U2B was installed to *sense* the leakage current as a voltage produced across R38. U2B then actively nulls the leakage current by feeding its inverse through R35 to the top of C39, bringing the R38 voltage back toward zero. To ensure that the baseline correction voltage across C39 does not include the voltage developed across R38, R38 is shunted to ground (common) during sampling.

A more elegant approach to reduce the dV/dt droop effect of leakage currents in the S&H sub-circuits is shown in the closed-loop design of Figure 3.16. During sampling, FollowerOut is connected to SampleIn and the circuit behaves as a LPF with $\tau = R_{37}C_{43}$, charging C43 to the input voltage (Baker 2010). After the sample period (Timer 4 or Timer 5), FollowerOut is disconnected from SampleIn and instead grounded to isolate the input signal from the output. Although this design was implemented after most of the data file simulations were run, a performance comparison was made using simulated ECG data and ±300 mV offset steps. The closed-loop S&H design approach offers improvements, such as reduced dV/dt, fewer parts, and a faster sampling time constant.

3.4.2. Differentiator and Peak Detector

The differentiator portion (U7A) of sub-circuit SC10 in Figure 3.9A ideally operates according to the transfer function in equation (3.5), or in the time domain, according to equation (3.6) (Sedra and Smith 2004).

$$H(s) = -sR_{62}C_{49} \tag{3.5}$$

$$v_{out}(t) = -R_{62}C_{49}\frac{dv_{in}(t)}{dt} \tag{3.6}$$

Unfortunately, the differentiator circuit in its ideal configuration tends to be too sensitive to high frequency noise. To reduce the undesirable oversensitivity, R60 was added in series with C49 to give the system a cutoff frequency at about 1.6 kHz. The addition of R60 changes the transfer function to equation (3.7).

$$H(s) = \frac{-sR_{62}C_{49}}{1 + sR_{60}C_{49}} \tag{3.7}$$

While no longer ideal, the inverting differentiator closely maintains the necessary -90° phase shift over the T-wave bandwidth of 0 to 10 Hz and rises to a 5% error (-94.5°) at 125 Hz. At the nominal T-wave frequency of 5 Hz, phase error is only about 0.2 %. As a secondary design criterion, C49 and R62 values were selected to make the 0 dB crossing near 5 Hz.

The differentiator is followed by an inverting LPF with a cutoff frequency around 160 Hz and a gain of -5. Experimentally determined, the additional signal smoothing of this LPF helps reduce unwanted firing of the Schmitt trigger. Unfortunately, the LPF further impinges upon ideal differentiator behavior, dropping the 5% phase error to just above 11 Hz. The inverter gain boosts the maximum slope of a 5 Hz signal at 200 mV peak (T-wave model after gain of 1,000) to about 1 V. However, a 20 Hz signal at 1 V

(R-wave model after gain of 1,000) would be amplified to about 20 V, if power supply headroom allowed.

The differentiator, then, has two functions: First, after dividing the differentiator sub-circuit output voltage by the RC coefficient in equation (3.6) and the gain of the inverter, the slopes of the T-wave can be extracted from the ECG signal within the T-wave interval window. Second, taking the derivative of the ECG signal has increased the R-wave-to-T-wave amplitude discrimination by a factor of four (in this case, from 1 V/200 mV to 20 V/1 V), significantly improving the magnitude thresholding technique used to detect R-waves.

As previously described, the differentiator output is full-wave rectified (Figure 3.9B) and sent to the peak detector of Figure 3.9C. Initial charge of the peak-hold capacitor of Figure 3.9C, C51, is about 2 V, as determined by the R69 setting minus the diode drop across D3. The peak output of the full-wave rectifier sub-circuit, if greater than 2 V, charges C51 with a time constant of about 200 µs during the first 40 ms of the Timer 2 interval. Charging of C51 is inhibited for the remainder of the Timer 2 interval and is also inhibited during the Timer 5 interval, where step-change differentiator spikes could be falsely interpreted as R-wave events. Peak charging is permitted during the T-wave window interval with the rationale that tall T-waves should raise the peak differentiator voltage so the T-waves will not be confused with R-waves in the cycles that follow.

The C51 discharge time constant is 3 s and, without additional input, the C51 voltage will settle back to its initial charge value of 2 V. The buffered C51 voltage, DiffPeak, is reduced to 75% of its value at the resistor divider formed by R2 of Figure

3.3. The voltage on the wiper of R2 defines the threshold level for the Schmitt trigger of Figure 3.10A. Other than during the Timer 1 and Timer 5 intervals when the Schmitt trigger is disabled, rectified differentiator outputs larger than the threshold level will fire the Schmitt trigger, signaling the start of an R-wave event and initiating the timer functions.

3.4.3. Integrator

The integrator sub-circuit of Figure 3.9D is less burdened by non-ideal circuit elements than the differentiator is, and its only function is to find the area of the T-wave. The Miller integrator's transfer function is presented in equation (3.8), followed by its time domain equivalent in equation (3.9) (Sedra and Smith 2004).

$$H(s) = -\frac{1}{sR_{73}C_{52}} \tag{3.8}$$

$$v_{out}(t) = -\frac{1}{R_{73}C_{52}}\int_0^t v_{in}(t)dt \tag{3.9}$$

For the integrator circuit to maintain the idealized behavior inherent in equations 3.8 and 3.9, there must not be an impedance in parallel with C52. In fact, though, there is an analog switch wired across the C52 capacitor in series with a current limiting resistor, R76. Fortunately, the OFF-state impedance of the switch is greater than 10^9 Ω and so can be ignored without consequence (ADG441 2005). The second requirement for idealization is that the initial condition voltage across C52 must be zero prior to integration. As designed, the analog switch, actuated by Timer 2, resets the C52 voltage prior to the start of each T-wave interval window.

In the absence of the Feedback step-change correction that occurs just prior to integration, maximum integrator reset errors could be as high as ± 33 mV by the following formula (ADG441 2005):

$$Reset\ Error_{max} = \left(\frac{R_{on_{max}} + R_{76}}{R_{73}}\right) v_{in_{max}} \tag{3.10}$$

$$= \left(\frac{70\ \Omega + 1\ \text{k}\Omega}{160\ k\Omega}\right)(\pm\ 5\ V)$$

$$= \pm\ 33\ mV$$

Feedback step-change correction improves the integrator reset errors significantly, however, by reducing the range of v_{in} to levels that should be at most a few hundred millivolts during transient recovery conditions. Transient recovery usually completes in a few heartbeats, after which v_{in} levels are corrected to near zero. Nevertheless, using ±300 mV for $v_{in_{max}}$, the reset error is reduced to ± 2 mV under transient conditions. Under normal circumstances, the reset error will be insignificant because baseline correction prior to integration typically limits v_{in} to within a few millivolts of zero, driving the reset error down to tens of microvolts. The Zero-Offset step-change isoelectric line correction that occurs after the T-wave window interval tends to reduce the reset error even further.

Similar to those of the differentiator, the RC values of the integrator were selected such that the 0 dB crossing occurs near 5 Hz. The ideal +90° phase shift is maintained down to around 8 mHz, whereupon the phase rises by 5%. The inverter that follows the integrator has a gain of -1, correcting the signal polarity (phase) and buffering the output.

3.4.4. Timer 1

Timer 1 output, driven high by the Schmitt trigger pulse, is returned low when the voltage on the Threshold pin (pin 6) reaches two-thirds of the supply voltage (VSS1) (LM555 2006). In monostable timer configurations with fixed duration pulses, pulse width is controlled by the general formula of 3.11, where, in the case of Figure 3.10B, R is R86 and C is C55 (LM555 2006).

$$Timer\ ON = 1.1(RC) \tag{3.11}$$

By equation (3.11), Timer 1 minimum duration is 284 ms with the R86 and C55 values of 550 kΩ and 0.47 μF, respectively. The heart rate dependency of the Timer 1 sub-circuit of Figure 3.10B is based on the concept that reducing the charging currents to timing capacitor C55 will prolong the time it takes to charge and, thereby, extend the duration of the timer pulse. In other words, reducing the charging currents to C55, in effect, increases its apparent capacitance. If the amount of charging current *siphoned* away from C55 is made inversely proportional to heart rate, then timer duration will be also, extending to accommodate the longer QT intervals of slower heart rates.

For the first 115 ms of T-wave monitor operation, V1 of Figure 3.4 initializes the Timer 1 interval by charging C54 to 5V through R81, maximally decoupling diode D5. Under these conditions, Timer 1 operates at its shortest duration of 284 ms. However, as C54 discharges through R84, the charging voltage on C55 eventually exceeds the voltage on C54 enough to allow current to flow through D5 and its associated components, R83, R84, and C54. It is the current flow through D5 that reduces the charging currents to C55, extending the Timer 1 interval.

At the beginning of every heart beat cycle, R-wave events trigger the simultaneous start of Timer 1 and Timer 2. The Timer 2 output pulse, wired to D4, charges C54 through R82 to restore some portion of the voltage that discharged since the previous Timer 2 pulse ended. The duration of Timer 2 is fixed at 160 ms, making the charge time of C54 also fixed at 160 ms. The time since the previous Timer 2 pulse (or R-wave), however, is directly a function of heart rate. Therefore, the longer the time between Timer 2 pulses, the more voltage discharges from C54. The lower the voltage on C54, the sooner D5 couples, reducing the charging currents to C55 and increasing the Timer 1 interval. Conversely, faster heart rates mean shorter C54 discharge times, so D5 is coupled for a smaller fraction of the C55 charging cycle, reducing the Timer 1 interval accordingly.

The Timer 1 interval versus heart rate was measured experimentally and is represented by the curve of Figure 1.7. Resistor and capacitor values chosen to achieve the Timer 1 performance shown were determined heuristically. Overall Timer 1 sub-circuit operation is demonstrated in Figure 3.17, using a series of progressively staggered simulated R-wave events. Input trigger signals were placed at 0.684, 1.0, 2.0, 3.5, 5.5, 8.0, 8.7, and 9.2 seconds, to provide a demonstration range of 24 to 190 BPM. Note also in Figure 3.17 that after the Timer 2 interval has completed, the C55 charging currents that flow during the balance of the Timer 1 interval can hold or raise the voltage on C54 when D5 is coupled. The additional charging of C54 is most pronounced when Timer 1 intervals are long (low BPM) and, so, tends to compensate for the deeper C54 discharge droop between cycles.

3.4.5. Right-Leg Drive

Input for the RLD and shield drive amplifiers of Figure 3.6C is taken from the midpoint of the two gain resistors (R16 and R18) of instrumentation amplifier U1 in Figure 3.6B. As such, the RLD input represents the common-mode voltage (CMV) of the incoming ECG signal. Ideally, the common-mode potential rests at the midpoint of the power supply rails to maximize the dynamic range of the system. Common-mode noise, however, and in particular those noises coming from external AC power sources, can vary the midpoint potential to detrimental effect if the ECG device is not well isolated from the noise source ground. For example, CMV levels near enough to the power supply rails can cause signal clipping because of IA input stage saturation. In addition, unbalanced IA inputs can convert otherwise rejected common-mode noise into differential-mode noise, which is then amplified along with the ECG signal.

To ensure that high levels of common-mode rejection are designed into medical equipment, ANSI/AAMI standard testing procedures require ECG devices to have outputs of less than 1mV peak when all patient leads are wired to a single 10 Vrms common-mode line frequency source (Cardiac 2002; Diagnostic 2007). The RLD portion of the sub-circuit in Figure 3.6C (U4A) augments the inherent CMR of the IA design by amplifying and inverting the common-mode noise and delivering it back to the patient's body through a current limiting impedance , R29. U4A has an open loop gain of -39 and operates up to a cutoff frequency of about 1 kHz to reduce noise from common-mode sources that generate higher order harmonics, such as fluorescent lights (Winter and Webster 1983).

As is typical for many closed-loop systems using negative feedback, however, care must be taken to design such that phase shifts and gains around the loop do not create unstable conditions. From the feedback amplifier signal-flow diagram of Figure 3.18 and its closed-loop transfer function of equation (3.12), loop gain is defined as the product $G(s)H(s)$, where $G(s)$ is the open-loop feedforward transfer function and $H(s)$ is the open-loop feedback transfer function (Sedra and Smith 2004). The condition of instability to be avoided is a loop gain of unity or greater coupled with a phase shift of $180°$ (Sedra and Smith 2004). The common-mode signal passing through the feedforward IA experiences a unity gain up to the cutoff frequency of the common-mode RFI filter. Thereafter, the common-mode signal is attenuated by 20 dB per decade.

$$\frac{Out(s)}{In(s)} = \frac{G(s)}{1 + G(s)H(s)} \tag{3.12}$$

3.4.6. T-wave Monitor Designs with High-Pass Filters

In addition to the primary step-change correction T-wave monitor design (Model 4c), two variations, employing a single IA and high-pass filtering with cutoff frequencies of either 0.5 Hz (ambulatory, Model 1) or 0.05 Hz (diagnostic, Model 1a), were designed to test for comparative differences in baseline drift mitigation and artifact transient recovery performance. T-wave monitor designs with HPF do not include step-change correction hardware – Feedback S&H, Zero-Offset S&H, Difference Amp, Timer 3, and Timer 4 sub-circuits – and, therefore, the Feedback and Zero-Offset signals are also not present. Timer 5 remains to disable the Schmitt trigger for 7 ms between Timer 1 intervals – maintains timing consistency with the step-change correction design. The IA sub-circuit blocks with HPF are detailed in Figure 3.13.

3.4.7. Electrodes, DC Offsets, and Common-Mode Rejection

DC bias currents can cause significant changes to electrode half-cell potentials (Macfarlane et al. 2011). Over time, bias currents tend to polarize the electrodes (Macfarlane et al. 2011). Electrode potential and electrode impedance changes present the IA with the time-varying differential offset voltages often referred to as baseline drift. In addition, mechanical disturbance of the charges within the electrode interface double-layer can produce large motion artifact noise (Macfarlane et al. 2011). To ensure that ECG signals are still readable under either of these circumstances, ANSI/AAMI standards require testing ECG devices with input offset voltages up to ±300 mV (Cardiac 2002; Diagnostic 2007).

To test the T-wave monitor designs for dynamic range and artifact transient response, a series of ±300 mV steps were introduced into the ECG signal. The time between steps was adjusted per design to accommodate recovery performance. The modified input signal sub-circuit is shown in Figure 3.14A. Common-mode rejection was tested using the sub-circuit shown in Figure 3.14B. Again, the ECG test setup is similar to those found in ANSI/AAMI standards (Cardiac 2002; Diagnostic 2007).

The dynamic range/transient response and CMR test circuits also include electrode models (310 kΩ in parallel with 0.01 μF) in each of the three leads (Cardiac 2002; Diagnostic 2007). When measured at 10 Hz and located on the chest area, the impedance of the electrode models was designed to represent worst-case impedance for greater than 99.9 % of a typical population (Cardiac 2002; Diagnostic 2007). Additionally, the electrode lead series impedances were increased from 390 kΩ to 500 kΩ to reduce bias currents, better protect the patient from leakage currents, and reduce

the impact of frequency-dependent electrode impedances on the RFI filter cutoff frequency (Figure 3.15A). The RFI filter capacitors were adjusted accordingly.

Lastly, the RLD circuit was redesigned to improve stability of the closed-loop system. Most of the simulation runs, however, did not use the updated design because of time constraints. Shown in Figure 3.15B, an electrode impedance imbalance model (51 kΩ in parallel with 0.047 μF) was included in the lead of the RLD per ANSI/AAMI set up procedures to worsen the scenario of the CMR tests (Cardiac 2002; Diagnostic 2007).

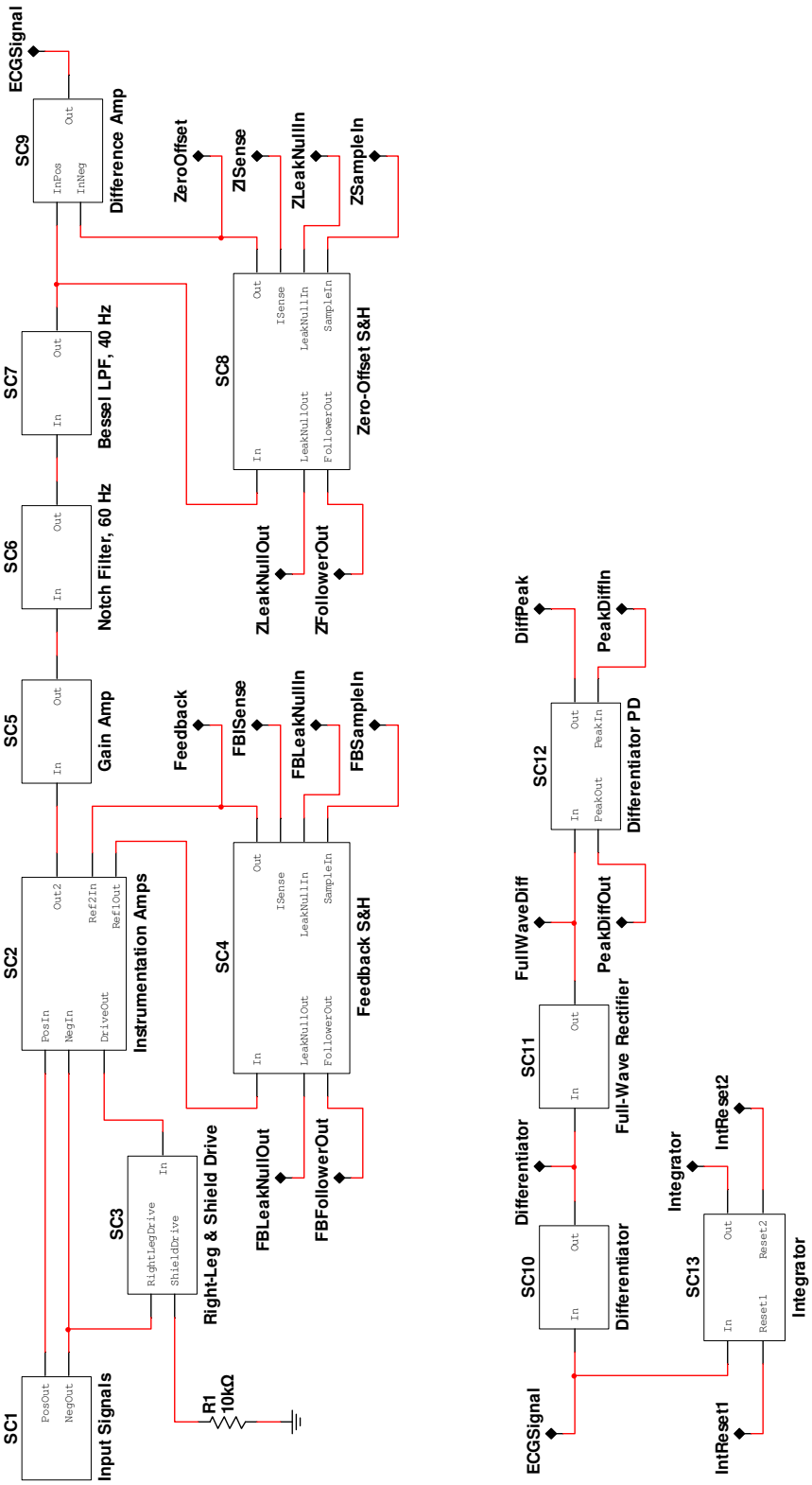

Figure 3.2. T-wave monitor, Model 4c. Top-level schematic, sheet 1 of 4.

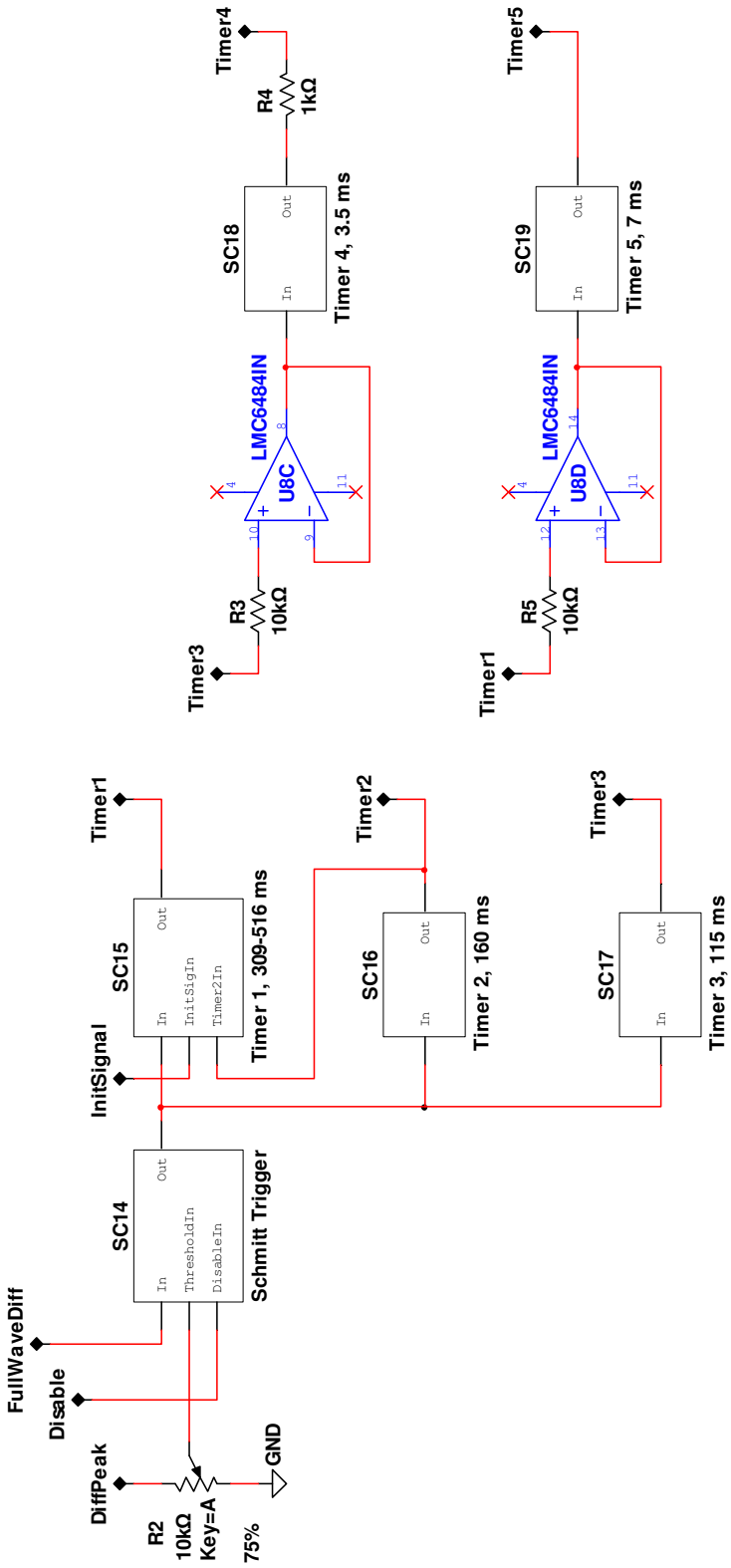

Figure 3.3. T-wave monitor, Model 4c. Top-level schematic, sheet 2 of 4.

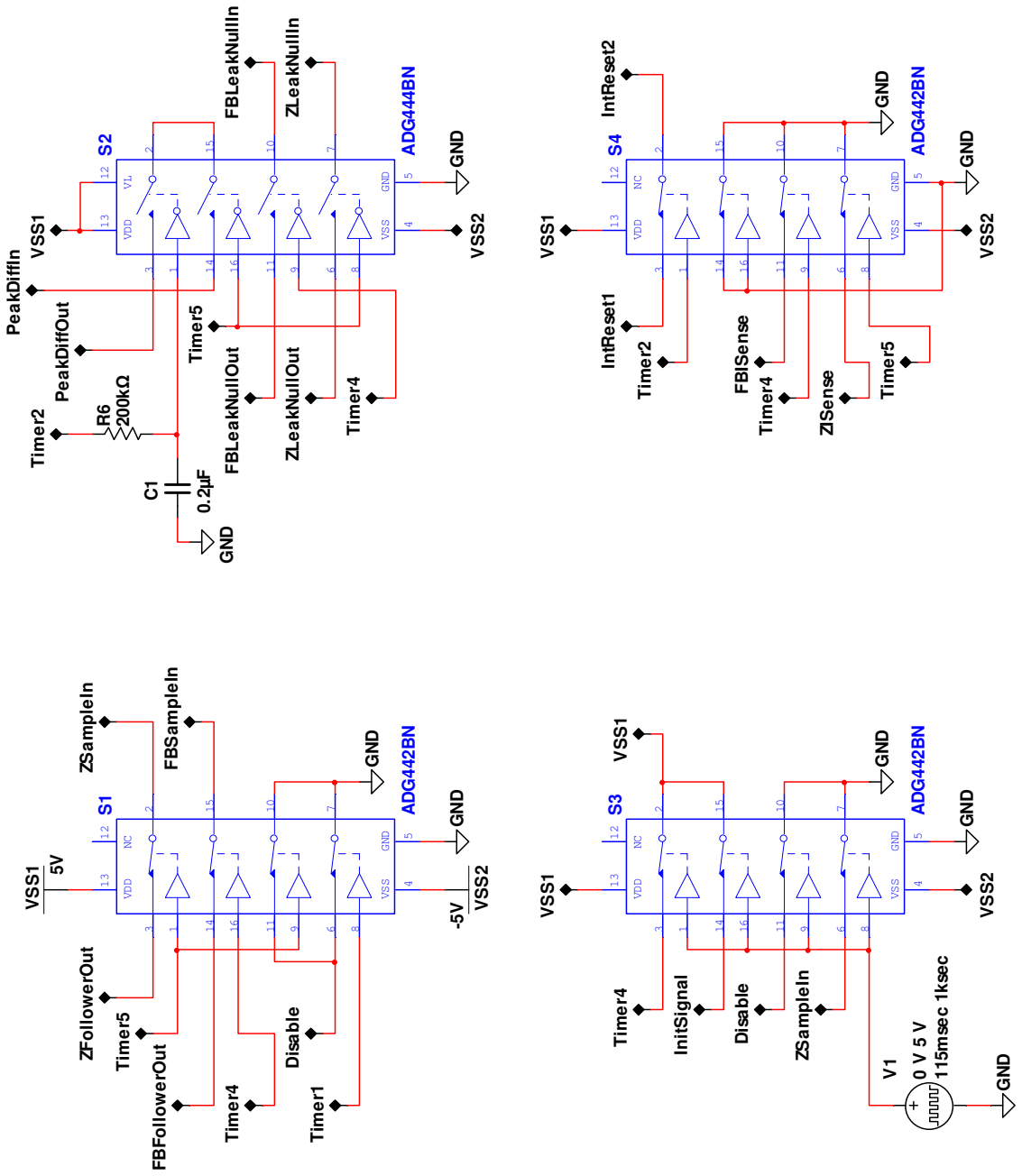

Figure 3.4. T-wave monitor, Model 4c. Top-level schematic, sheet 3 of 4. Analog switches (S1 – S4) and initialization pulse voltage source (V1).

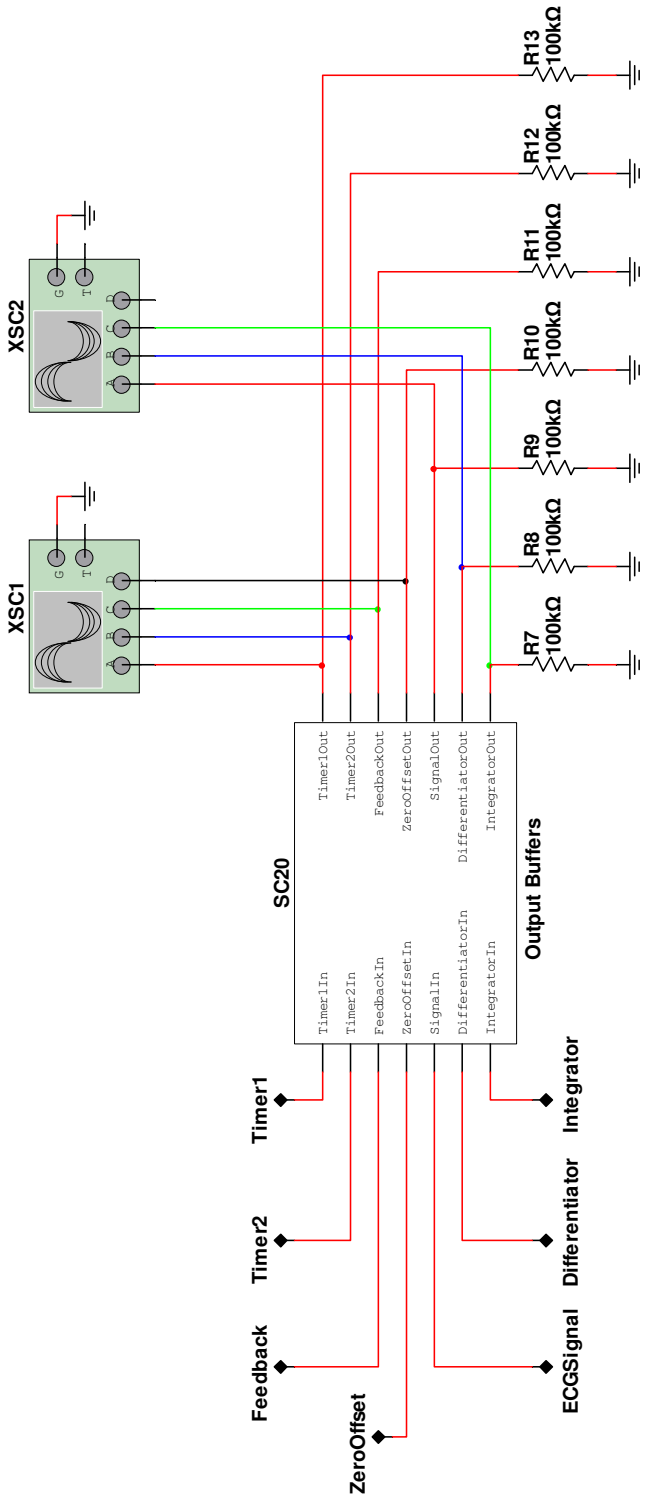

Figure 3.5. T-wave monitor, Model 4c. Top-level schematic, sheet 4 of 4. Output buffers and oscilloscopes (XSC1 and XSC2) for recording output data.

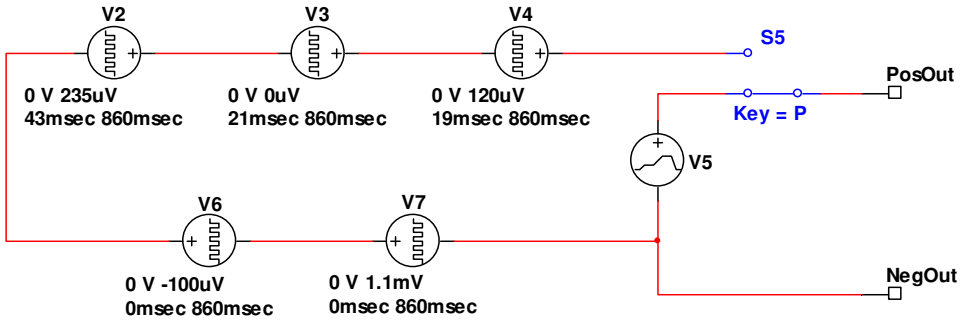

A) Sub-circuit SC1: Input Signals. Simulated ECG signal component sources (V2, V3, V4, V6, and V7) and data file source (V5), switch selectable (S5).

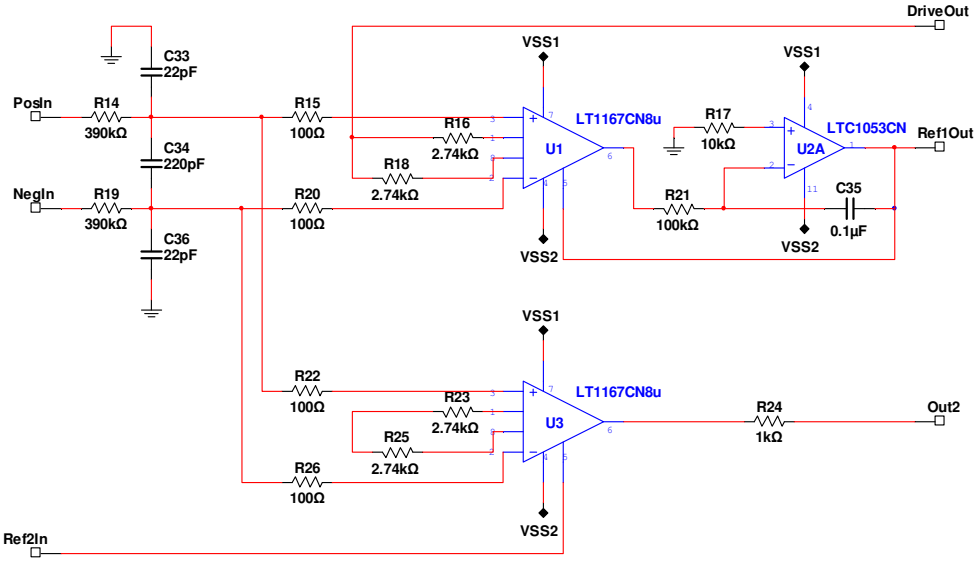

B) Sub-circuit SC2: Instrumentation Amps. Series-R (R14 and R19), RFI filter (C33, C34, C36, R14, and R19), dual instrumentation amplifiers (U1 and U3, gain = 10), and Miller integrator HPF (U2A, f_c = 15.9 Hz).

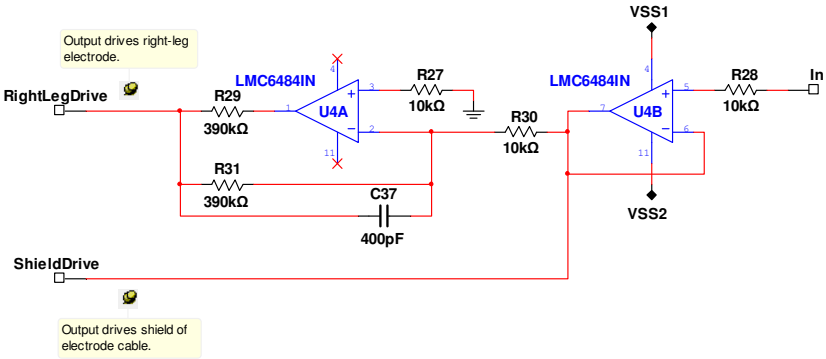

C) Sub-circuit SC3: Right-Leg and Shield Drive.

Figure 3.6. T-wave monitor, Model 4c. Sub-circuits SC1, SC2, and SC3.

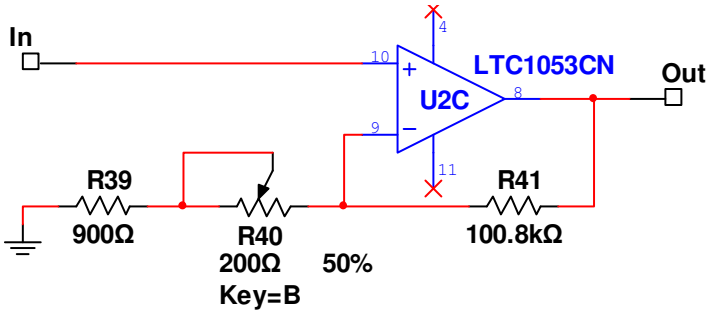

A) Sub-circuit SC5: Gain Amp. Gain = 101.8.

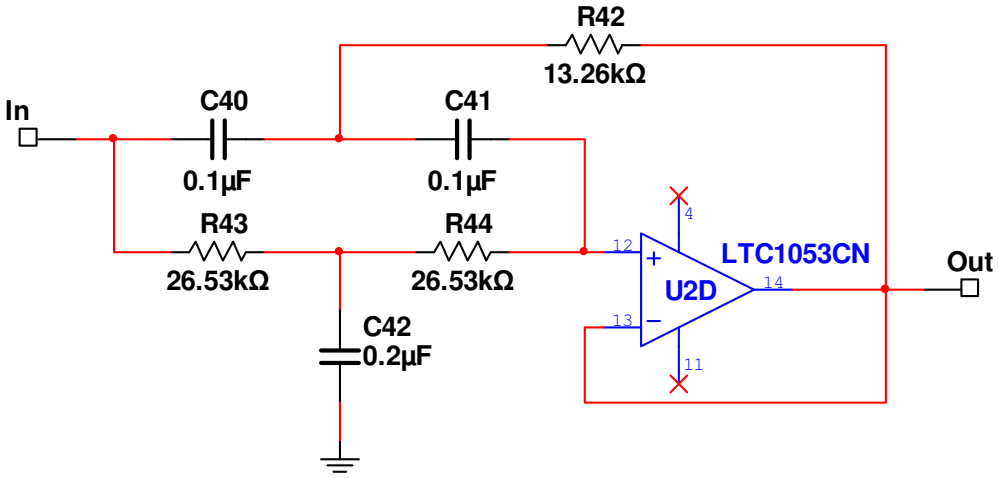

B) Sub-circuit SC6: Notch Filter, 60 Hz. Passband gain = 1, Q = 0.5.

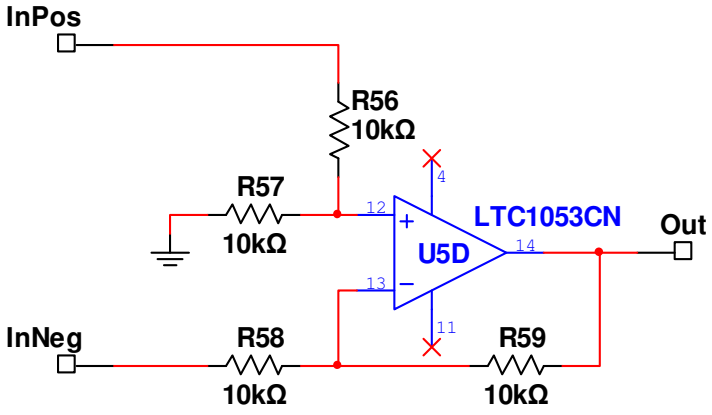

C) Sub-circuit SC9: Difference Amp.

Figure 3.7. T-wave monitor, Model 4c. Sub-circuits SC5, SC6, and SC9.

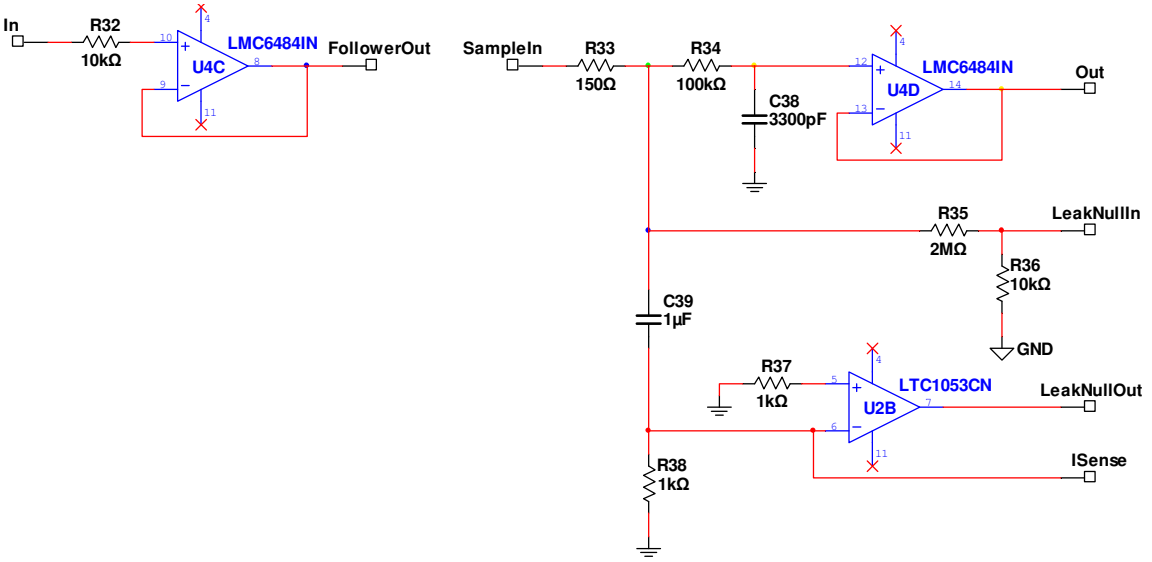

A) Sub-circuit SC4: Feedback S&H. Same as sub-circuit SC8: Zero-Offset S&H, except for reference designators.

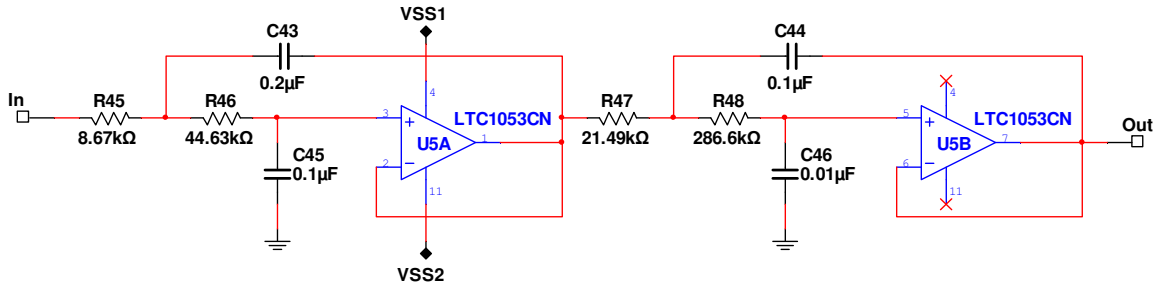

B) Sub-circuit SC7: Bessel LPF, 40 Hz. Passband gain = 1.

Figure 3.8. T-wave monitor, Model 4c. Sub-circuits SC4, SC7, and SC8.

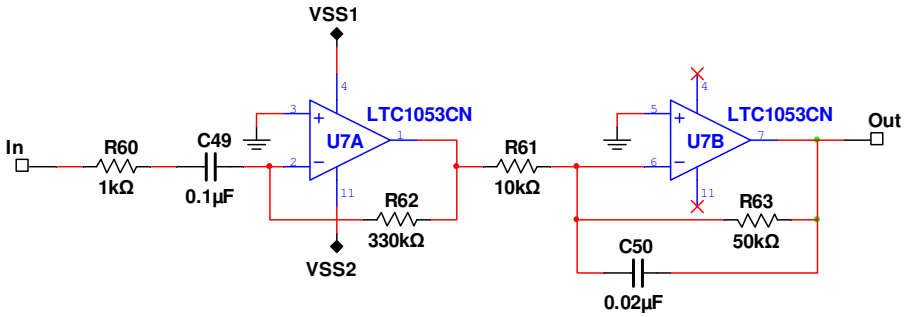

A) Sub-circuit SC10: Differentiator. Differentiator f_{0dB} = 4.82 Hz. Inverting LPF (U7B) f_c = 159 Hz, passband gain = -5.

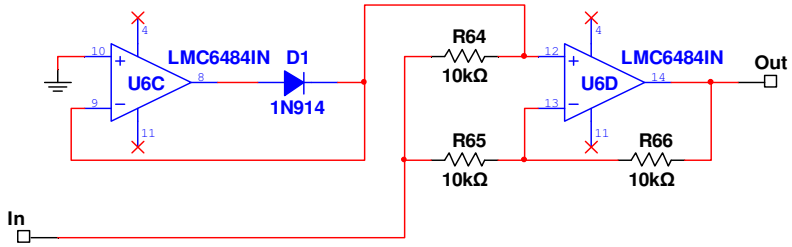

B) Sub-circuit SC11: Full-Wave Rectifier.

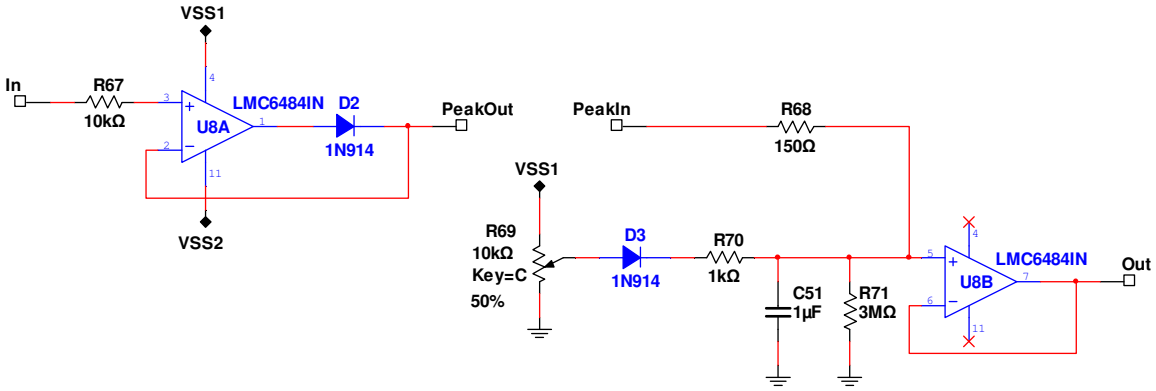

C) Sub-circuit SC12: Differentiator PD. Charge τ = 150 µs, decay τ = 3 s.

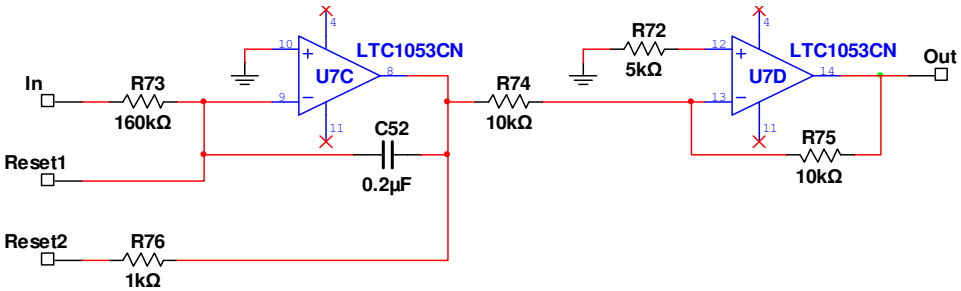

D) Sub-circuit SC13: Integrator. Integrator f_{0dB} = 4.97 Hz.

Figure 3.9. T-wave monitor, Model 4c. Sub-circuits SC10, SC11, SC12, and SC13.

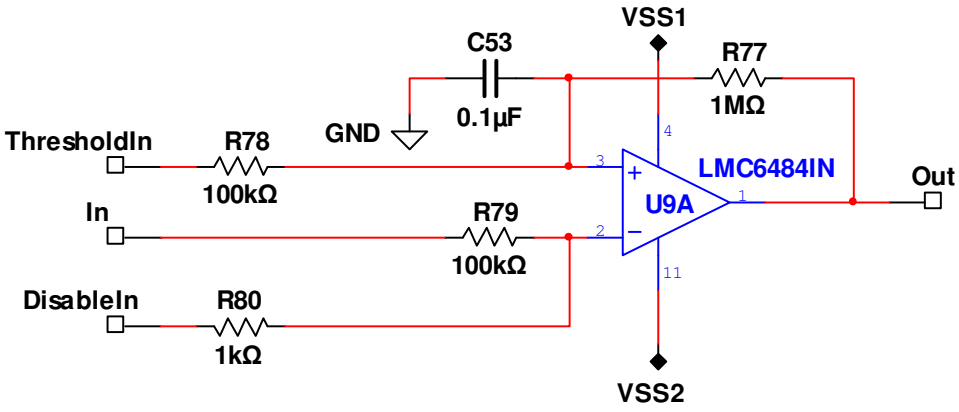

A) Sub-circuit SC14: Schmitt Trigger.

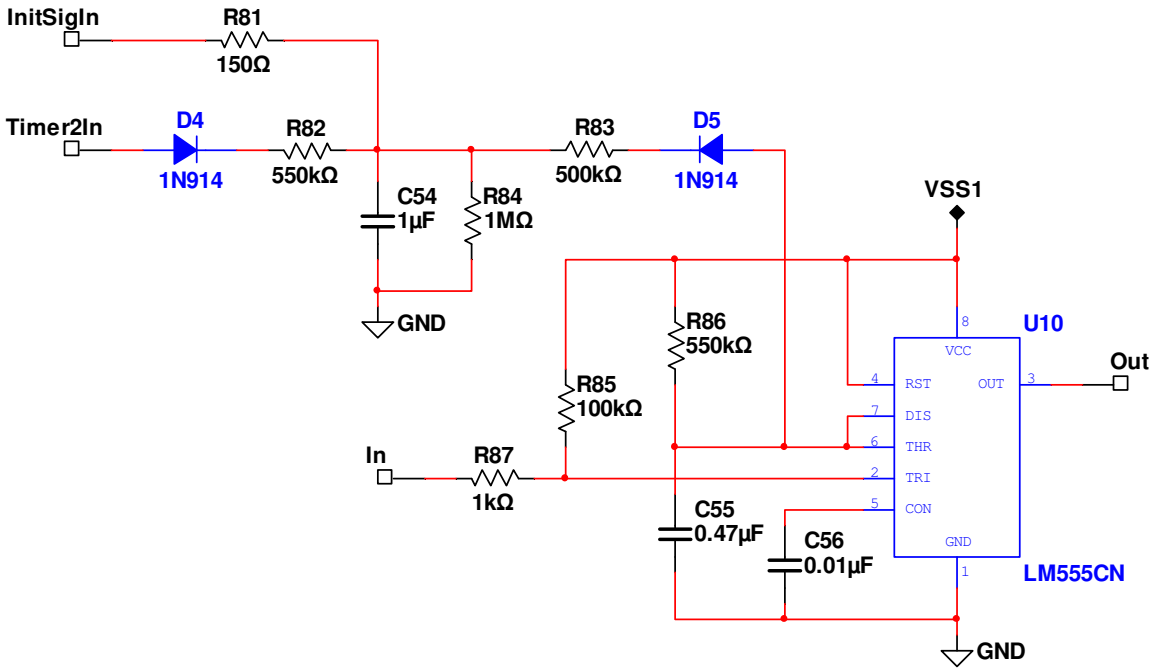

B) Sub-circuit SC15: Timer 1, 309-516 ms.

Figure 3.10. T-wave monitor, Model 4c. Sub-circuits SC14 and SC15.

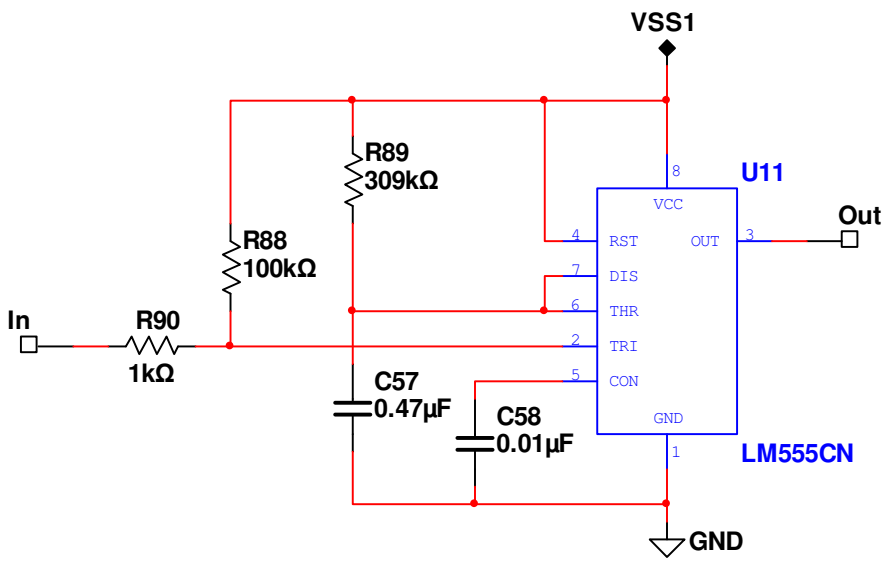

A) Sub-circuit SC16: Timer 2, 160 ms. Same as sub-circuit SC17: Timer 3, 115 ms, except 309 kΩ changed to 222 kΩ.

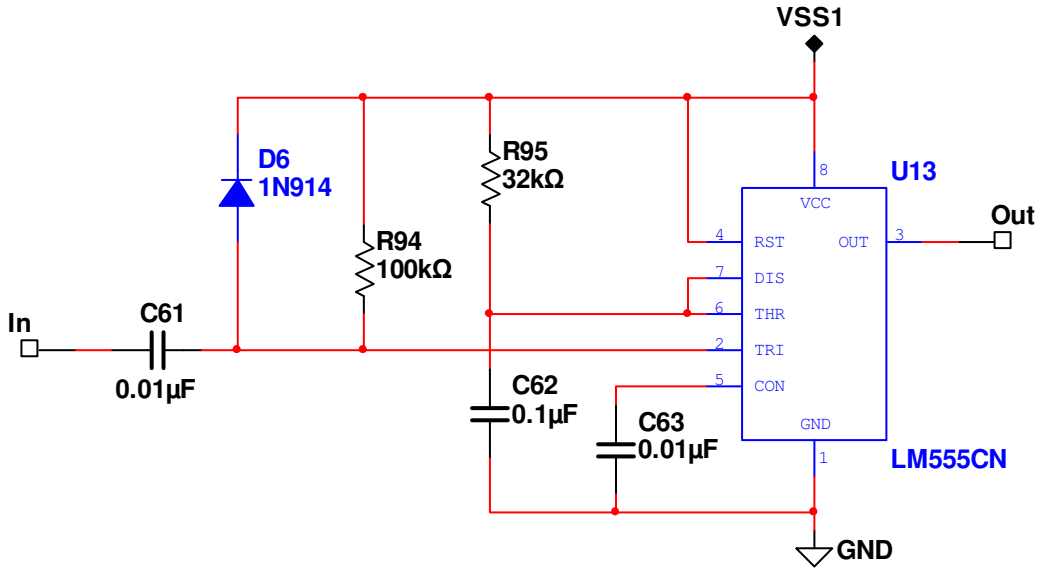

B) Sub-circuit SC18: Timer 4, 3.5 ms. Same as sub-circuit SC19: Timer 5, 7 ms, except 32 kΩ changed to 64 kΩ.

Figure 3.11. T-wave monitor, Model 4c. Sub-circuits SC16, SC17, SC18, and SC19.

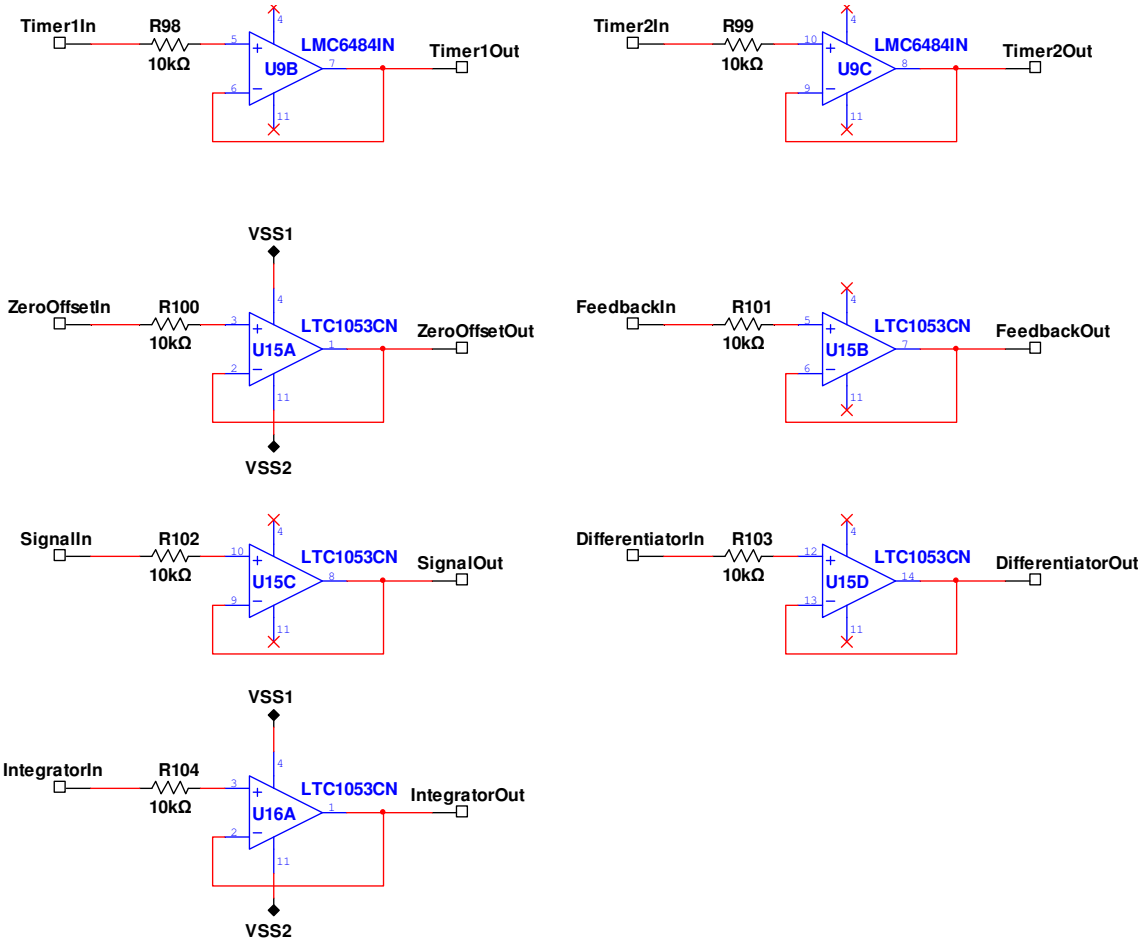

Figure 3.12. T-wave monitor, Model 4c. Sub-circuit SC20: Output Buffers.

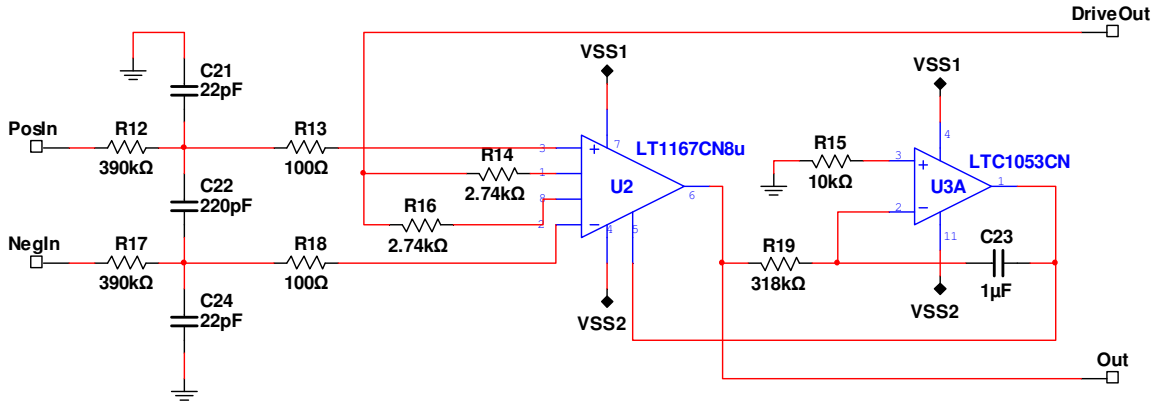

A) Model 1: Single IA (U2, gain = 10) and Miller integrator HPF (U3A, f_c = 0.5 Hz)

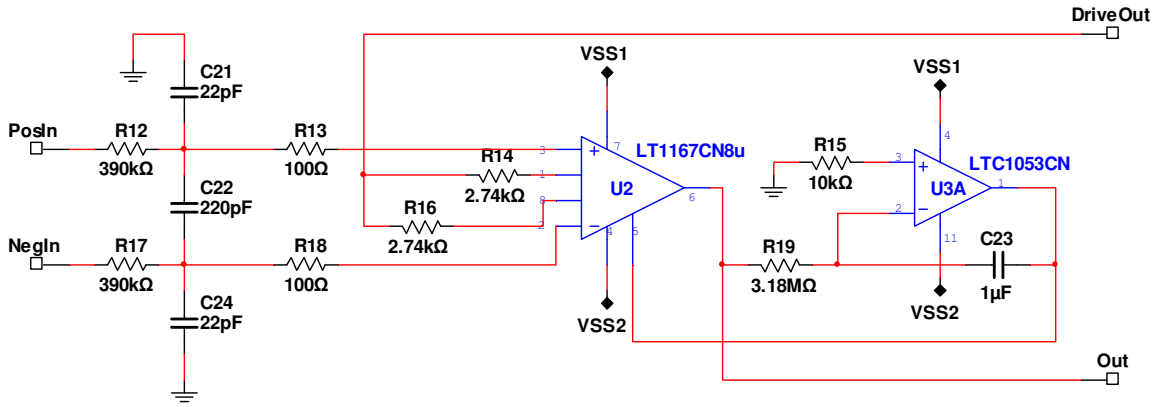

B) Model 1a: Single IA (U2, gain = 10) and Miller integrator HPF (U3A, f_c = 0.05 Hz)

Figure 3.13. T-wave monitor, Model 1 and Model 1a. Feedback S&H, Zero-Offset S&H, Difference Amp, Timer 3, Timer 4, and related circuitry removed. Otherwise, same as Model 4c.

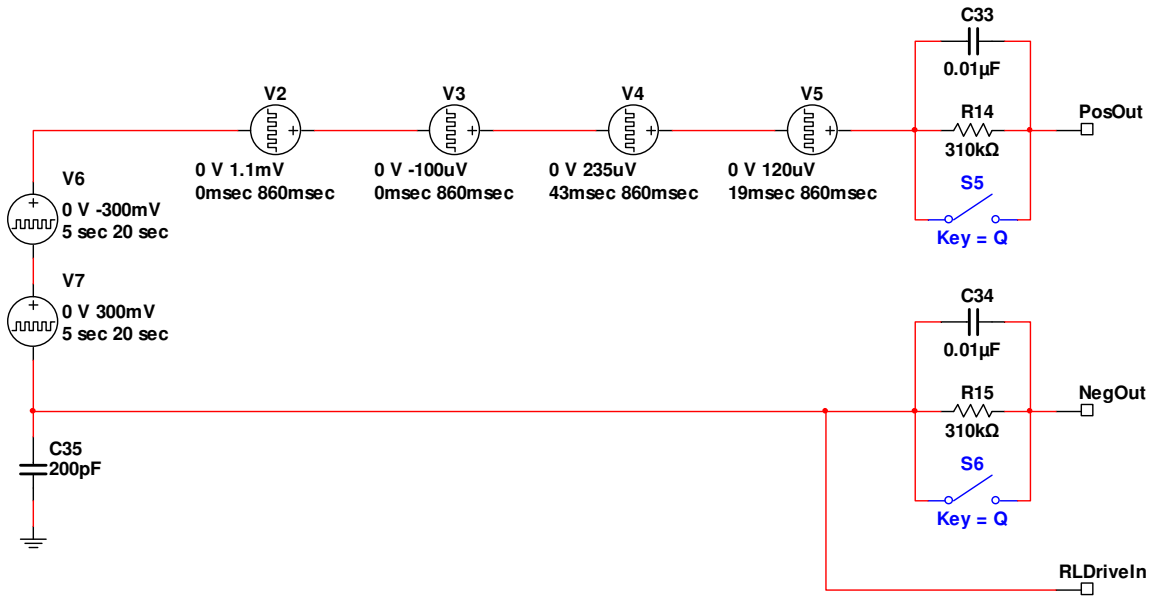

A) Model 4d, Model 1b, and Model 1c. Modification for transient response test: Added ±300 mV step pulse voltage sources (V6 and V7).

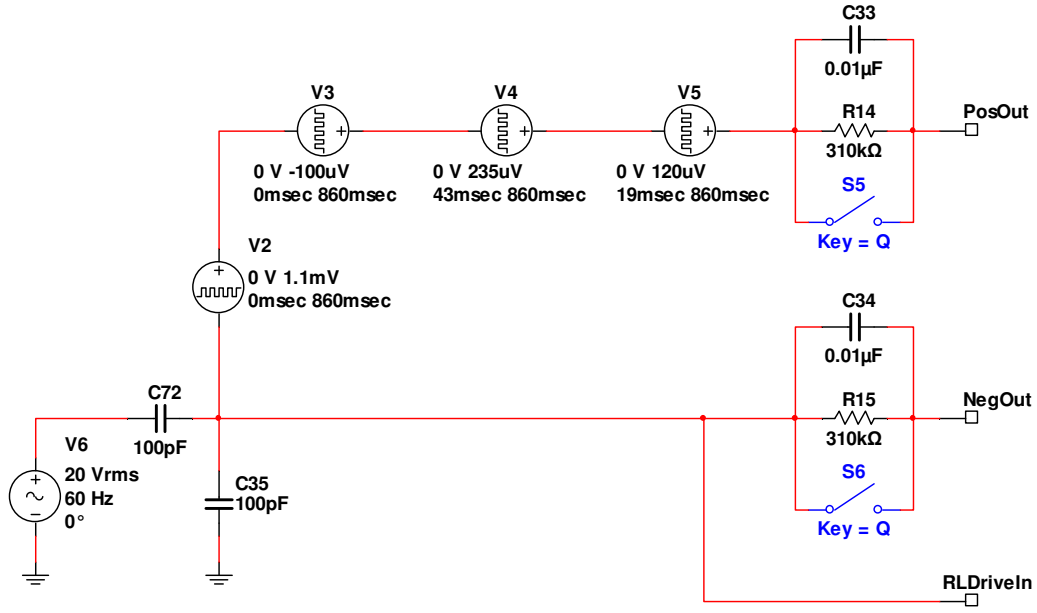

B) Model 4d. Modification for CMR test: Added 20 Vrms 60 Hz sine wave source (V6) and AC coupling/divider (C72 and C35).

Figure 3.14. Modifications for transient response and CMR testing.

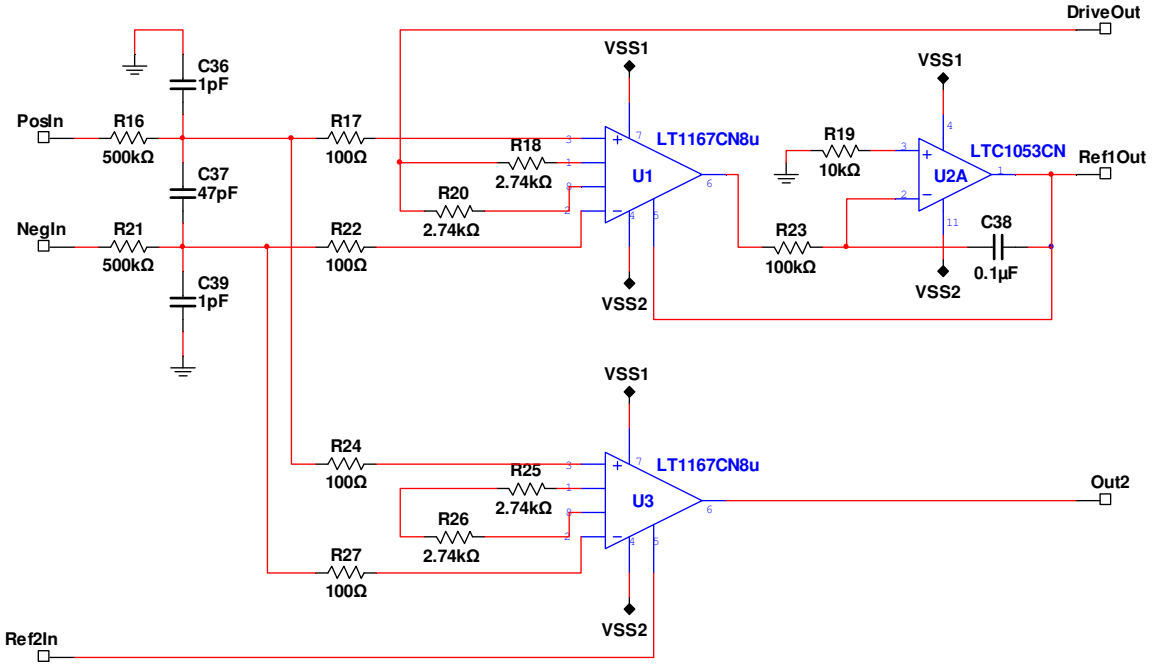

A) Updated series-R (R16 and R21) and RFI filter (C36, C37, C39, R16, and R21).

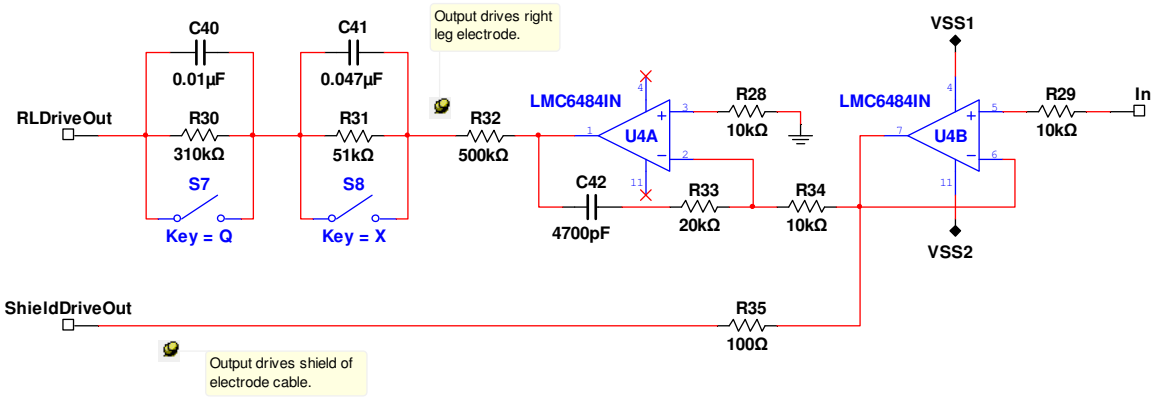

B) Updated RLD. Also includes electrode (C40 and R30) and lead imbalance (C41 and R31) models.

Figure 3.15. T-wave monitor, Model 4d. Updated series-R, RFI filter, and RLD.

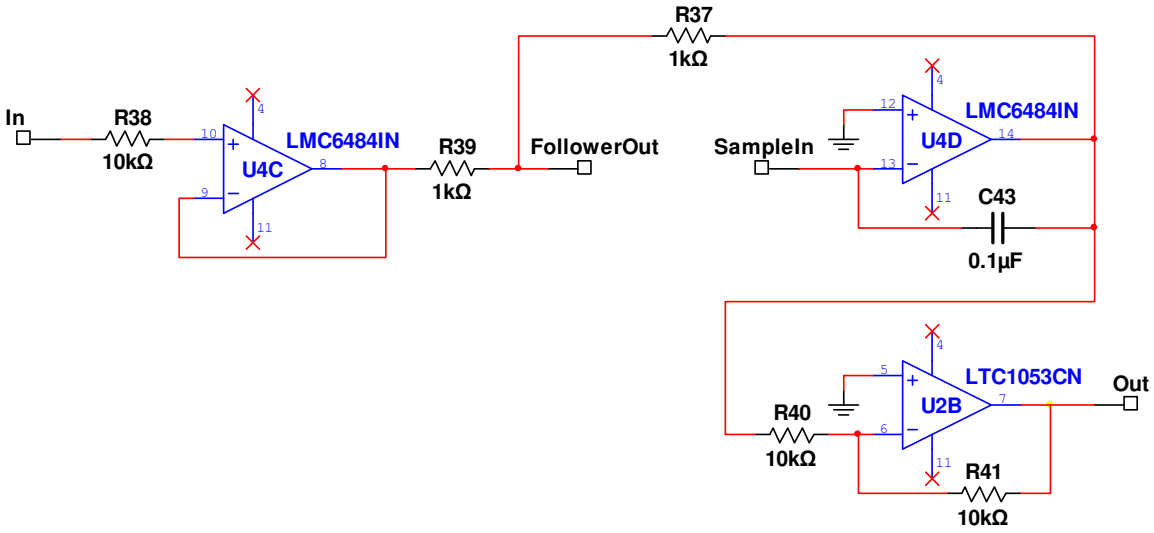

Figure 3.16. T-wave monitor, Model 4d. Updated closed-loop type Feedback S&H sub-circuit. Same as updated Zero-Offset S&H sub-circuit, except for reference designators.

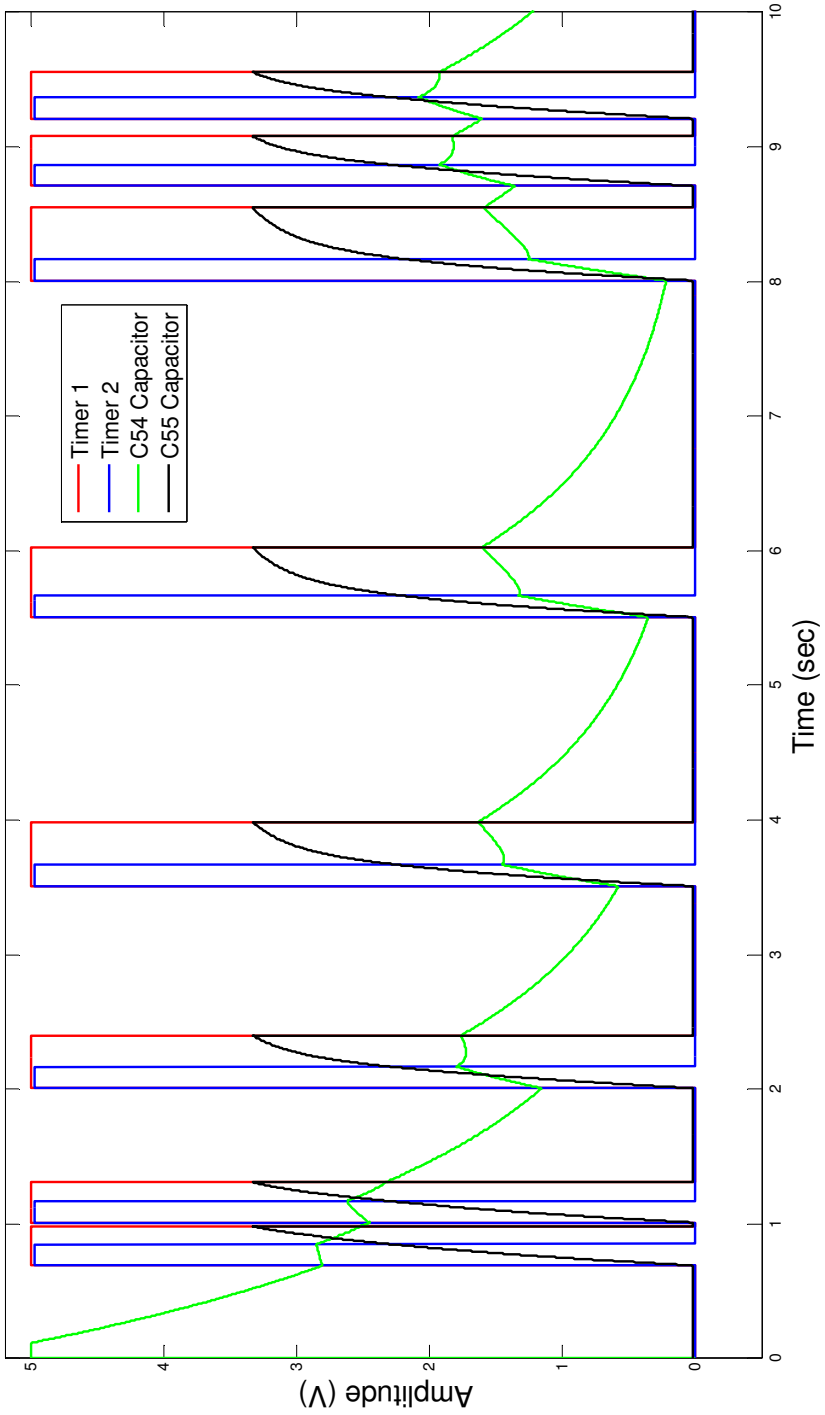

Figure 3.17. Timer 1 (red) responding to a series of staggered trigger signals to demonstrate variable pulse width as a function of heart rate. Trigger timing corresponds to heart rates of 24 to 190 BPM. Also shown are the Timer 2 (blue), C54 (green), and C55 (black) voltage waveforms that underlie Timer 1's behavior.

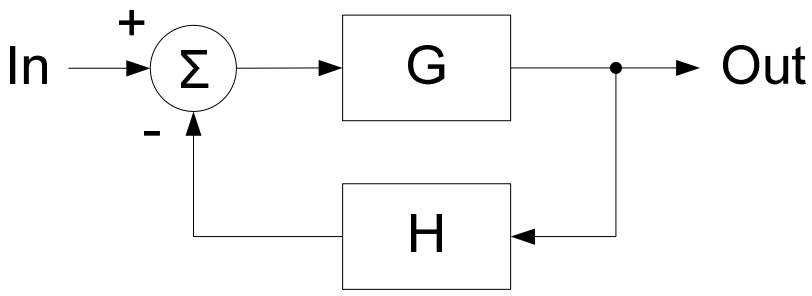

Figure 3.18. Generalized signal-flow diagram of a feedback amplifier.

3.5. ECG Source Data

The ECG signal data used for the T-wave monitor simulation runs came from four sources: the PhysioBank ECG database, synthetic waveshapes constructed within the Multisim environment, the Telemetric and Holter ECG Warehouse database, and the Cardiovascular Engineering Lab of Rutgers, The State University of NJ. The source most often used was PhysioBank, a database archive component of the PhysioNet website (www.physionet.org). Funded by the National Institutes of Health's National Institute of Biomedical Imaging and Bioengineering and National Institute of General Medical Science, PhysioBank provides a large selection of digital ECG signal recordings of both normal and diseased patients (Goldberger et al. 2000). Synthetic ECG signals are also available from the PhysioBank archives. For example, TWA were imbedded into synthetic ECG signals to facilitate testing of TWA detection algorithms. In total, twenty-four segments of control and arrhythmic recordings (some from different places within the same data file) were selected from the PhysioBank database and used for T-wave monitor design, testing, and analysis.

A set of four synthetic ECG signals were constructed within the Multisim environment from a series of pulse voltage sources. As shown in Figures 3.6A, 3.14A, and 3.14B, each of the major ECG signal segments (P, R, S, and T) was designed into a single pulse source and then appropriately time-delayed to create the composite waveshape. The four synthetic variations include one control waveshape (normal T-wave) modeled after the ECG signal of data source # 1, and three other types of T-wave morphologies: inverted T-wave, biphasic T-wave, and elevated ST segment. The

segment parameters, along with calculated T-wave area, T-wave slopes, and RT intervals are listed in Table 3.3.

Two ECG digital recordings were downloaded from the Telemetric and Holter ECG Warehouse of the University of Rochester Medical Center (http://www.thew-project.org). Of particular interest was to test the T-wave monitor design with ECG signals from Holter monitors because they typically have greater amounts of motion artifacts and baseline drift than resting ECG recordings.

The digital ECG source data from Rutgers was recorded using the BIOPAC (BIOPAC Systems, Inc., Goleta, CA, USA) MP35 interface unit. With HPF and LPF cutoff frequencies of 0.05 Hz and 150 Hz, respectively, the analog signal output of the MP35 was digitized at an 800 Hz sample rate and transmitted to a standard PC using a custom 8-bit, wireless ZigBee® network. A copy of this recording was modified to include periodic baseline step-jumps of about 200 μV to simulate minor motion artifacts during the first 20 seconds of data.

Digital ECG signal recordings were converted as needed to a comma-separated-variable file format and fed into the simulated T-wave monitor circuitry via Multisim's piecewise linear voltage source model (V5 of Figure 3.6A). Most simulations ran for 60 seconds. A complete list of the ECG data files used for T-wave monitor testing, along with their source information, recording parameters, and a brief description is provided in Appendix A.

Table 3.3. Parameters for synthetic ECG signals constructed from a series of pulse voltage sources in Multisim. Parameters with blue fill are different from the non-inverted T-wave of data source # 3. R-to-T interval measured from R-wave peak to middle of T-wave pulse width. R-to-T End interval measured from R-wave peak to T-wave end. For biphasic, same R-to-T measurement points, but for T-wave 1 only.

	Non-inverted (Normal)	Initial Value (mV)	Pulsed Value (mV)	Delay Time (ms)	Rise Time (ms)	Fall Time (ms)	Pulse Width (ms)	Period (ms)					
Data Source # 3	R-wave	0	1.1	10	16	16	0	860	Area (mV·s)	Slope Up (mV/s)	Slope Down (mV/s)	R-to-T (ms)	R-to-T End (ms)	
	S-wave	0	-0.1	42	16	75	0	860						
	T-wave	**0**	**0.235**	**200**	**70**	**48**	**43**	**860**	**2.40E-02**	**3.36**	**-4.90**	**265.50**	**335.00**	
	P-wave	0	0.12	710	38	38	19	860						
	Inverted	**Initial Value (mV)**	**Pulsed Value (mV)**	**Delay Time (ms)**	**Rise Time (ms)**	**Fall Time (ms)**	**Pulse Width (ms)**	**Period (ms)**					
Data Source # 4	R-wave	0	1.1	10	16	16	0	860	Area (mV·s)	Slope Up (mV/s)	Slope Down (mV/s)	R-to-T (ms)	R-to-T End (ms)	
	S-wave	0	-0.1	42	16	75	0	860						
	T-wave	**0**	**-0.235**	**200**	**70**	**48**	**43**	**860**	**-2.40E-02**	**-3.36**	**4.90**	**265.50**	**335.00**	
	P-wave	0	0.12	710	38	38	19	860						
	Elevated ST	**Initial Value (mV)**	**Pulsed Value (mV)**	**Delay Time (ms)**	**Rise Time (ms)**	**Fall Time (ms)**	**Pulse Width (ms)**	**Period (ms)**						
Data Source # 5	R-wave	0	1.1	10	16	16	0	860	Area (mV·s)	Slope Up (mV/s)	Slope Down (mV/s)	R-to-T (ms)	R-to-T End (ms)	Area After Timer 2 (mV·s)
	S-wave	0	0.05	34	0	75	0	860						
	T-wave	**0**	**0.235**	**42**	**205**	**68**	**58**	**860**	**4.57E-02**	**1.15**	**-3.46**	**250.00**	**347.00**	**3.64E-02**
	P-wave	0	0.12	710	38	38	19	860						
	Biphasic	**Initial Value (mV)**	**Pulsed Value (mV)**	**Delay Time (ms)**	**Rise Time (ms)**	**Fall Time (ms)**	**Pulse Width (ms)**	**Period (ms)**						
Data Source # 6	R-wave	0	1.1	10	16	16	0	860	Area (mV·s)	Slope Up (mV/s)	Slope Down (mV/s)	R-to-T1 (ms)	R-to-T1 End (ms)	
	S-wave	0	-0.1	42	16	75	0	860						
	T-wave 1	**0**	**0.115**	**205**	**24**	**35**	**21**	**860**	**5.81E-03**	**4.79**	**-3.29**	**213.50**	**259.00**	
	T-wave 2	**0**	**-0.115**	**286**	**35**	**24**	**21**	**860**	**-5.81E-03**	**-3.29**	**4.79**			
	P-wave	0	0.12	710	38	38	19	860						

3.6. Software

Before signal processing and analysis, all oscilloscope data exported from the Multisim T-wave monitor simulation runs were interpolated to create uniformly spaced time vector increments. Interpolation of the spreadsheet-formatted output data was required because Multisim simulation time-step sizes are program-determined per step, up to a user definable maximum step size. To ensure reasonable signal integrity, maximum time steps were limited to less than or equal to 1 ms for all simulations. In keeping with the 1 ms maximum time-step resolution, the MATLAB® interpolation function recreated the signals with a sampling frequency of 1 kHz so that significant data was not lost in the conversion process.

To prevent initialization events from being included in T-wave monitor performance analyses, the first 3 seconds of all simulation runs were ignored. Timer intervals were considered to start or end when the timer pulse reached half its maximum amplitude, 2.5 V. The 2.5 V level roughly corresponds to the minimum Input High Voltage of 2.4 V required by the analog switches used in the simulations (ADG441 2005). Feedback data values were captured at the beginning of the first R-wave (Timer 2 start) and then at the beginning of each T-wave window interval (Timer 2 end) that followed. Similarly, Zero-Offset data values were captured at the beginning of the first R-wave (Timer 2 start) and then at 10 ms after the end of each T-wave window interval (Timer 1 end) that followed. The 10 ms delay allowed for recovery from Timer 5 initiated Zero-Offset step-change transients. The T-wave window interval was defined as when Timer 1 was ON and Timer 2 was OFF.

Prior to extracting feature data from the T-wave, a copy of the filtered ECG Signal was height-adjusted in sections by subtracting the change in Zero-Offset isoelectric line correction that had occurred since the previous heart cycle. In so doing, the signal preceding the most recent Zero-Offset correction – that portion prior to 10 ms after Timer 1 ended – up to the previous Zero-Offset correction was repositioned accordingly. Theoretically, if the Zero-Offset sample were taken from the isoelectric line of the ECG signal, then the T-wave baseline would be corrected to near zero potential by subtracting the Zero-Offset difference. Feedback step-change correction occurs before the T-wave window and is therefore already included in the amplitudes of the T-wave signal.

After Zero-Offset isoelectric line correction, T-wave maximum and minimum amplitudes were extracted from within the T-wave interval window. To avoid signal anomalies that may have occurred near the interval edges, the T-wave window was effectively reduced to 90% of its width by ignoring signal data within the first and last 5%. R-wave (includes S-wave) maximum and minimum amplitudes were extracted from the first 2/3 of the Timer 2 ON interval. The R-wave amplitudes were adjusted to include the Feedback correction differences for reasons similar to those just described for subtracting the Zero-Offset difference from the T-wave signal.

T-wave maximum and minimum area data (integrator output) were extracted from the full width of the T-wave window interval. The maximum and minimum slopes (differentiator output), however, were not. Instead, an algorithm was developed to determine first if the T-wave was non-inverted (normal) or inverted. Slope selection logic, as might be expected, depended heavily on the state of T-wave inversion

classification. In brief, the algorithm seeks the trend of the waveshape within several subsections of the T-wave window by taking its slope average. To illustrate using one straightforward example, if the sign of the average slope within the first subsection of the window investigated was positive and the sign of the average slope in the second subsection was negative, then the T-wave was considered non-inverted. Unfortunately, T-wave morphology was not always this evident.

After the state of T-wave inversion was classified, the maximum and minimum slopes were selected from within the set of window subsections prescribed by the algorithm. By far, the algorithm to assess the state of inversion and then meaningfully place the tangent lines on the leading and trailing edge slopes of the T-wave was the most challenging to design. Refer to the MATLAB® code in the appendixes for more details regarding the inversion classification and slope selection logic.

The selected maximum and minimum slope data were amplitude-corrected by dividing the samples by the RC coefficient of equation (3.6) and dividing again by the gain of the differentiator inverter. The maximum and minimum area data were amplitude-corrected by multiplying the samples by the RC coefficient of equation (3.9) and dividing by the gain of the integrator inverter. The area and slope data were left with the system gain of around 1,000, however, so amplitude units expressed will be reduced by the same factor.

The slope tangent lines of Figure 1.8 and Figure 3.19 were created by solving for the y-intercept, b, in the line equation $y = mx + b$. Here, y is the ECG signal amplitude at the time of the max/min slope, m is the local max/min slope magnitude from the amplitude-corrected differentiator output, and x is the time the max/min slope occurred.

Slope tangent lines created using the completed line equation were initially drawn long enough to span the T-wave window interval. Long slope tangent lines improved the chances of intersection with upcoming horizontal peak lines, a condition desired for reasons explained shortly. The slope tangent lines were later trimmed to the T-wave top and bottom amplitudes.

Under some conditions, the max/min peak amplitudes measured within the T-wave window interval can occur outside of the area framed by the slope tangent lines. For example, if the selected slope magnitudes are small enough, the slope tangent lines can intersect before the T-wave reaches its peak amplitude. Alternatively, artifacts can create large baseline shifts outside of the T-wave segment, but still within the T-wave window interval. Under these types of circumstances, the peak height used for the composite T-wave approximation ($h2$) was adjusted to be the local max/min signal amplitude between the timing of the selected max/min slope data points. The peak height for the composite figure was additionally constrained to be no greater in magnitude than the intersection vertex of the two slope tangent lines, if, indeed, a vertex existed.

Next, horizontal lines that extend to the intersection of the slope tangent lines on either side were created at the composite T-wave peak maximum and minimum amplitudes. Finally, the slope tangent lines were trimmed to meet the horizontal composite T-wave peak max/min lines or the edges of the T-wave window, whichever occurred first, completing one of the geometric T-wave approximations of Figure 1.4. The process of creating the composite T-wave approximation as just described is shown in Figure 3.19.

With the geometric T-wave composite figures completed for each T-wave event within the ECG source file, the composite area of a non-inverted T-wave was calculated as follows, in accordance with the labeling of Figure 1.4:

$$Area\ 1\ = \frac{1}{2}(h1\ +\ h2)(t2 - t1) \tag{3.13}$$

$$Area\ 2\ = h2(t3 - t2) \tag{3.14}$$

$$Area\ 3\ = \frac{1}{2}(h2\ +\ h3)(t4 - t3) \tag{3.15}$$

$$Total\ Area\ = (Area\ 1) + (Area\ 2) + (Area\ 3) \tag{3.16}$$

For inverted T-waves, all heights were treated as positive quantities to keep the formulas for $Area\ 1$, $Area\ 2$, and $Area\ 3$ the same as above. The total area found using equation (3.16) was then multiplied by -1.

Because the integrator output represents the accumulated T-wave area found prior to Zero-Offset isoelectric line correction, the measured T-wave area magnitudes required adjustment. The adjustment process started with identifying the Zero-Offset difference values, as it was with the T-wave peak amplitude adjustments. Instead of a simple amplitude addition or subtraction, however, the Zero-Offset differences were considered to be the overall height ($h2$) of composite figures similar to the ones of Figure 1.4. Again using the slope tangent lines or T-wave window edges to form the outer boundaries of the composite shapes, the correction area was calculated with the same equations used for the composite T-wave approximation area (equations 3.13 through 3.16).

If the Zero-Offset difference was greater than or equal to zero for a given heart cycle, the composite correction area was subtracted from the measured area. Alternatively, if the Zero-Offset difference was less than zero, the composite correction

area was added to the measured area. While it is understood that T-wave morphology can differ from that outlined by the slope tangent lines or T-wave window edges, and that, therefore, the composite correction area adjustment may not be the exact correction needed, the approach was deemed reasonable and pragmatic.

The balance of the software written pertains to T-wave monitor and cardiac data analysis and so is better left for discussion within the context of Chapter 4 and Chapter 5.

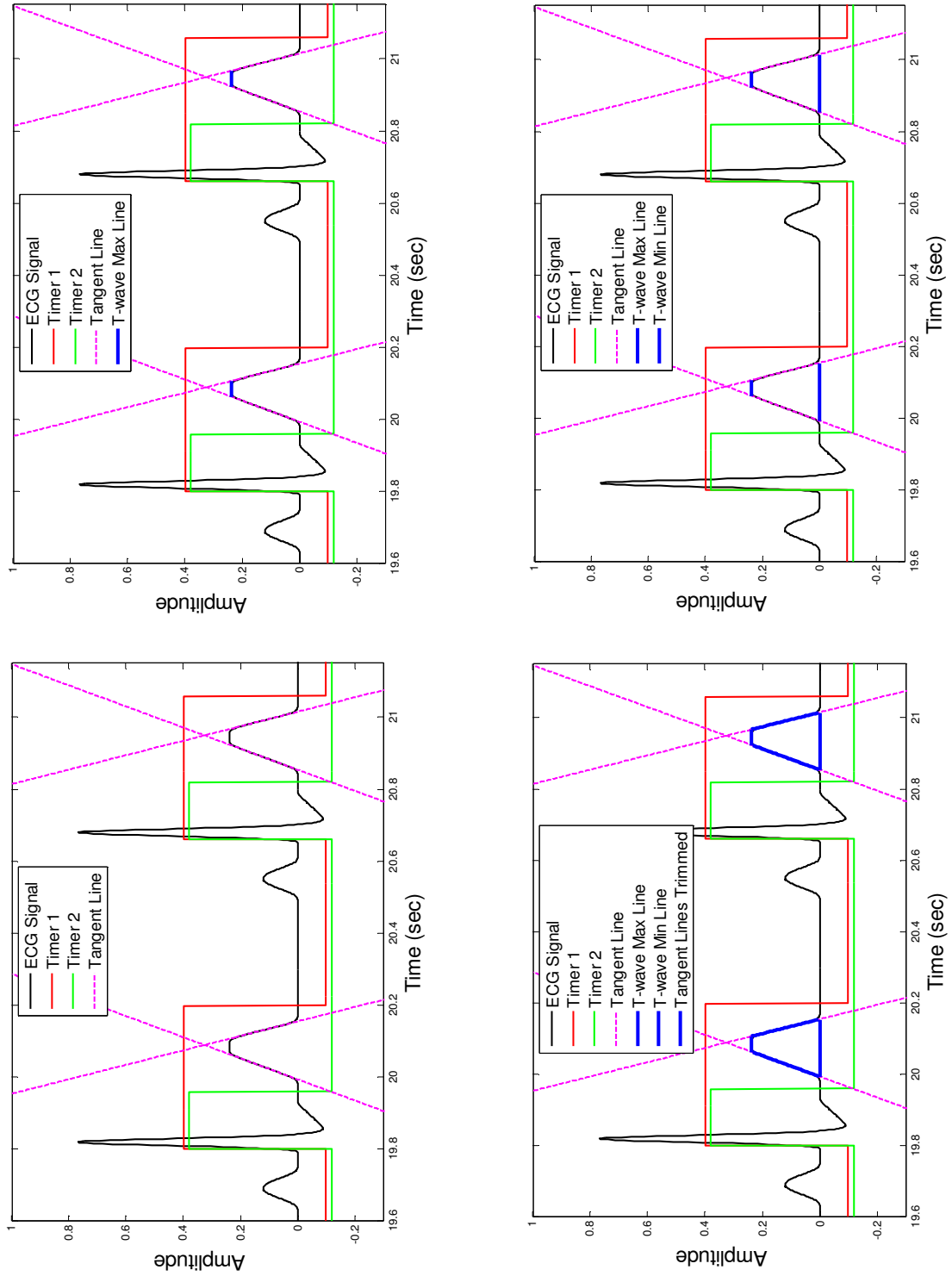

Figure 3.19. Creation of a composite T-wave approximation figure from slope tangent and horizontal max/min T-wave amplitude lines, proceeding clockwise from lower left. ECG signal is data source # 3.

3.7. T-wave Monitor Performance Evaluation

As designed and implemented for proof of concept simulation and testing, evaluation of T-wave monitor performance will rest on the answers to five questions:

1) How effective was the R-wave detection method?
    - Because the T-wave window location (and hence the T-wave) was only defined relative to the onset of an R-wave, successful R-wave detection is key to the balance of the performance results.
    - The R-wave detection method should produce a minimal number of false timer triggers to avoid reporting morphologic data for non-T-wave events.
2) How well did software algorithms identify the T-wave features of interest?
    - If the R-wave was detected correctly, then, presumably, the T-wave will be somewhere within the T-wave window. To create a reasonable approximation of the T-wave, extracted features of interest must be representative of T-wave morphology.
3) How well did the composite T-wave approximation represent the T-wave of the filtered ECG signal?
    - The geometric composites of Figure 1.4 are clearly only approximations of the actual waveshape. In general, however, if T-wave features are identified correctly, the hypothesis states that the geometric composites will be reasonable approximations of several of the typical T-wave morphologies shown in Figure 1.2. The question is, how reasonable were they, if at all?
    - Assessment of how well the composite approximation represents the T-wave is more than just determining how closely the metrics match. Considerations

that are more subjective can be useful when evaluating if, for example, the composite represents the T-wave morphology better than the waveshape appears within the context of a noisy signal. In other words, did the composite extract the underlying T-wave morphology in spite of the waveshape?

- Meaningfulness of the geometric composite implies that clinically relevant information is embedded in its constituent data. Since height is one feature of the T-wave embedded in the approximation figure, an example of clinical use would be the observation of TWA using the composite data exclusively.

4) How near was the isoelectric line to zero potential, in particular during the T-wave segment?
   - Because peak amplitudes and area measures are ideally referenced to zero potential, keeping the isoelectric line near zero by means of the Feedback and Zero-Offset step-change correction sub-circuits is an important function of the Model 4c T-wave monitor design.
   - Feedback and Zero-Offset step-change correction sub-circuits also serve to keep the ECG signal away from the power supply rails, reducing signal saturation. Therefore, a comparison of baseline zeroing via step-change correction versus high-pass filtering is of interest.
5) How fast did the isoelectric line return to near-zero after baseline disturbances?
   - In Model 4c, transient response is believed improved and the potential for low frequency signal distortion reduced because step-change correction functions are used in place of high-pass filtering. However, step-change correction

transients can be harsh, which sometimes causes re-initialization of the Feedback and Zero-Offset signals, and Timer 1 interval. When they occur, the reset cycles add time to transient recovery.

CHAPTER 4

4. RESULTS

4.1. Introduction

To enhance the evaluation of T-wave monitor function, up to seventeen channels of simulated oscilloscope data were exported from the Multisim environment. With seventeen channels of time and amplitude data, a sampling rate of 1 kHz, and an average simulation run-time of 60 seconds, the data imported into MATLAB® reached excesses of two-million samples per ECG signal source file. Fortunately, under typical operational circumstances, only seven channels would be required: Timer 1, Timer 2, ECG Signal, Feedback, Zero-Offset, Differentiator, and Integrator (the shaded blocks in Figure 1.5). Further, most of the data needed for real-time processing would be discrete time and amplitude samples from a relatively few points per heart cycle (eleven, if no R-wave height data extracted).

Two of the additional Multisim oscilloscope channels imported into MATLAB® provided access to the original ECG source signal. Critical for input/output comparison, the original source was taken as the differential-mode signal of the IAs – PosOut minus NegOut – as shown in Figure 3.6A. The source input signal was then multiplied by 1,000 to match the gain of the ECG output signal over the T-wave bandwidth (5 Hz nominal).

One hundred and two Multisim simulations were run using the thirty-two ECG source files listed in Appendix A. All but six of these simulations were divided equally amongst the three most tested T-wave monitor designs. These three designs are reintroduced here for convenience as follows:

1) Primary design, identified as Model 4c
    - Has dual IAs as well as Feedback and Zero-Offset step-change baseline correction. Design includes all the functions of Figure 3.2 through Figure 3.12. There is no HPF in the signal path.
2) Comparative ambulatory design, identified as Model 1
    - Has a single IA with a HPF as shown in Figure 3.13A. Cutoff frequency of the HPF is 0.5 Hz. Model 1 does not include Feedback or Zero-Offset step-change baseline correction functions. Related S&H circuits, Timer 3, and Timer 4 are also not included. Timer 5 remains to disable the Schmitt trigger for 7 ms after Timer 1 interval to maintain timing consistency with Model 4c.
3) Comparative diagnostic design, identified as Model 1a
    - Has a single IA with a HPF as shown in Figure 3.13B. Cutoff frequency of the HPF is reduced to 0.05 Hz, but circuits are otherwise the same as Model 1.

The other six simulation runs involve slight variations of the three models listed above and were used to test for ±300 mV offset step-transient response and CMR performance (Figure 3.14A and Figure 3.14B, respectively). These six simulations also included the updated RFI and RLD designs of Figure 3.15A and Figure 3.15B, respectively, and they will be discussed in the Transient Response (4.5) and Common-Mode Rejection (4.7) sections later in this chapter.

Along with the algorithmic implementation of the geometric composite T-wave approximation figure, importing the Multisim simulation data into MATLAB® provided opportunity for statistical measure and graphical observation of T-wave monitor

performance. The differing content each ECG source file produced varied performance results depending on the specific circuit design and source file combination. In four of the thirty-two sources, the ECG data had such short ST segments or long QT intervals that the timer settings were adjusted for all three T-wave monitor models prior to simulation. The need for adjustment indicated that timer parameters require refinement if broader populations are to be included without modification. Timer modifications are listed in Table 4.1.

In an effort to avoid subjectivity where possible, T-wave amplitude, slope, area, and some other measurement performance results were limited to simulation runs that used ECG data sources with known quantities for these features. The only ECG sources that qualified for statistical T-wave feature measurement analysis, therefore, were the synthetic data in files # 3, # 4, # 5, and # 6 of Appendix A. The features for these data sources are quantified in Table 3.3. Unfortunately, the consequence of using so few data sources was that the number of T-waves potentially observed dropped by a factor of about ten.

4.2. R-wave Detection

Excluding the first three seconds for all simulation runs, the combined R-wave (or T-wave) events of the thirty-two ECG source data files, simulated with each of the Model 4c, Model 1, and Model 1a T-wave monitors, totaled 2,604. Regarding the effectiveness of the R-wave detection method, all three models performed well at producing timer triggers for R-wave events. Model 4c performed best with an R-wave detection average of 99.36% (SD = 2.34%). Model 1 ranked last with a detection average of 99.19% (SD = 3.00%). R-waves were missed due to the excessive motion artifact noise (6 of 54 R-

waves) found in data source # 20, heightened P-waves and noise following ectopic beats (2 of 117) in data source # 27, or by tall P-waves with short R-waves (up to 6 of 53) and an R-on-T event (1 of 53) in data source # 28.

Sometimes, however, the R-wave detection circuits produced false timer triggers – triggers not initiated by R-waves. For example, timer events caused by the motion artifacts of data source # 20 or the tall P-waves with short R-waves of data source # 28 were considered false trigger events. Looking at the ratio of correct (R-wave) timer triggers to total timer triggers, Model 1a performed best, correctly triggering the timers an average of 98.85% (SD = 3.95%) of the time, while Model 4c had the lowest score, averaging 98.50% (SD = 4.18%). Motion artifacts of data source # 20 contributed the largest number of false triggers to the data (up to 13 of 61 timer events). Model 4c's slightly reduced performance resulted mostly from false timer triggers caused by large transient step-change correction recoveries, such as those after some of the PVC events in data source # 25.

Figure 4.1 shows the working interrelationship between the various R-wave detection sub-circuits described in section 3.4.2. Figure 4.2 through Figure 4.5 show some examples of the missed R-wave and false trigger events.

4.3. T-wave Features

4.3.1. Inversion Classification

The T-wave's state of inversion was classified (inverted or non-inverted) by the algorithm logic as the first step toward creating a reasonable geometric T-wave approximation. Importantly, the outcome of the classification determined slope selection and T-wave baseline location logic. It needs to be noted, however, that performance of

the state of inversion classification element of the T-wave monitor algorithm was evaluated to some degree on how well the algorithm classified the waveshape that was within the T-wave window interval. In other words, it is understood that moving or resizing the T-wave window interval could have produced a different set of classification results.

A good example of reclassification as a function of window interval modification is found in the extreme ST depression of data source # 25 (Figure 4.6). The T-waves of data source # 25 were classified as inverted, but it is clear by observation of the ECG signal that extending the Timer 1 interval would have produced non-inverted, albeit severely flattened T-wave approximation figures. Data source # 22 (Figure 4.7) demonstrates the alternative non-inverted classification for a similar waveshape with ST depression. For biphasic T-waves, the first dominant morphology was selected as the correct inversion state classification. In all cases, it was decided that consistency of classification logic was more important than the absolute correctness of the clinical T-wave classification for this analysis.

The total number of non-inverted T-waves in the data source files was 2,463. The number of inverted T-waves in the group was much less at 141. From each group, some T-waves were not assessed for inversion classification because of missed R-waves. Other T-waves were incorrectly classified – non-inverted T-waves found to be inverted or vice versa. Including both of these types of errors in the calculations, Model 1 performed best, correctly classifying the non-inverted T-waves an average of 99.87% (SD = 0.51%) of the time. Model 4c performed worst with an average of 99.70% (SD = 0.86%) correct. Again, false timer triggers were the cause for Model 4c's slightly reduced performance.

For the 141 inverted T-waves, the results were a little different. Model 4c and Model 1a both correctly classified the inverted T-waves 100% of the time. Model 1 scored an average of 92.69% (SD = 6.38%) correct. High-pass filtering made the performance difference for Model 1. For data source # 25 (Figure 4.5), Model 1 was the only design that classified any of the T-waves as non-inverted (6 of 59). Since Model 1 and Model 1a are the same except for HPF cutoff frequency (0.5 Hz vs. 0.05 Hz, respectively) and Model 4c has no HPF, it follows that HPF waveshape distortion similar to that shown in Figure 3.1 skewed the slopes enough to alter the inversion classification. Comparison of the original ECG signal to the filtered signal of Figure 4.5A reveals the HPF distortion effects.

4.3.2. Peak Amplitude and Envelope Heights

All max/min peak amplitude measurements were made with respect to zero potential. The differences in model performance were dramatic for the maximum peak T-wave amplitude. Model 4c performed best with an average error of only 1.69% (SD = 0.28%) from the known maximum amplitudes in Table 3.3. Model 1a had an average error of -29.31% (SD = 7.69%) and Model 1 scored worst with an average maximum amplitude error of -35.07% (SD = 12.06%). The minimum peak T-wave amplitude results were similar, with Model 4c having an average error of only 0.94% (SD = 0.65%) and Model 1a having the worst average minimum peak amplitude error of 15.80% (SD = 17.95%). The inclusion of high-pass filtering and the lack of baseline correction in Model 1 and Model 1a designs proved highly detrimental to their performance when measuring T-wave amplitude features.

Another way to measure the T-wave is to find its envelope height, taken generally as the maximum peak amplitude minus the minimum peak amplitude within the T-wave interval window. In the special case where the T-wave baseline is positioned at zero potential, the envelope height is the same as the peak max/min height. Because of Feedback and Zero-Offset baseline step-change correction, Model 4c is more likely to have the special case condition exist than with the other two models.

Using the T-wave envelope height approach, and thereby ignoring some of the non-zero baseline error, the three models performed more evenly. Model 4c had an average T-wave envelope height error of 1.66% (SD = 0.29%). Model 1a was a close second with an average error of 2.44% (SD = 1.06%). Model 1, with its HPF waveform distortion hampering the accuracy of its output, performed worst with an average envelope height error of 7.16% (SD = 8.04%).

Figure 4.8 (non-inverted T-wave) and Figure 4.9 (inverted T-wave) compare the max/min peak and envelope height measurement performance of Model 1, Model 1a, and Model 4c using data source # 3 and # 5, respectively. As will be discussed more in section 4.3.4, peak height measurement errors are indicative of area errors and both are influenced by T-wave morphology.

4.3.3. Slopes

T-wave slope feature extraction is a more subjective and complex task than was measuring T-wave height features. Here, max/min indicates the local max/min slope selected by the algorithm after the state of inversion classification. Again, only the synthetic ECG signals of Table 3.3 were used to assess slope measurement performance. With an average error of only 0.35% (SD = 2.10%), Model 1a was best at measuring the

maximum T-wave slope. Model 4c performed well with an average error of just 0.77% (SD = 1.97%), while Model 1 had an average error of -2.73% (SD = 9.93%). For the minimum slope selected within the T-wave window interval, all three designs performed comparably: Model 4c averaged 1.78% (SD = 0.02%) error, Model 1a averaged 1.83% (SD = 0.60%) error, and Model 1 averaged 1.88% (SD = 5.57%) error.

4.3.4. Area

Peak positive T-wave area represents the maximum positive (>/= 0) output from the integrator sub-circuit over the full T-wave window interval. Similarly, peak negative area represents the most negative (< 0) integrator output over the same interval. Measured areas were compared to the calculated areas of Table 3.3. For the positive areas, Model 4c performed much better than the other two designs with an average positive area error of only 2.48% (SD = 0.69%). Model 1a had a much poorer performance with an average -51.27% (SD = 9.77%) error. Model 1 was worse yet with an average positive area error of -58.27% (SD = 13.47%). As before with the T-wave peak amplitudes, the inclusion of high-pass filtering and the lack of baseline correction in Model 1 and Model 1a designs caused the large performance disparity. Refer to Figure 4.8.

The results for peak negative area measurements were surprisingly different. The design having the least average negative area error was Model 1 at -0.55% (SD = not applicable). Model 4c had an average error of 0.99% (SD = not applicable) and Model 1a fell to last place with an average negative area error of 4.97% (SD = not applicable). Data source # 5 (inverted T-waves of Figure 4.9) was the only waveform in the group with a net negative area. Use of a single data source file is the reason for the *not*

applicable (na) standard deviations. In addition, the inverted (negative) T-wave amplitudes tended to balance the R-wave (positive) amplitudes so that the signal average, and hence the baseline via the HPF effect, was pushed closer to zero for this data source simulation. Consequently, the negative area performance improved significantly for Model 1 and Model 1a. The non-inverted T-waves have the opposite influence, driving the baseline well below zero (Figure 4.8). This was especially true for Model 1, with its higher HPF cutoff frequency.

Nevertheless, the baseline error and HPF waveshape distortion of Model 1 coincidently combined to produce the best average negative area performance for data source # 5. This particular result, however, should not be interpreted as indicating Model 1's superior performance. Rather, it is the result of a set of serendipitous circumstances.

The integrator output at the end of the T-wave window interval represents the net area measured. The results for the net area error were similar to the positive area error. This was not surprising since there were more data source waveshapes with positive area than negative. Model 4c had an average net area error of 1.84% (SD = 1.05%), followed by Model 1a with -36.75% (SD = 36.07%) error, and by Model 1 with -48.91% (SD = 35.77%) average error. The net area of the biphasic T-wave of data source # 4 is zero so percentage error is not possible to report. Nevertheless, Model 4c's average error from zero net area was lowest at $2.14 \times 10^{-4}\ mV \cdot sec$. Model 1 and Model 1a both had average net area errors around $-7.5 \times 10^{-3}\ mV \cdot sec$ for data source # 4.

4.4. Composite T-wave Approximation

The overall height of the geometric composite T-wave approximation ($h2$ of Figure 1.5) was taken as the T-wave envelope defined in section 4.3.2, but with the

constraints imposed by the slope lines discussed in section 3.6. The leading and trailing edge slopes for the geometric composite figure were selected as the local max/min by the algorithm. The accuracies of the heights and slopes of the geometric composite were determined by comparison to the known values for these T-wave features as given in Table 3.3. The accuracy results for height and slope measurements were reported in their respective sections and so do not bear repeating here. The accuracy of the calculated area of the geometric composite figure, however, has yet to be discussed.

4.4.1. Area

Compared exclusively to the data source files of Table 3.3 (biphasic source not included since its net area is zero), Model 4c had the best composite area performance. The average error of the calculated area of the composite versus the actual area of the synthetic waveshape before filtering was 2.66% (SD = 0.68%) for Model 4c. Model 1a had an average composite area error of 4.58% (SD = 0.59%). Model 1 lagged far behind with an average composite area error of 18.25% (SD = 10.18%).

To provide an alternative sense of how well the composite T-wave approximated the ECG signal waveshape, the height of what would be another composite figure was calculated from the already selected slope magnitudes, their relative timings, and the maximum area measured for non-inverted T-waves or the minimum area measured for inverted T-waves. By substituting equations (3.13), (3.14), and (3.15) into (3.16), and using the max/min area measured as the $Total\ Area$, the new equation was solved for $h2$. The resultant height, designated *T-peak Calc*, defines what the height of the composite figure would have been if the slope data had been used in combination with the measured max/min area instead of the measured T-wave envelope data.

Unfortunately, the difference between the composite height and *T-peak Calc* alone does not quantify the approximation's goodness of fit. It too must be factored in with other statistical measures and subjective graphical observation because of potentially flawed slope and/or area data. Nevertheless, deriving *T-peak Calc* did add to the list of comparative data in a way that improved the understanding of algorithmic performance and strengthened the logic used.

Note: Unless otherwise specified, the balance of this chapter includes simulation run data from all thirty-two ECG data source files of Appendix A. In addition, all geometric figures evaluated for goodness of fit (reasonableness) were constructed in response to R-wave initiated timer triggers. False trigger events were ignored.

4.4.2. Reasonableness

As previously stated, the reasonableness criterion for each geometric composite T-wave approximation includes statistical assessment of feature accuracy along with the more subjective observed goodness of fit evaluation. Composite feature accuracy has been discussed within the context of comparison with the control data files of Table 3.3. However, it cannot be assumed that these sometimes high levels of accuracies will translate equally well into the other twenty-eight simulations. In fact, many of the ECG data source signals were chosen specifically to challenge the T-wave monitor designs with their highly arrhythmic behavior and extreme T-wave morphologies.

In response to the ECG signal challenge, two rules of observation were established for this prototype analysis: 1) If the geometric composite was believed to

match the observable T-wave within the T-wave window interval by better than a two-thirds margin, then that approximation figure was classified as reasonable. 2) If the geometric composite appeared to have morphologic character that enhanced the observability of the T-wave when compared to the original ECG signal, then that approximation was classified as better than the original. Clearly, these two rules of observation require that a subjective, case-by-case determination be made for each geometric figure and the T-wave morphology it approximates (almost 7,800). Also clear, though, is that ECG signals are often read and diagnostically annotated by subjective observation, suggesting some clinical support for the methods used.

Of the nearly 2,600 T-waves observed per model (2,592 for Model 4c, 2,589 for Model 1, and 2,590 for Model 1a), Model 4c had the highest number of geometric composite figures considered reasonable approximations of T-wave morphology with an average of 88.80% (SD = 15.41%). Model 1a and Model 1 also had good results with averages of 88.46% (SD = 15.93%) and 86.25% (SD = 19.16%), respectively. The average number of composite figures considered better approximations than the T-wave of the ECG signal was around 4% (SD ~ 8%) for all models.

A geometric composite figure was not considered a reasonable approximation of the observed T-wave for several reasons. These reasons include the effects of baseline drift, motion artifacts, and other non-cardiac transient events, as well as arrhythmic disturbances. The average percentages of composite figures considered less than reasonable approximations are listed along with their cause in Table 4.2. Table 4.2 also summarizes many of the other results discussed in this chapter.

Figure 4.10 and Figure 4.11 show a few examples of geometric composite figures and the T-waves they approximate. Along with some of the other graphs in this chapter, it can be seen that the range of T-wave morphologies tested was diverse. In the case of Figure 4.10, the ECG signal of the healthy patient (data source # 15) is close to ideal. With minimal 60 Hz noise or baseline drift, the tall R-waves are easily detected and the T-waves are reasonably approximated by the geometric composite figures – certainly by better than a 2/3 margin. The composite T-wave assessments for the ECG signals of Figure 4.11 and others were more challenging.

4.4.3. Meaningfulness

To test the geometric composite figure for imbued meaningfulness, the ECG signal must first have data that indicates some aspect of cardiovascular health to the observer. The geometric composite figure, or its constituent data, must then reasonably convey the same aspect of cardiovascular health to the observer. In the simplest case, an ECG signal from Lead I, say, with a non-inverted T-wave having a height of about 0.2 mV and lasting around 200 ms, indicates a normal state of cardiovascular health, with regard to the T-wave segment, in particular. It is believed that the explanations in the preceding sections, the various figures provided, and the data of Table 4.2 have successfully demonstrated that the geometric composite approximation of Model 4c would be able to convey the same state of normal T-wave health. With the same logic and supporting evidence, the claim of demonstrated meaningfulness can be extended beyond the simplest case to several other healthy and non-healthy T-wave morphologic approximation figures. Additionally, the observer will have the benefits that come with the imbedded beat-to-beat T-wave quantitative and relative timing data.

Not so obvious to the ECG signal observer is evidence of TWA or MTWA. Except for the fact that the baseline of the geometric composite is apt to be near zero more consistently, thereby facilitating T-wave height measurements, graphical observation of the composite figure will likely not yield evidence of alternans. The lack of obvious visible difference between those ECG signals with TWA and those without is demonstrated in Figure 4.12. However, the composite's constituent data can be used to identify and convey these subtle alternating patterns (for example, ABABAB...) of T-wave height.

By running the simulations for data source # 31 and # 32, and then graphing the T-wave peak and composite envelope heights (Figure 4.13), or better yet, by taking the beat-to-beat difference of the T-wave peak and composite envelope heights (Figure 4.14), MTWA can be clearly observed in data source # 31 for the first forty-five seconds, or so. By comparison, MTWA are not present in data source # 32. The beat-to-beat T-wave magnitude differences are about 3 μV per beat, riding atop the average T-wave height of about 415 μV, and a lower frequency influence (synthetic respiration component assumed). The close relationship between the graphs of measured T-wave peak height alternans and those expressed in the graphs of the composite envelope heights demonstrates imbued meaningfulness. Further, the composite envelope measure (a differential-mode approach) eliminates common-mode max/min peak height variations, improving the results.

Another example of demonstrated meaningfulness is found in Figure 4.15. Here, the height of the T-wave peak and the composite envelope heights are shown to correlate with the oxygen saturation levels (respiration) of the sleep apnea patient of data source #

7, although the signals are not shown in phase. Again, a close relationship is seen between the measured T-wave peak and the composite envelope height results.

To explore how the other T-wave features – area and slope – were affected by sleep apnea, their magnitudes were graphed in Figure 4.16. Along with the positive area measures, the minimum slope seems to correlate particularly well with T-wave height and blood oxygen levels for this series.

4.4.4. Baseline

The baseline of the geometric composite is the bottom of the T-wave envelope previously defined. Under ideal conditions, the baseline of the composite would be placed at zero potential by the Zero-Offset difference signal subtraction that occurs within the software algorithm. In fact, for the ideal signal conditions found in data source files # 3, # 5, and # 6, the average baseline error from zero was approximately -1×10^{-4} mV for Model 4c. For the same group of ECG control signals, Model 1 and Model 1a had average baseline errors of more than -5×10^{-2} mV, or more than 500 times that of Model 4c.

As small as both these baseline errors seem, consider that they represent a potential 0.05% peak height error for Model 4c, but a 25% error for the other two models, when compared to a nominal T-wave height of 0.2 mV. When analyzed over the full set of ECG signal data files in Appendix A, the results still favored the Model 4c design, but by a much smaller factor of 5:1. Interestingly, the peak height error potential grew to about 5% for Model 4c, but stayed close to the 25% average baseline error for Model 1 and Model 1a.

The graphs of Figure 4.17 through Figure 4.20 show explicit examples of composite baseline performance for the three T-wave monitor models. Many of the other figures in this chapter, however, including the ones that follow Figure 4.20, also give clear examples of composite baseline placement performance. In general, the composite baseline placement of Model 1 and Model 1a tend toward a weighted signal average (Figure 4.8 and Figure 4.9). On the other hand, the composite baseline placement of Model 4c tends toward zero when the Zero-Offset sample is taken from the isoelectric line and is placed at the difference from zero otherwise.

The 60 Hz noise remaining in the filtered signal of data source # 1 (Figure 4.17) created one example where the Zero-Offset step-change correction was not able to zero the composite baseline. However, the baseline is still consistently closer to zero for Model 4c than for the other two models. The sometimes very short TP intervals of data source # 22 (Figure 4.7) and # 27 (Figure 4.3) created Zero-Offset samples taken from the top or the rising slope of the P-wave. Again, the non-isoelectric line sample meant that the baseline was not placed at zero for all T-waves. Nevertheless, the Feedback and Zero-Offset step-change correction functions of Model 4c offer strong baseline placement advantages, as shown in Figure 4.19 and as will be more dramatically demonstrated in section 4.5.

4.4.5. Summary

Although it would not be practical within the scope of this effort to attempt accuracy assessment of the geometric composite in its approximation of the almost 2,600 T-waves attempted per model, it does serve future work to provide average T-wave findings as reported by the composite's constituent data. To enhance realism, results

from synthetic ECG data source files (# 3, # 4, # 5, # 6, # 31, and # 32) were not included. Data source # 2, # 9, and # 25 were also not included to eliminate some data redundancy, some T-wave outliers introduced by compilation data, and the small number of non-synthetic T-waves correctly classified as inverted (59 of 1713). Table 4.4 summarizes the average non-inverted T-wave composite height, max/min slope, area, and baseline placement on a per model basis, along with a few other statistical measures.

4.5. Transient Response

Transient response tests were conducted with slightly updated T-wave monitor designs. The updated designs, Model 4d, Model 1b, and Model 1c, are otherwise functionally similar to Model 4c, Model 1, and Model 1a, respectively. Modifications included the addition of the ±300 mV step pulse voltage sources in series with the input signals (Figure 3.14A), the addition of electrode and lead imbalance models shown in Figures 3.14A and 3.15B, the updated RFI filters of Figure 3.15A, and the updated RLD of Figure 3.15B. Model 4d also included the updated S&H of Figure 3.16.

The pulse voltage sources for Model 4d and Model 1b were configured so that after an initial delay of 5 sec, ±300 mV pulses alternated every 10 sec. Each pulse width was 5 sec. Because of the very slow recovery for Model 1c, the pulse width was increased to 35 sec and the period stretched to 70 sec. With the standard 60 sec simulation run time, only one pulse could be recorded for Model 1c. Model 1c also had the initial 5 sec pulse delay.

The test for transient response from alternating ±300 mV step inputs added to the ECG signal of data source # 3, made another of the significant differences between the three models more evident. Model 4d, without a HPF could respond quickly to the step

changes, but occasionally suffered from reset requirements that added to the time needed for complete transient recovery. Resetting the baseline correction voltages and the Timer 1 interval would sometimes cause errant signal data to be recorded for Model 4d. Under other circumstances, however, Model 4d transient recovery was completed well within one heartbeat. The timing of the input step pulse with respect to Model 4d's timer cycle determined the character of the result.

Model 1b, with its HPF set to a cutoff frequency of 0.5 Hz, could recover completely in around 3 s, but typically had large amounts of slew-related T-wave errors after the ECG signal came out of saturation (about 1.3 s after the input step pulse). As would be expected, Model 1c, with a 0.05 Hz HPF cutoff frequency, responded about 10 times slower than Model 1b. Saturation ended about 13 s after the step input pulse and recovery slew errors lasted another 10 to 15 seconds. However, because the slew-rate for Model 1c was not as fast as for Model 1b, the errors, on average, were less pronounced.

Figure 4.21 through Figure 4.25 highlight some of the key transient response performances of the three T-wave monitor models. Included are graphs showing the placement of the composite T-wave approximation figure during the different phases of transient response and recovery.

The mechanism that keeps signals out of saturation during the ±300 mV input steps for Model 4d (and Model 4c) is the Feedback step-change baseline correction. Unfortunately, as designed, the timers must be triggered to start the correction process. As such, the non-R-wave triggered baseline correction events register recordings of false T-waves (and R-waves) that skew the output data. If these types of reset triggers were

ignored by the algorithm via thresholding, for example, it was found that the transient response data for Model 4d improved tremendously.

The modification of the algorithm to include transient trigger thresholding for Model 4d is justifiable, given that Model 1b and Model 1c inherently ignore one, or more, or many heart cycles after each input step pulse because of ECG signal saturation. As a first attempt, the threshold levels were set to ignore R-wave and T-wave data if their peak magnitudes or their segment envelope magnitudes were greater than ten-times nominal (10 mV for R-waves, 2 mV for T-waves) during their respective timer intervals. In addition, if the timers were triggered and the R-wave envelope was less than 0.15 mV, the R-wave and T-wave data were ignored.

The rationale for ignoring data when there are very large or very small R-wave peak or envelope magnitudes hinges on the assumption that some other stimulus was likely responsible for the timer trigger. If the T-wave amplitudes are extreme, then it is likely that some artifact has disrupted the T-wave signal to the degree of rendering the data untrustworthy. Both of these assumptions and the threshold settings require additional testing over a larger signal group, however.

Modifying the algorithm to ignore some transient timer triggers made a very significant improvement to the average results. The cost of modification was to have some T-waves ignored even though the baseline reset functions had corrected them fully (Figure 4.21). Nevertheless, the results thus far indicate that the loss of a few transient recovery successes is beneficial overall. Comparison of the graphs of Figure 4.26 with those for Model 4d in Figure 4.24 and Figure 4.25 demonstrates the improvement. Table 4.3 summarizes the transient response performance for the three T-wave monitor models

and includes the modified Model 4d response with transient trigger thresholding. Measures are similar to those of Table 4.2.

4.6. Right-Leg Drive

Referring back to equation (3.12) and Figure 3.18, simulations of loop gain GH, made by opening the feedback loop after H (RLD sub-circuit) and using a common-mode input source to drive G (IA sub-circuit), indicate that for Model 4c, Model 1, and Model 1a (RFI filters of Figure 3.6B, RLD of Figure 3.6C, no electrode or lead imbalance models in any leads), unity gain of GH (0 dB crossing) occurs at around 25 kHz. The phase shift at 25 kHz is 169°, yielding a phase margin of 11°. Phase shift of 180° occurs at 31 kHz. Gain of GH at 31 kHz is -2.6 dB, providing a modest gain margin of 2.6 dB. Maximum gain of GH measured 31.8 dB at 0.01 Hz. Theoretical maximum gain of GH is also 31.8 dB.

Under similar conditions, but using Model 4d, Model 1b, or Model 1c designs (RFI filters of Figure 3.15A, RLD of Figure 3.15B, all electrode and lead imbalance models bypassed), simulations indicate the unity gain of GH (0 dB crossing) to be around 20 kHz. The phase shift at 20 kHz is 77°, yielding an improved phase margin of 103°. Phase shift of 180° occurs at 227 kHz. Gain of GH at 227 kHz is -30 dB, providing a much better gain margin of 30 dB. Maximum gain of GH measured 51.9 dB at 0.01 Hz.

The theoretical maximum gain of the RLD for Model 4d, Model 1b, and Model 1c (Figure 3.15B), however, acquires the open-loop gain characteristics of op-amp U4-A at 0 Hz (around 100 dB) (LMC6484 2000). On the other hand, the minimum gain magnitude of this RLD design is 2, which can help keep the product GH away from unity over a wider bandwidth, in some cases. The results indicate that the RLD of Model 4d,

Model 1b, and Model 1c is a higher gain and yet much more stable design than was used in the previous T-wave monitors.

4.7. Common-Mode Rejection

Model 4d was tested for CMR using the common-mode AC source shown in Figure 3.14B to see what effect the noise would have, if any, on the simulation results. The addition of the 20 Vrms 60 Hz common-mode signal to the simulation of data source # 3 made only insignificant differences. All results were within 0.01% of the Model 4d simulation data run without the 60 Hz noise.

A second CMR test was conducted using Model 4d, where, similar to the CMR test setup in the ANSI/AAMI procedures for cardiac and diagnostic ECGs, the right arm (RA), left arm (LA), and RLD leads of Figure 1.5 were all wired to the junction of the 100 pF capacitors through lead imbalance models (51 kΩ in parallel 0.047 μF) as shown in Figure 4.27 (Cardiac 2002; Diagnostic 2007). The switch S7 of Figure 3.15B was closed to bypass the electrode model. During the simulation run, the RLD reduced the CMV from 10 Vrms to 7.75 mVrms (-62.2 dB). As a result, no 60 Hz noise was detectable on the IA, GA, or DA output signals.

Table 4.1. Timer modifications made to accommodate short ST segments or long QT intervals. Refer to Appendix A for ECG Source Data description and Figures 3.10B and 3.11A for timer schematics.

ECG Source Data #	Condition	Notes	Timer 1	Timer 2	Timer 3
10	Short ST	Reduced Timer 1, Timer 2, & Timer 3	min of 262 ms (550 kΩ => 400 kΩ)	120 ms (309 kΩ => 232 kΩ)	75 ms (222 kΩ => 145 kΩ)
28	Long QT	Increased Timer 1	min of 326 ms (550 kΩ => 630 kΩ)		
31	Short ST	Reduced Timer 1, Timer 2, & Timer 3	min of 262 ms (550 kΩ => 400 kΩ)	90 ms (309 kΩ => 174 kΩ)	45 ms (222 kΩ => 87 kΩ)
32	Short ST	Reduced Timer 1, Timer 2, & Timer 3	min of 262 ms (550 kΩ => 400 kΩ)	90 ms (309 kΩ => 174 kΩ)	45 ms (222 kΩ => 87 kΩ)

Table 4.2. T-wave monitor results summary. Values with blue fill represent best in class performance.

	Model 4c (Baseline Correction, No HPF)		Model 1 (HPF @ 0.5 Hz)		Model 1a (HPF @ 0.05 Hz)	
Note: Data in the following section represents aggregate of all data source files in Appendix A. Data includes all timer triggers.						
# of Non-Inverted T-waves Attempted (of 2463)	2451		2448		2449	
# of Inverted T-waves Attempted (of 141)	141		141		141	
Total # of T-waves Attempted (of 2604)	2592		2589		2590	
	Average	**Std Dev**	**Average**	**Std Dev**	**Average**	**Std Dev**
R-wave Detection	99.36%	2.34%	99.19%	3.00%	99.25%	2.76%
Timer Events from R-waves	98.50%	4.18%	98.75%	4.09%	98.85%	3.95%
Non-Inverted T-waves Correctly Classified	99.70%	0.86%	99.87%	0.51%	99.83%	0.52%
Inverted T-waves Correctly Classified	100.00%	0.00%	92.69%	6.38%	100.00%	0.00%
	Average (mV)	**Std Dev (mV)**	**Average (mV)**	**Std Dev (mV)**	**Average (mV)**	**Std Dev (mV)**
Composite Baseline Error (from 0 V)	-0.010	0.029	-0.061	0.082	-0.043	0.081
Note: Data in the following section represents aggregate of data Source #3, #4, #5, and #6 only (Table 3.3 and Appendix A). Data includes all timer triggers.						
# of Non-Inverted T-waves Attempted (of 195)	195		195		195	
# of Inverted T-waves Attempted (of 65)	65		65		65	
Total # of T-waves Attempted (of 260)	260		260		260	
	Average	**Std Dev**	**Average**	**Std Dev**	**Average**	**Std Dev**
T-wave Max Peak Error	1.69%	0.28%	-35.07%	12.06%	-29.31%	7.69%
T-wave Min Peak Error	0.94%	0.65%	11.55%	19.27%	15.80%	17.95%
T-wave Envelope Height Error	1.66%	0.29%	7.16%	8.04%	2.44%	1.06%
Composite Envelope Height Error	1.65%	0.29%	7.16%	8.04%	2.44%	1.06%
T-wave Max Slope Error	0.77%	1.97%	-2.73%	9.93%	0.35%	2.10%
T-wave Min Slope Error	1.78%	0.02%	1.88%	5.57%	1.83%	0.60%
T-wave Pos Area Error	2.48%	0.69%	-58.27%	13.47%	-51.27%	9.77%
T-wave Neg Area Error	0.99%	na	-0.55%	na	4.97%	na
T-wave Net Area Error	1.84%	1.05%	-48.91%	35.77%	-36.75%	36.07%
Composite Area Error	2.66%	0.68%	18.25%	10.18%	4.58%	0.59%
R-wave Max Peak Error	-29.95%	0.19%	-34.69%	1.22%	-34.06%	3.00%
R-to-T (mid) Interval Error	1.07%	2.18%	-5.46%	4.36%	-3.34%	3.04%
R-to-T (end) Interval Error	3.16%	6.90%	2.24%	6.25%	3.06%	6.71%
Note: Data in the following section represents aggregate of all data source files in Appendix A. Evaluations of R-wave timer triggers only.						
Composites Considered Reasonable Approx. of T-wave	88.80%	15.41%	86.25%	19.16%	88.46%	15.93%
Composites Considered a Better Approx. of T-wave	4.20%	8.44%	4.05%	8.34%	4.20%	8.44%
Composites Less than Reasonable from Drift, Motion Artifacts, or other Non-cardiac Cause	9.08%	13.83%	9.83%	14.98%	9.20%	13.95%
Composites Less than Reasonable from Arrhythmia	2.79%	5.26%	4.03%	11.67%	2.95%	6.03%
Composites Open at T-wave Window Start	10.42%	24.36%	14.07%	28.02%	10.88%	25.25%
Composites Open at T-wave Window End	1.32%	3.80%	0.68%	2.05%	0.79%	2.25%

Table 4.3. Transient response results summary. Values with blue fill represent best in class performance.

	Model 4d (Baseline Correction, No HPF)	Model 4d (Baseline Correction, No HPF, Transient Trigger Thresholding)	Model 1b (HPF @ 0.5 Hz)	Model 1c (HPF @ 0.05 Hz)
Note: Data in the following section represents averages from data source #3 (Table 3.3 and Appendix A) with periodic ±300 mV input steps. Data includes all timer triggers.				
# of Non-Inverted T-waves Attempted (of 65)	56	52	47	34
# of Inverted T-waves Attempted	na	na	na	na
Total # of T-waves Attempted (of 65)	56	52	47	34
R-wave Detection	87.69%	87.69%	72.31%	52.31%
Timer Events from R-waves	80.28%	80.28%	82.76%	94.44%
Missed T-waves from Timer Events	16.92%	13.85%	27.69%	3.08%
Missed T-waves from Signal Saturation	0.00%	0.00%	20.00%	47.69%
Non-Inverted T-waves Correctly Classified	100.00%	100.00%	97.87%	100.00%
Inverted T-waves Correctly Classified	na	na	na	na
Avg T-wave Max Peak Error	9.87%	1.62%	-8.57%	-29.18%
Avg T-wave Min Peak Error (form 0 V)	-0.173 mV	-6.992E-04 mV	-0.414 mV	-0.099 mV
Avg Composite Baseline Error (from 0 V)	-0.017 mV	2.358E-03 mV	-0.143 mV	-0.076 mV
Avg T-wave Envelope Height Error	83.66%	1.91%	167.55%	13.03%
Avg Composite Envelope Height Error	11.85%	0.61%	19.55%	2.03%
Avg T-wave Max Slope Error	40.28%	1.94%	13.54%	-3.97%
Avg T-wave Min Slope Error	5.12%	1.93%	-8.17%	-3.47%
Avg T-wave Pos Area Error	11.49%	0.00%	52.86%	132.87%
Avg T-wave Neg Area Error (from 0 mV-s)	0.085 mV-s	-2.692E-03 mV-s	-0.033 mV-s	-0.035 mV-s
Avg T-wave Net Area Error	-31.37%	2.42%	-90.70%	-13.81%
Avg Composite Area Error	39.32%	0.66%	51.23%	9.20%
Avg R-wave Max Peak Error	356.45%	-30.30%	-19.59%	-27.88%
Avg R-to-T (mid) Interval Error	-1.74%	2.80%	-3.57%	-4.96%
Avg R-to-T (end) Interval Error	-3.86%	-0.51%	-4.63%	-3.04%
Note: Data in the following section represents averages from data source #3 (Table 3.3 and Appendix A) with periodic ±300 mV input steps. Evaluations of R-wave timer triggers only.				
Composites Considered Reasonable Approx. of T-wave	91.07%	96.15%	76.60%	85.29%
Composites Considered a Better Approx. of T-wave	0.00%	0.00%	0.00%	0.00%
Composites Less than Reasonable from Drift, Motion Artifacts, or other Non-cardiac Cause	7.69%	0.00%	16.92%	7.69%
Composites Less than Reasonable from Slew Errors	6.15%	0.00%	16.92%	7.69%
Composites Less than Reasonable from Arrhythmia	na	na	na	na
Composites Open at T-wave Window Start	0.00%	0.00%	6.15%	6.15%
Composites Open at T-wave Window End	3.08%	3.08%	1.54%	0.00%

Table 4.4. Non-inverted composite T-wave approximation results summary. Values with blue fill represent best in class performance.

	Model 4c (Baseline Correction, No HPF)		**Model 1** (HPF @ 0.5 Hz)		**Model 1a** (HPF @ 0.05 Hz)	
Note: The following data represents only non-synthetic data source files in Appendix A. Data source # 2, # 9, and # 25 are also not included.						
# of Non-Inverted T-waves Attempted (of 1654)	1648		1645		1646	
	Average	**Std Dev**	**Average**	**Std Dev**	**Average**	**Std Dev**
Composite Envelope Height (mV)	0.263	0.190	0.278	0.192	0.267	0.191
Composite Max Slope (mV/s)	5.83	2.35	5.60	2.42	5.84	2.34
Composite Min Slope (mV/s)	-6.06	3.24	-6.37	3.34	-6.11	3.25
Composite Area (mV-s)	2.34E-02	2.01E-02	2.68E-02	2.30E-02	2.40E-02	2.04E-02
Composite Baseline Placement (mV)	-7.24E-03	2.39E-02	-6.39E-02	8.25E-02	-4.60E-02	6.30E-02
Heart Rate (BPM)	82.4	27.0	82.1	27.3	82.0	27.3
R-to-T (mid) Interval (ms)	265.6	48.8	262.1	48.9	265.9	49.3
R-to-T (end) Interval (ms)	323.2	59.0	321.9	59.6	323.6	59.3

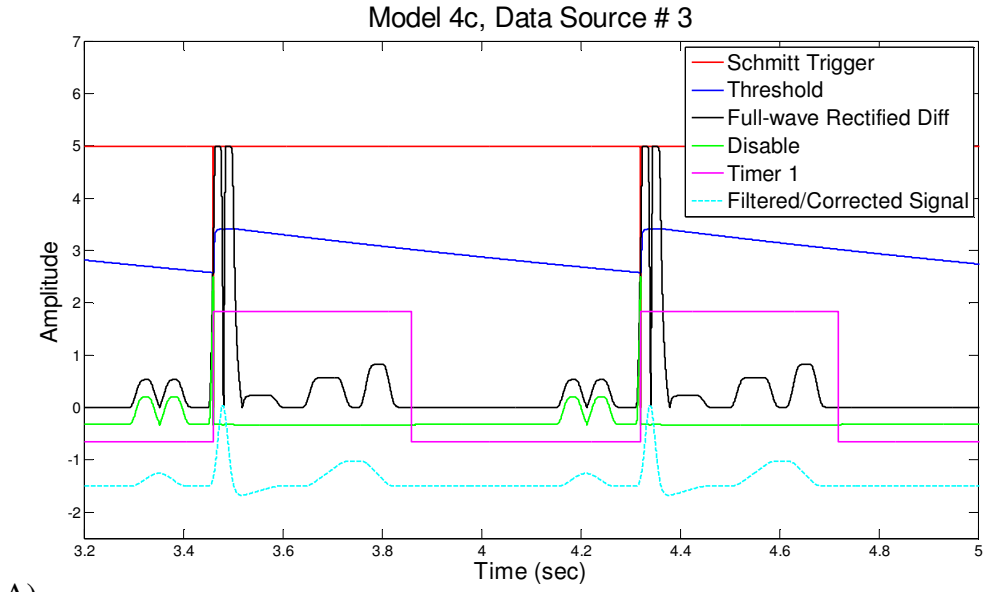

A)

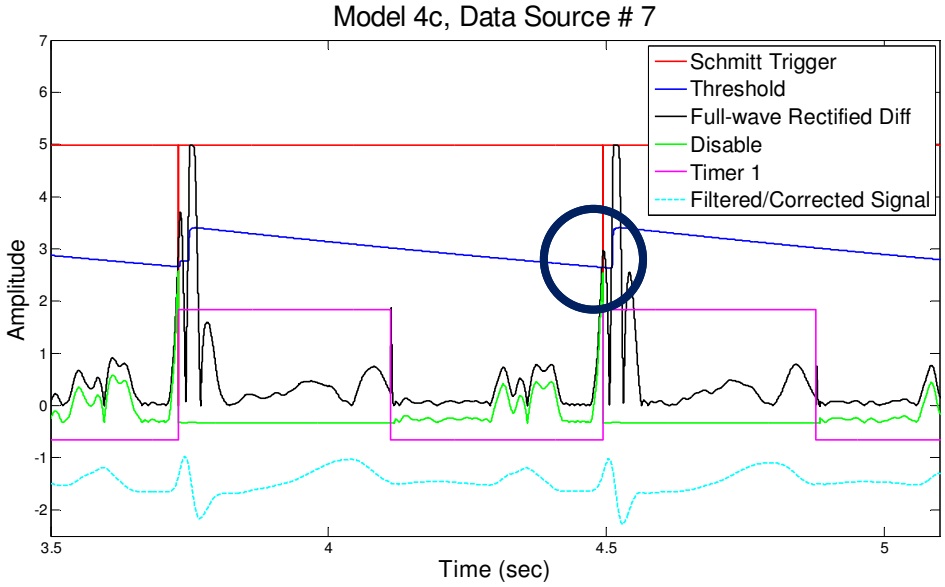

B)

Figure 4.1. Threshold (blue) from peak detector of full-wave rectified differentiator. Schmitt Trigger (red) fires when Disable (green) is not held at zero and Full-wave Rectified Diff (black) rises above Threshold. Timer 1 and ECG signal not shown to scale. Horizontal axis of Disable, Timer 1, and ECG signal offset for clarity. A) Slope magnitude at leading edge of typical R-wave (data source # 3) rises easily above Threshold. B) Slope magnitude at leading edge of small R-wave (data source # 7) rises to just above Threshold (inset circle).

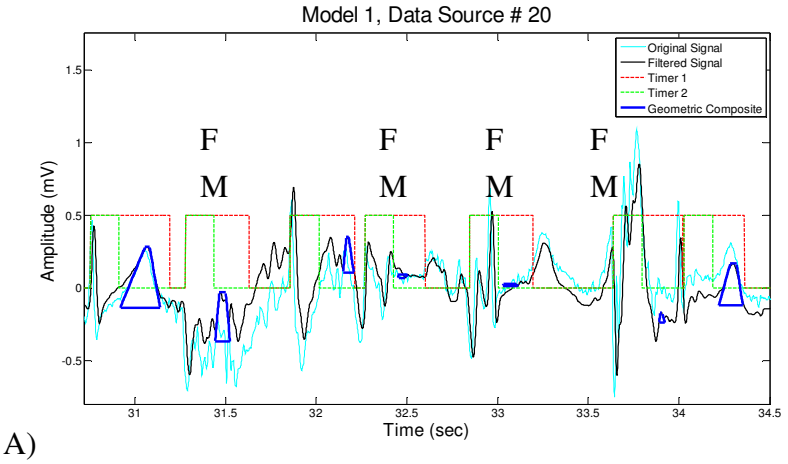

A)

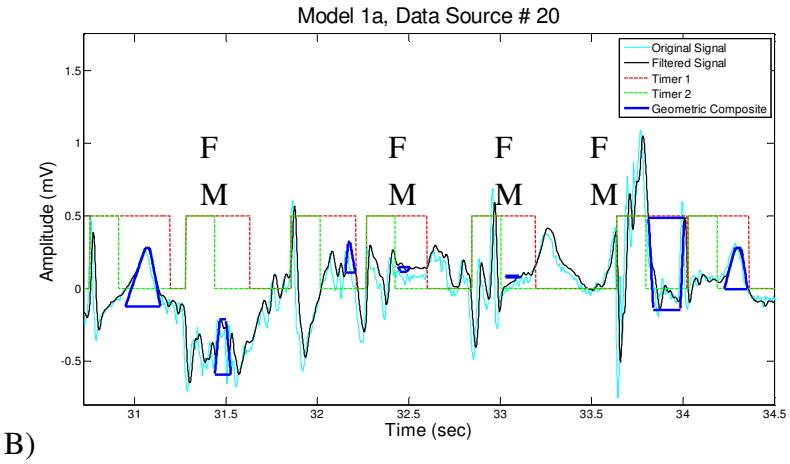

B)

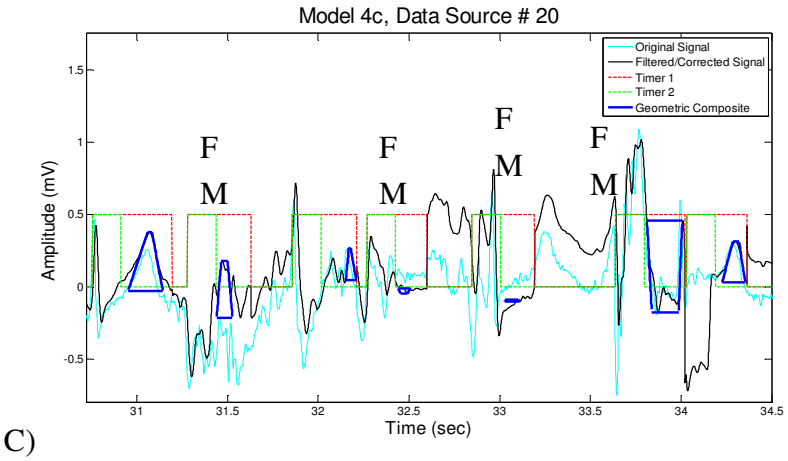

C)

Figure 4.2. Model comparison of false timer trigger (F) and missed R-wave (M) events caused by motion artifacts. Each series starts and ends with an R-wave detection. Note slope selection and placement of composite T-wave baseline for each model. C) Noise causing non-zero baseline placement.

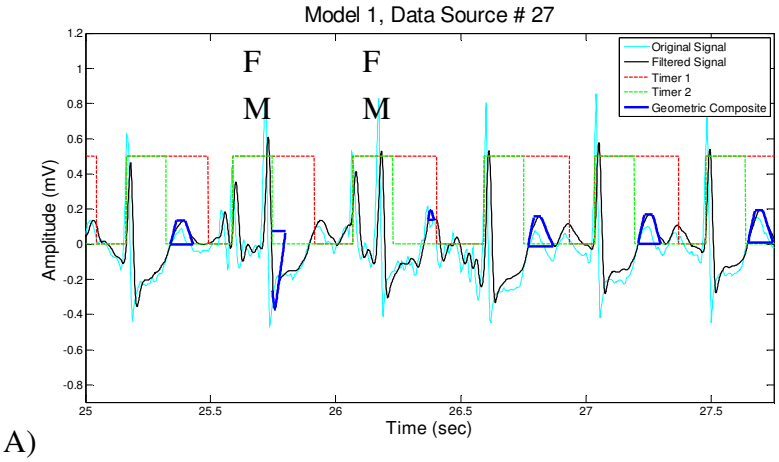

A)

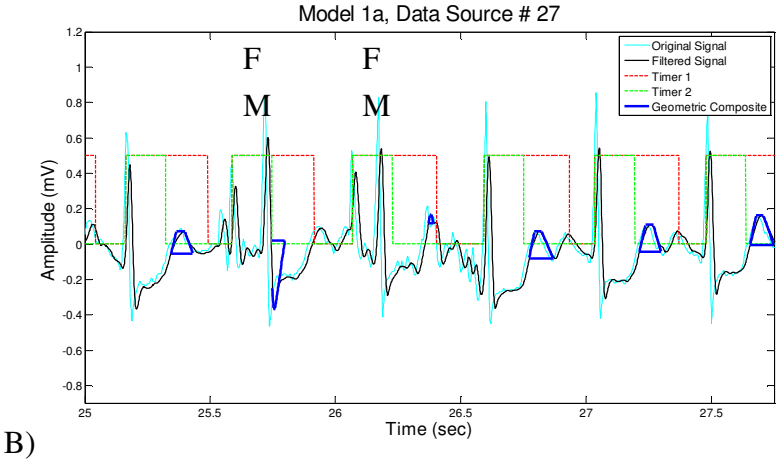

B)

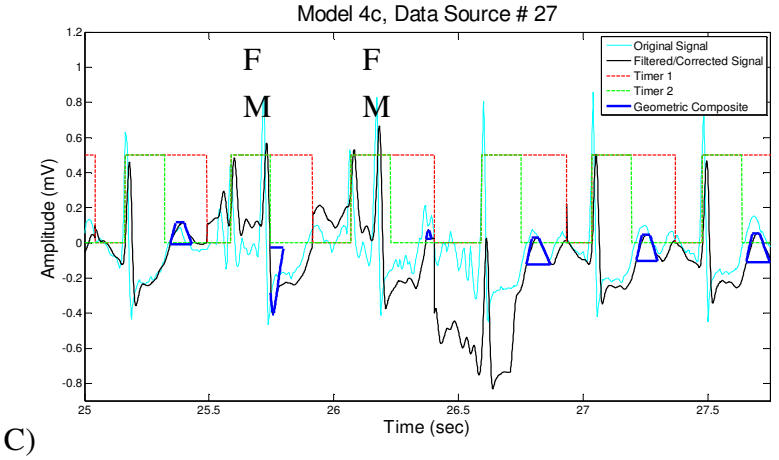

C)

Figure 4.3. Model comparison of false timer trigger (F) and missed R-wave events (M) caused by heightened (noisy) P-wave and small R-wave after ectopic beat. Each series starts and ends with an R-wave detection. Note placement of composite T-wave baseline for each model. C) Very short TP interval causing non-zero baseline placement.

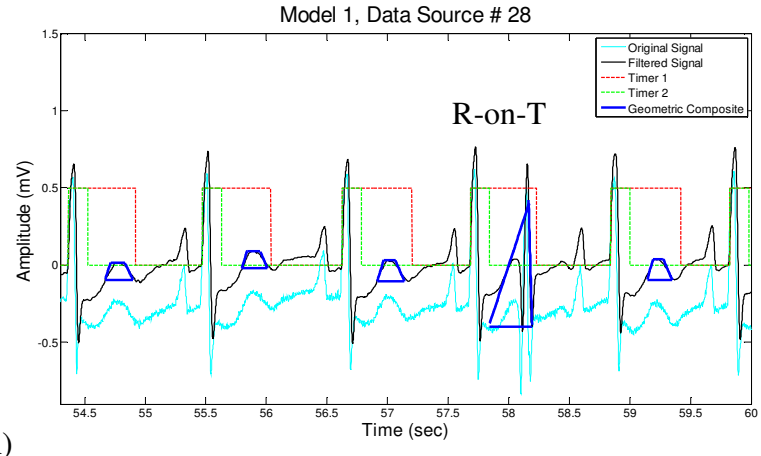

A)

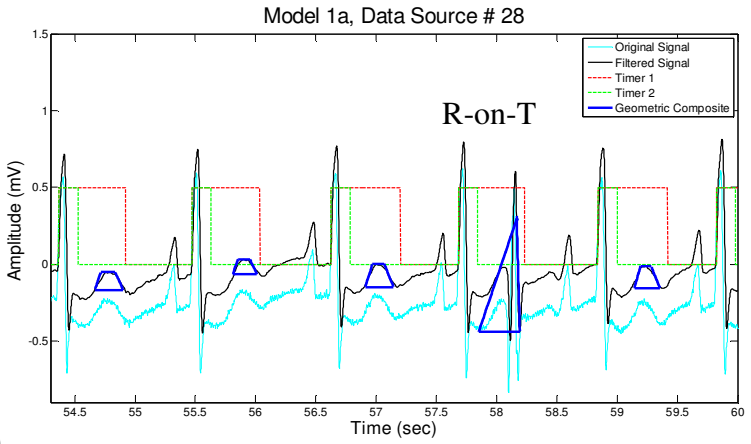

B)

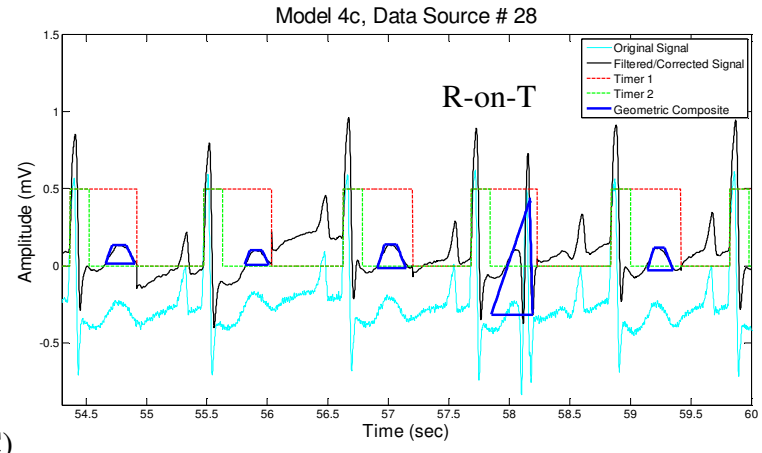

C)

Figure 4.4. Model comparison of disrupted T-wave caused by R-on-T event. Note placement of composite T-wave baseline for each model.

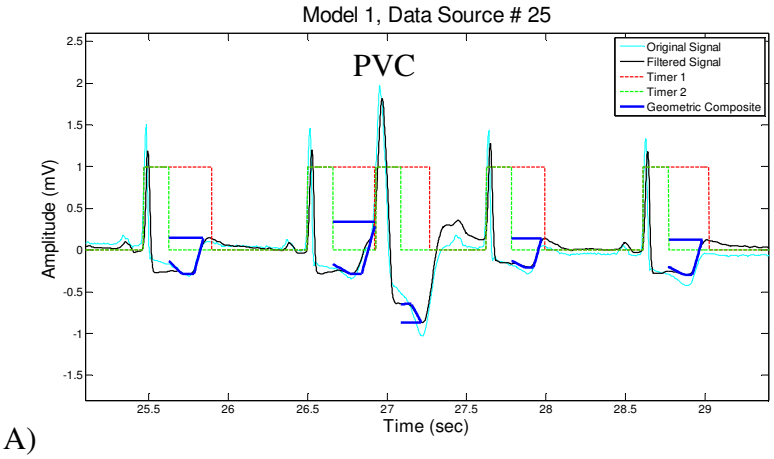

A)

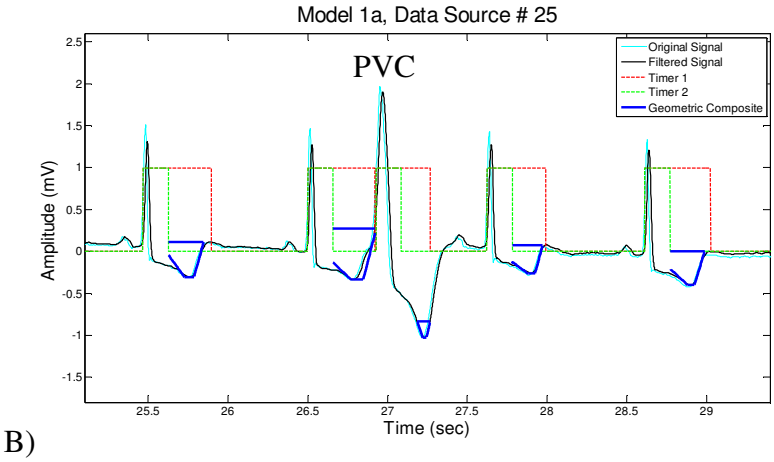

B)

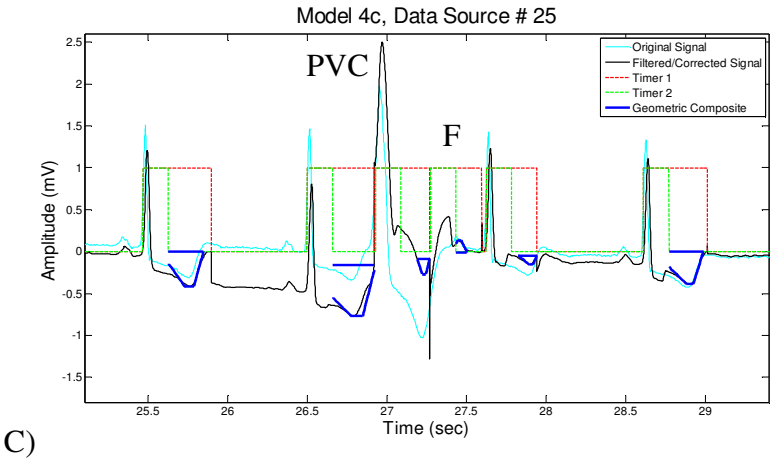

C)

Figure 4.5. Model comparison of recovery after PVC timer trigger. Inverted composites are *open* at start of T-wave window interval. Window edge used as composite edge for timing and area calculations. Note placement of composite T-wave baseline for each model. A) Composite T-wave after PVC was classified as non-inverted. C) Slew from baseline correction caused false timer trigger (F).

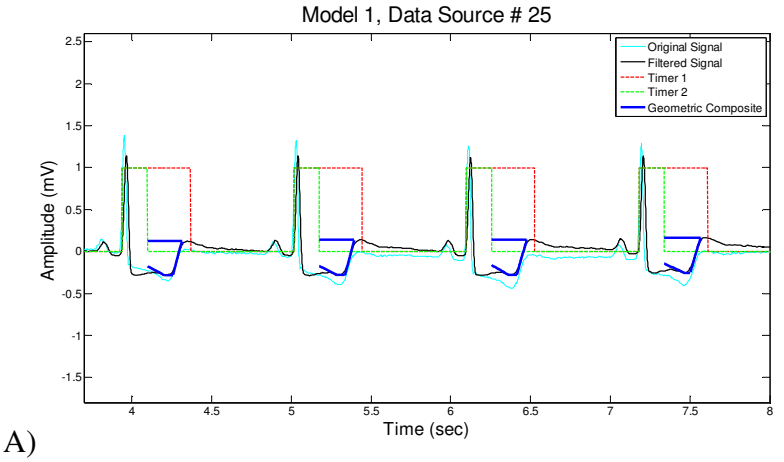

A)

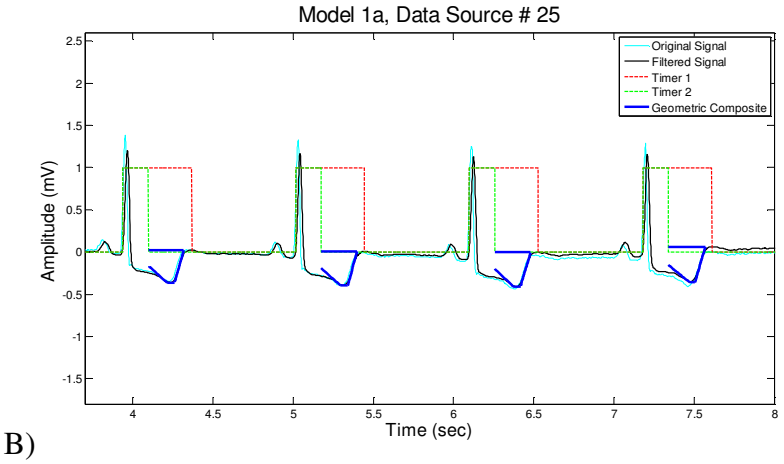

B)

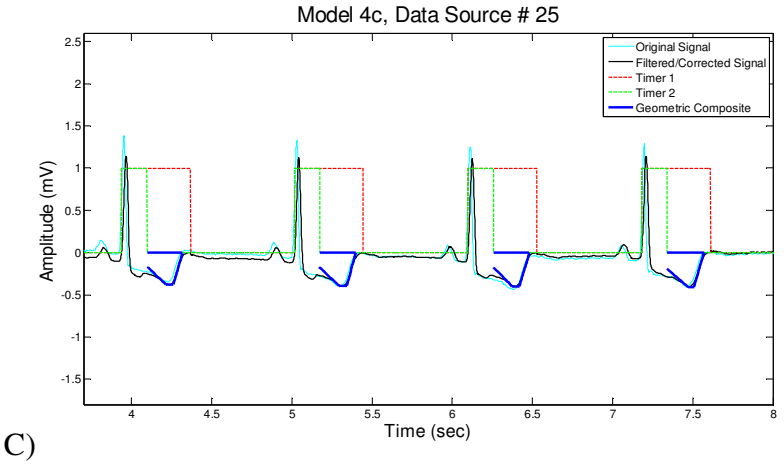

C)

Figure 4.6. Model comparison of inverted classification of T-waves in ECG signal with depressed ST segment because of long QT interval. Inverted composites are *open* at start of T-wave window interval. Window edge used as composite edge for timing and area calculations. Note placement of composite T-wave baseline for each model. A) Heightened T-wave caused by HPF distortion.

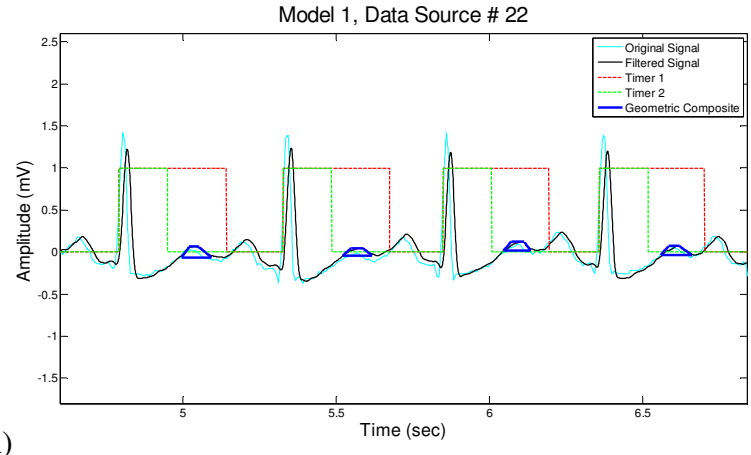

A)

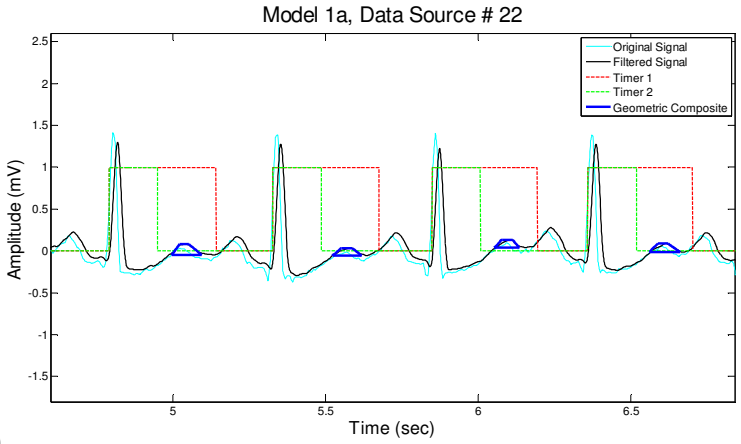

B)

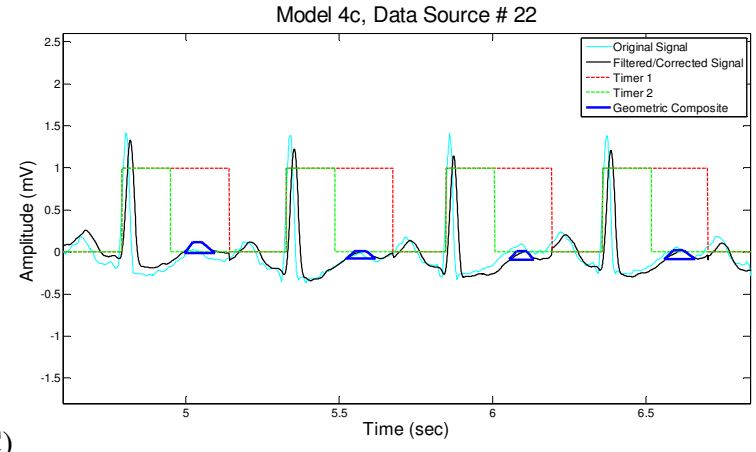

C)

Figure 4.7. Model comparison of non-inverted classification of T-waves in ECG signal with depressed ST segment. Note placement of composite T-wave baseline for each model. C) Very short TP interval causing non-zero baseline placement.

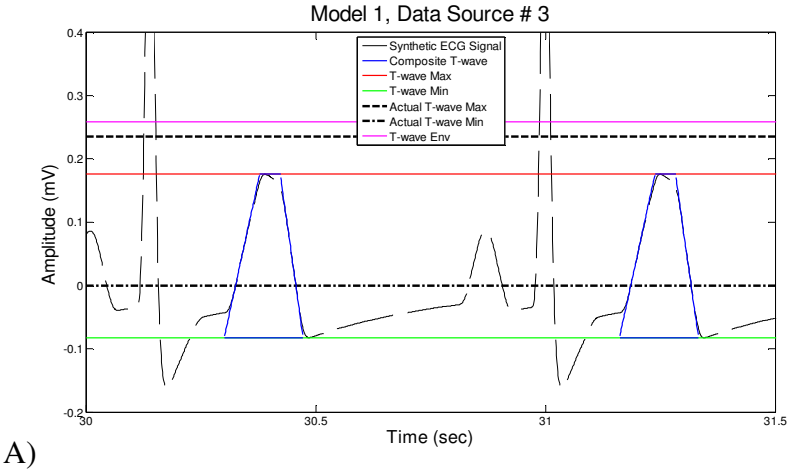

A)

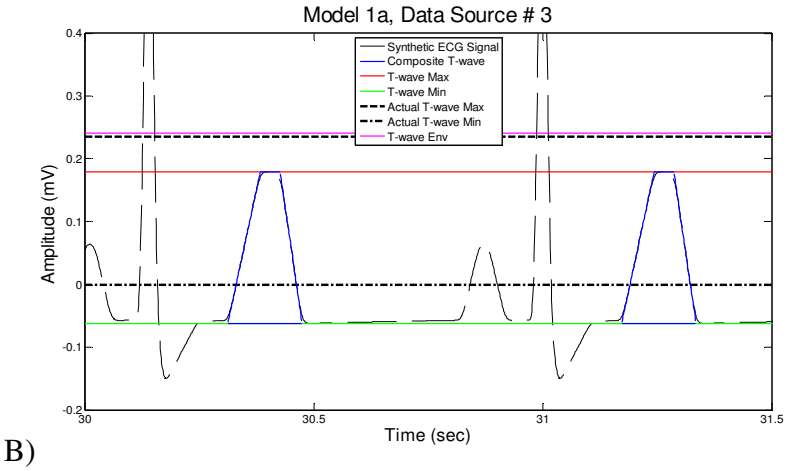

B)

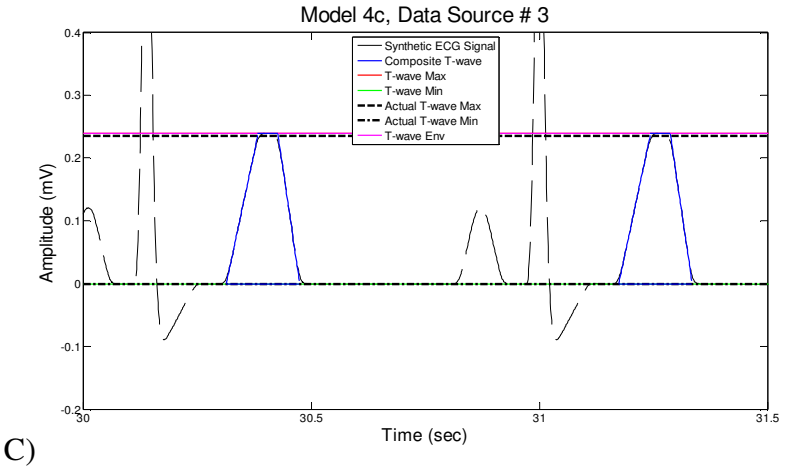

C)

Figure 4.8. Model comparison of non-inverted T-wave peak amplitudes and envelope heights. Note waveshape distortion and placement of composite T-wave baseline for each model and compare to Figure 4.9.

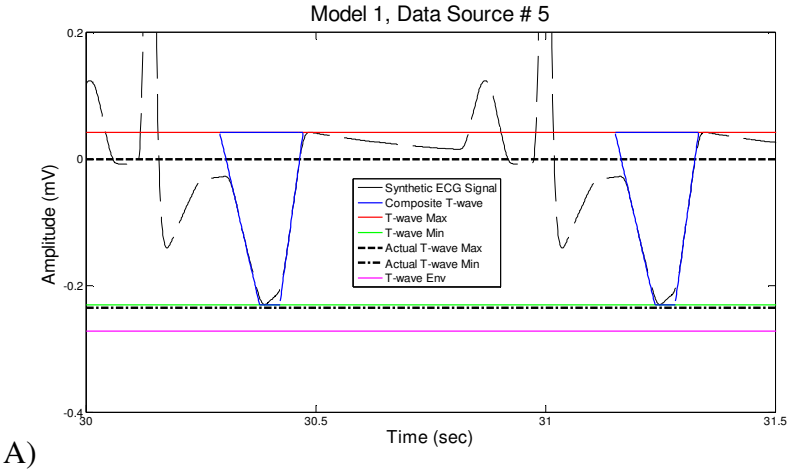

A)

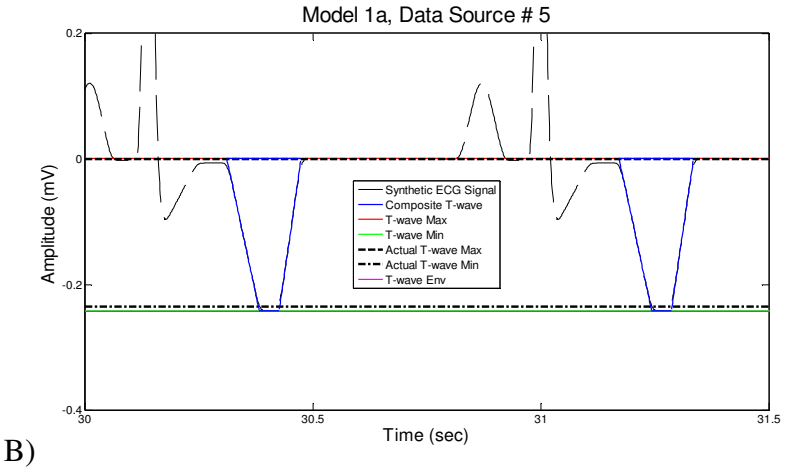

B)

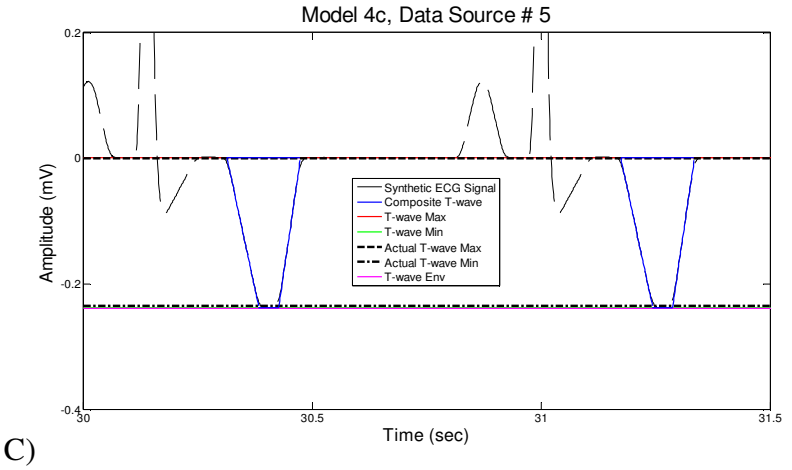

C)

Figure 4.9. Model comparison of inverted T-wave peak amplitudes and envelope heights. Note waveshape distortion and placement of composite T-wave baseline for each model and compare to Figure 4.8.

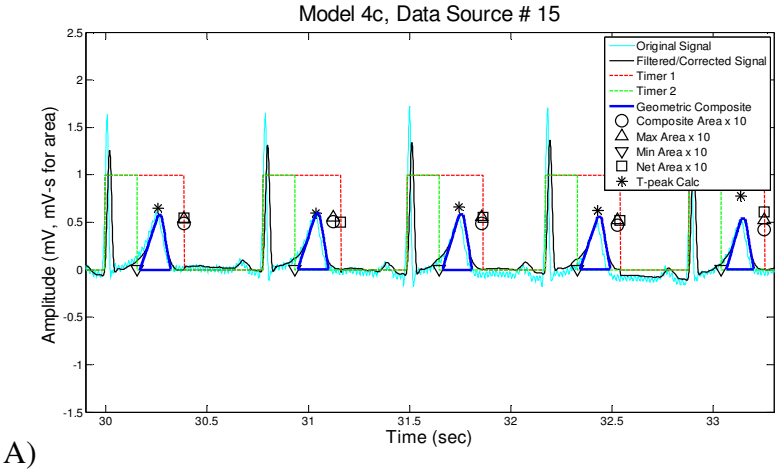

A)

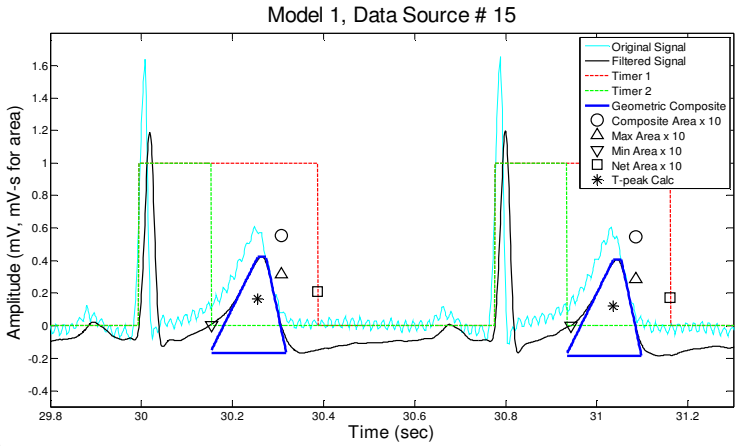

B)

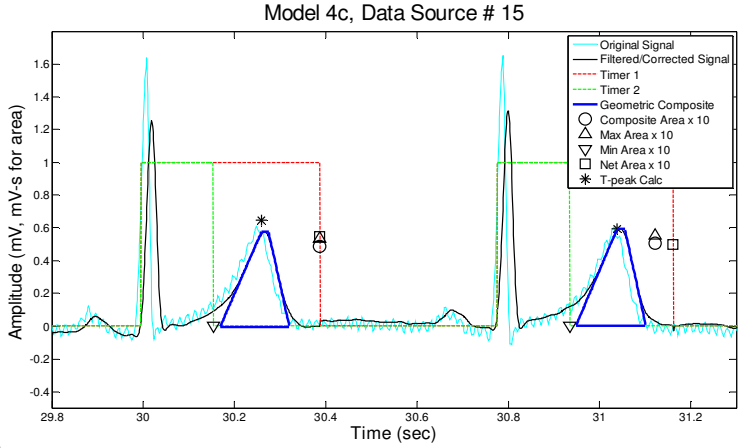

C)

Figure 4.10. Model comparison of T-wave composite figures for healthy patient. Generally, ideal data results are represented by tight clusters of area markers and T-peak Calc marker close to composite peak. A) Model 4c performance over several seconds. B) and C) Model comparison close-up to show differences in marker clusters, baseline placement, and waveshape distortion.

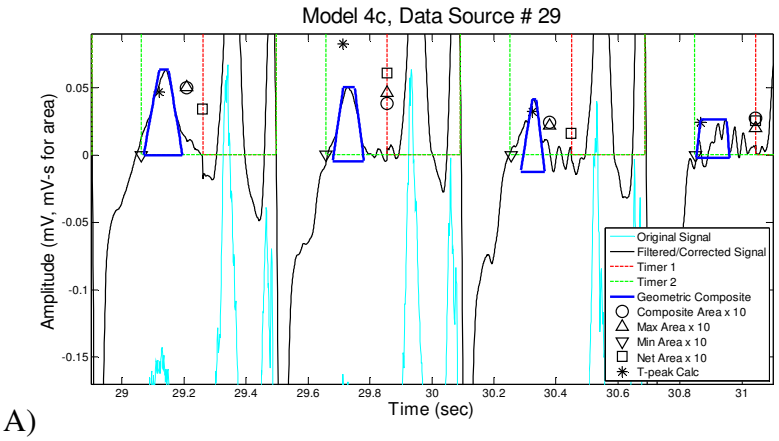

A)

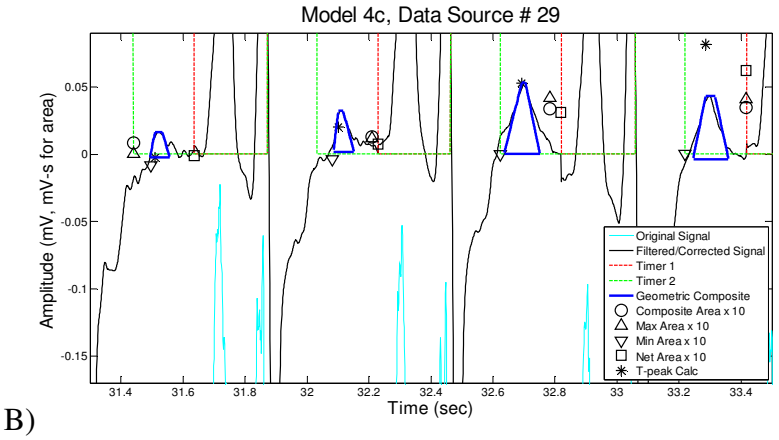

B)

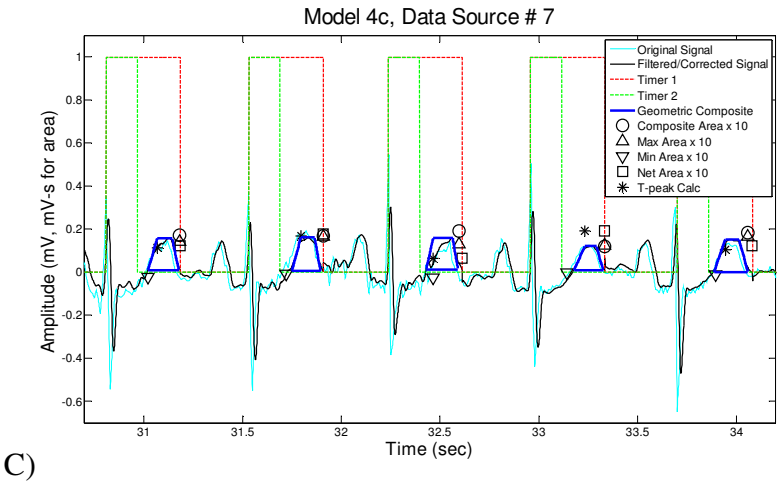

C)

Figure 4.11. A) and B) Four seconds of Model 4c composite T-wave figures as ECG signal changes from good to noisy and back to good. Note very small T-wave heights and inverted R-waves. C) Three seconds of Model 4c composite T-wave figures. Note very small R-waves and center composite approximation considered better than original due to temporary noise on signal.

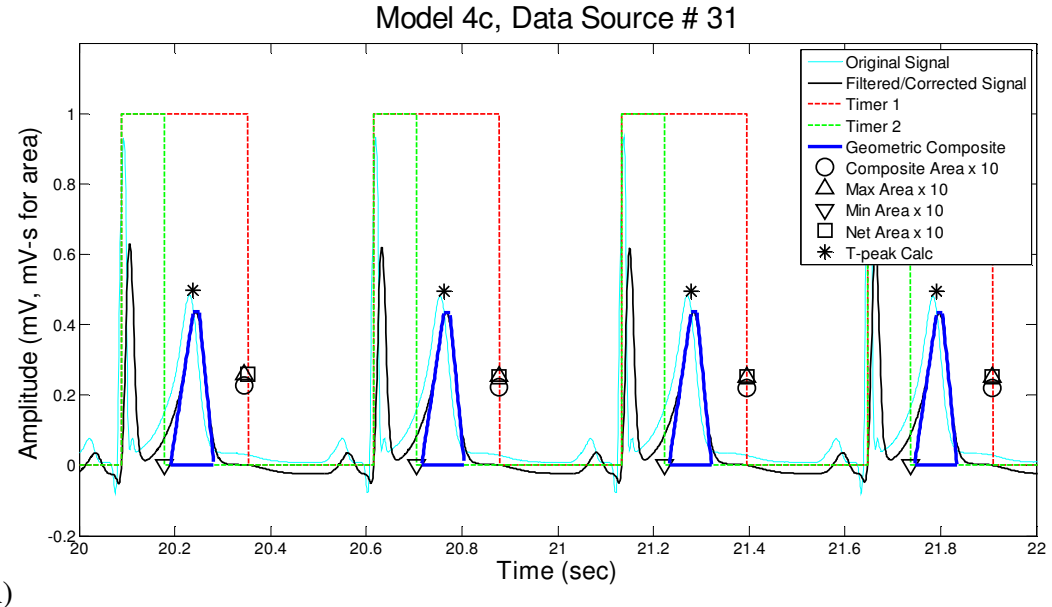

A)

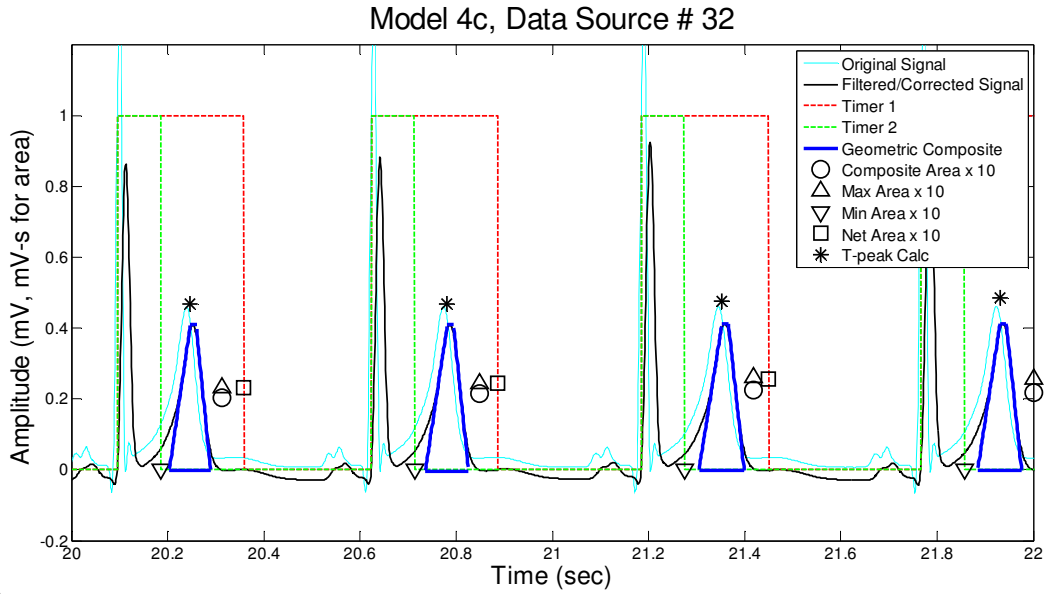

B)

Figure 4.12. Comparison of Model 4c composite figures for synthetic data source A) with MTWA and B) without MTWA.

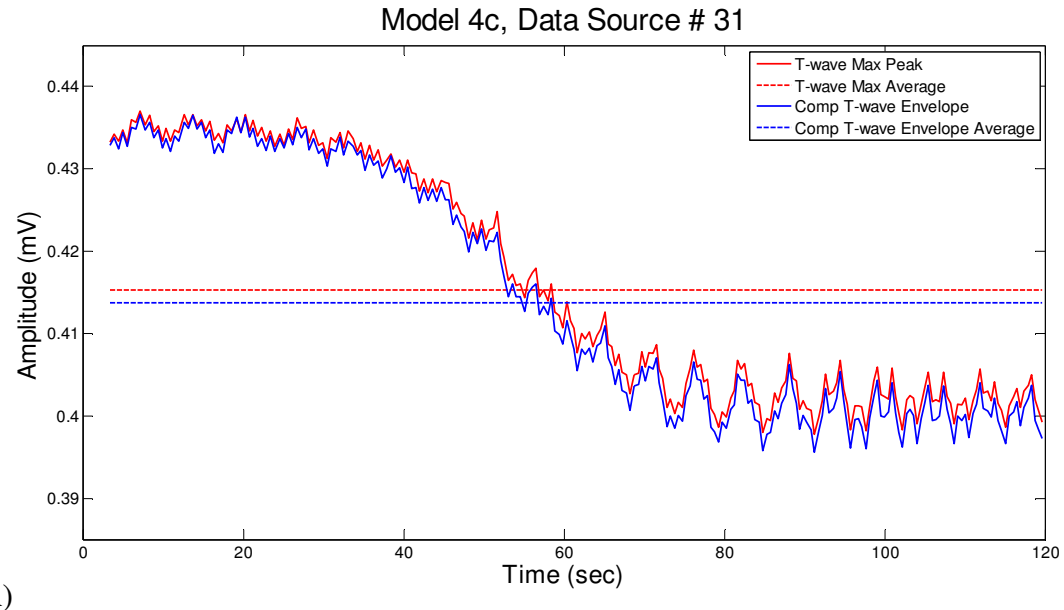

A)

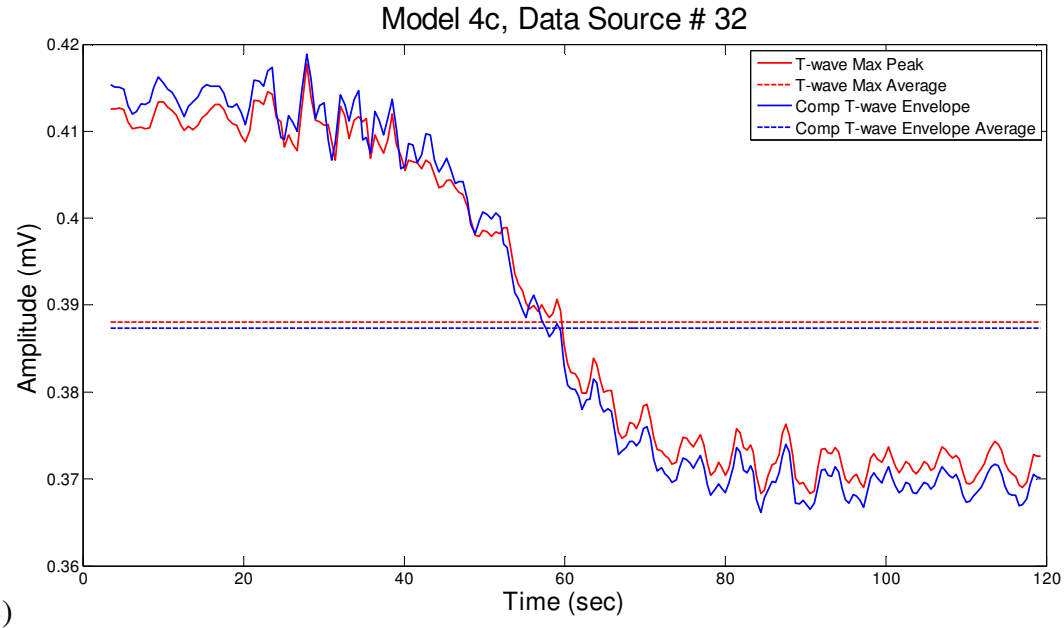

B)

Figure 4.13. Comparison of Model 4c T-wave maximum peak amplitudes and composite figure envelope heights for synthetic data source A) with MTWA and B) without MTWA. MTWA are seen most clearly in the first 45 sec of A). Note that peak amplitudes and composite envelope heights track closely in both A) and B).

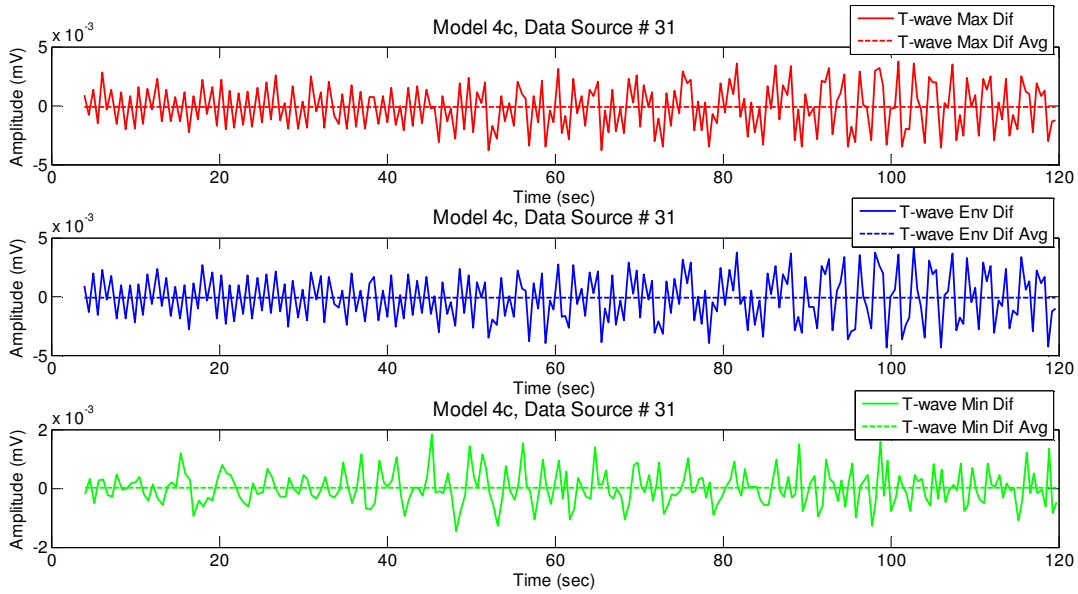

A)

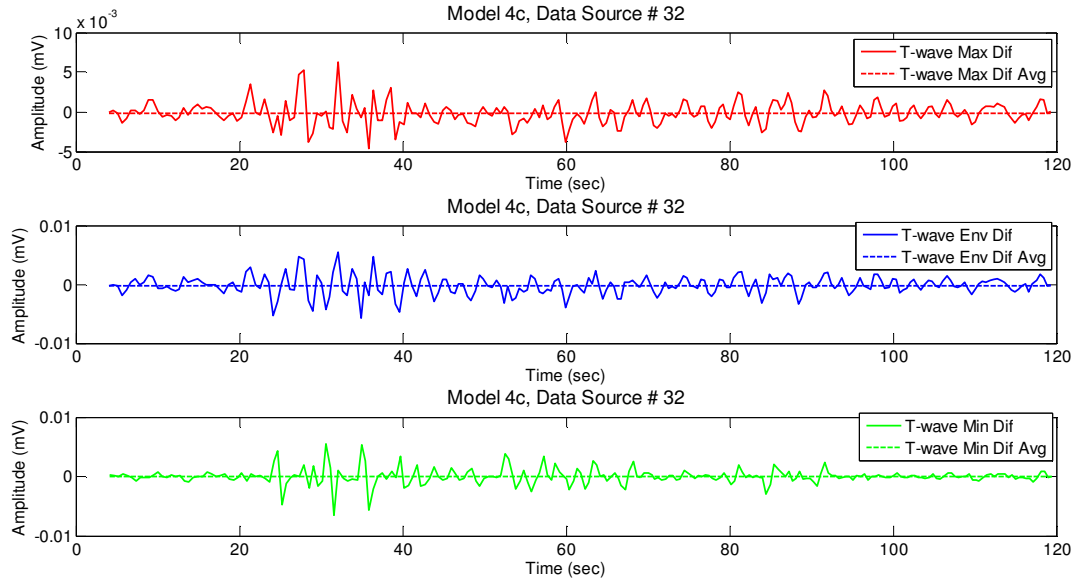

B)

Figure 4.14. Comparison of Model 4c beat-to-beat T-wave max/min peak amplitude and composite figure envelope height differences for synthetic data source A) with MTWA and B) without MTWA. MTWA are seen most clearly in the first 45 sec of the upper two graphs of A). Note that maximum peak amplitude and composite envelope height differences track closely in both A) and B).

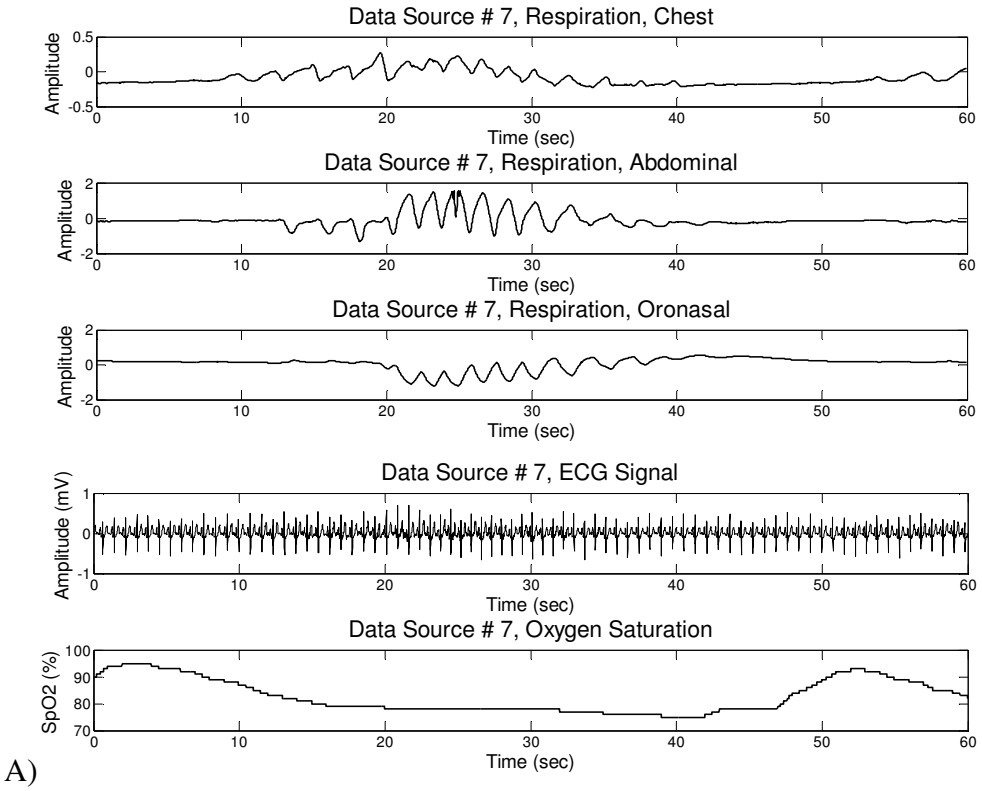

A)

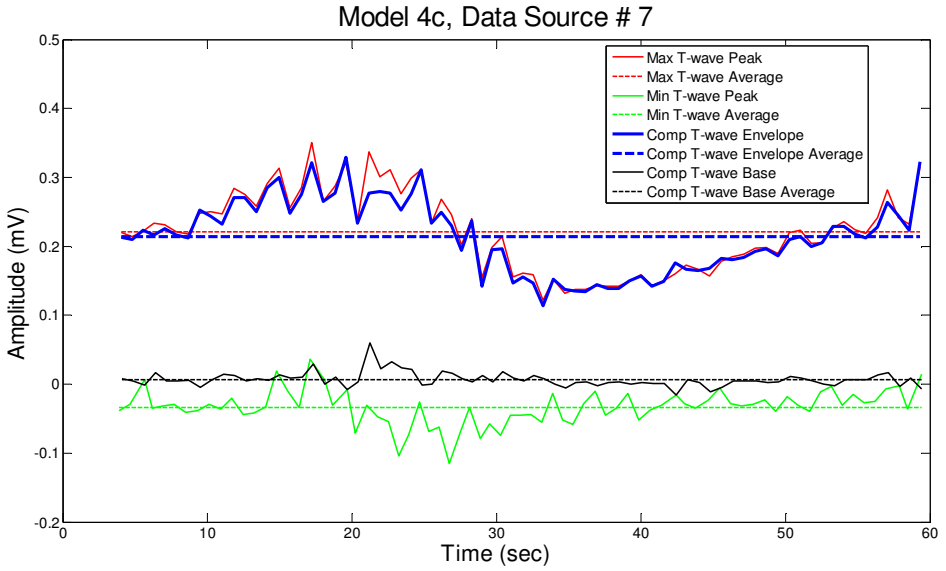

B)

Figure 4.15. A) Respiration, ECG signal, and oxygen saturation level (SpO2) for sleep apnea patient of data source # 7. B) Comparison of Model 4c T-wave max/min peak amplitude and composite figure envelope heights on same time scale as graphs of A). Note that maximum peak amplitudes and composite envelope heights track closely and are correlated (but not in phase) with oxygen levels in A).

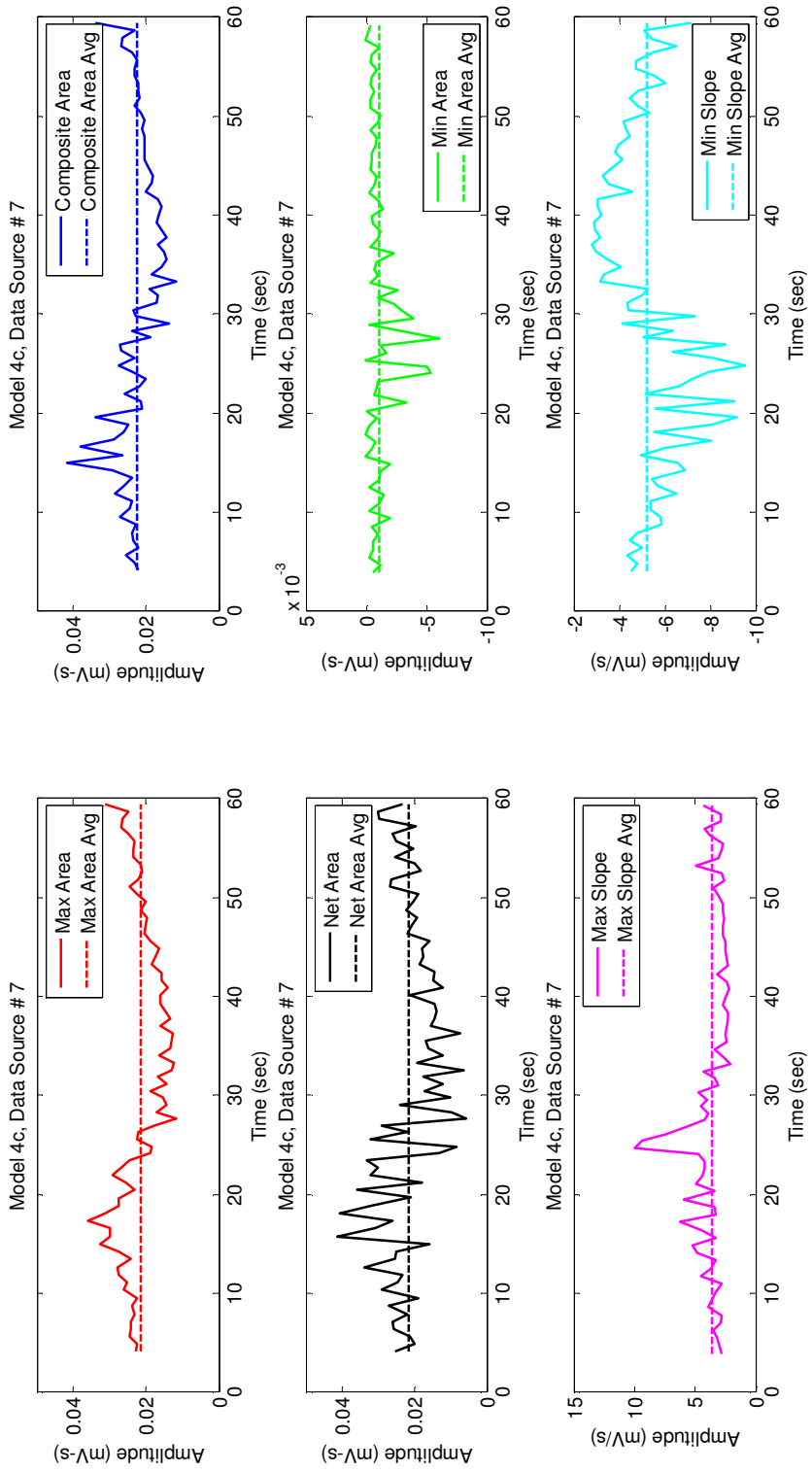

Figure 4.16. Model 4c T-wave area and slope magnitudes for sleep apnea patient of data source # 7. Positive area measures (max, composite, and net) and min slope show correlation with SpO2 levels and height measures of Figure 4.15.

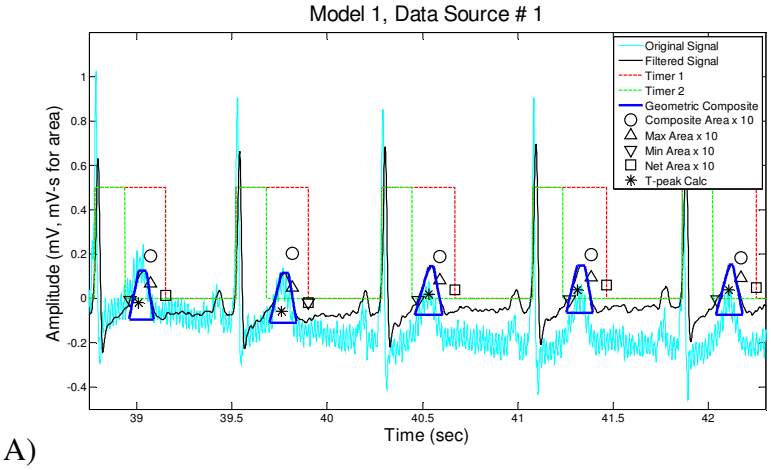

A)

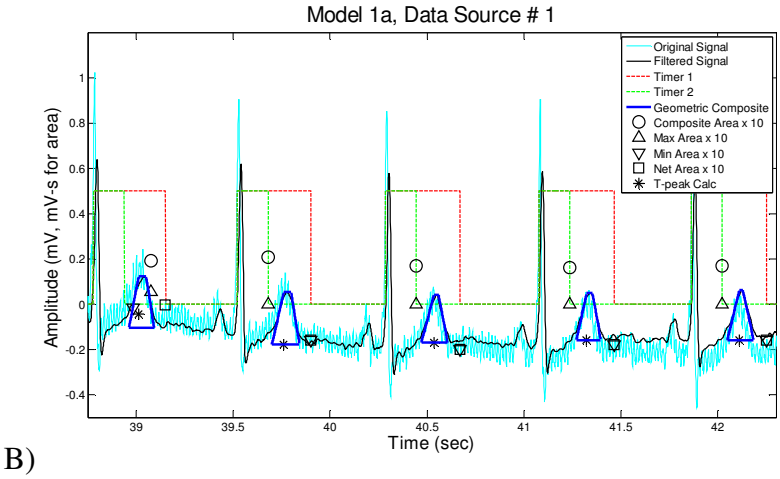

B)

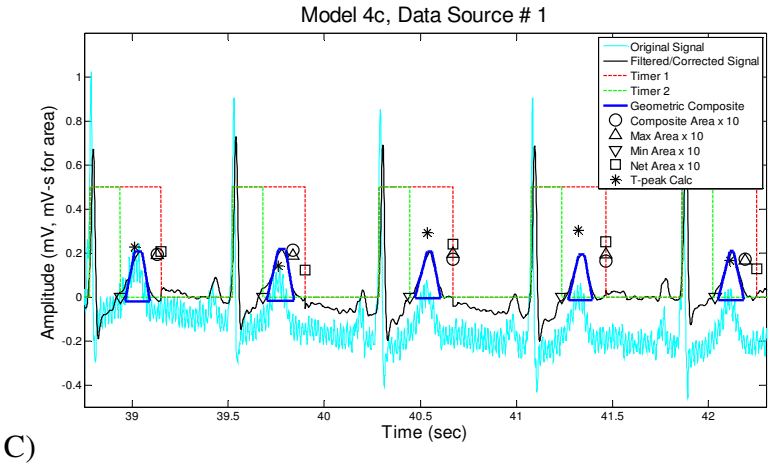

C)

Figure 4.17. Model comparison of ECG signal (data source # 1) with moderate baseline drift and 60 Hz noise. Note waveshape distortion, marker clusters, and placement of composite T-wave baseline for each model.

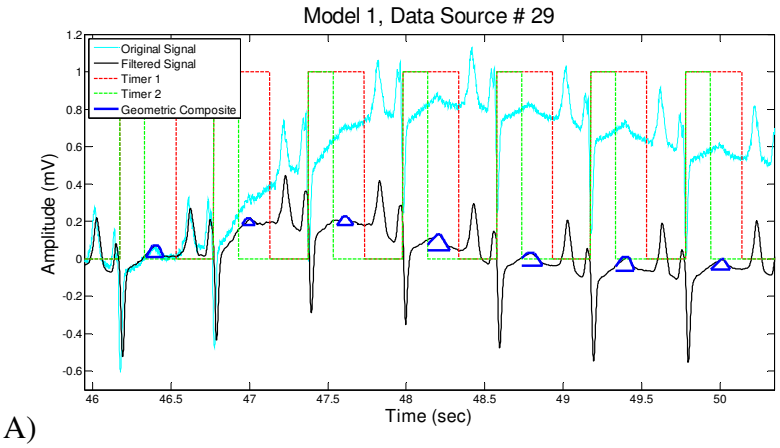

A)

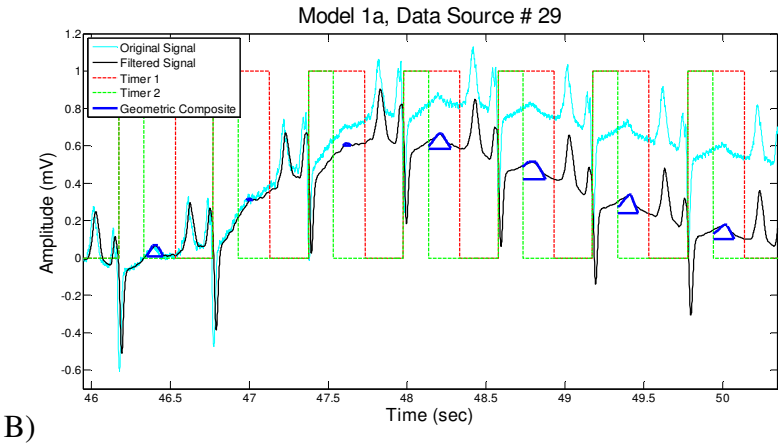

B)

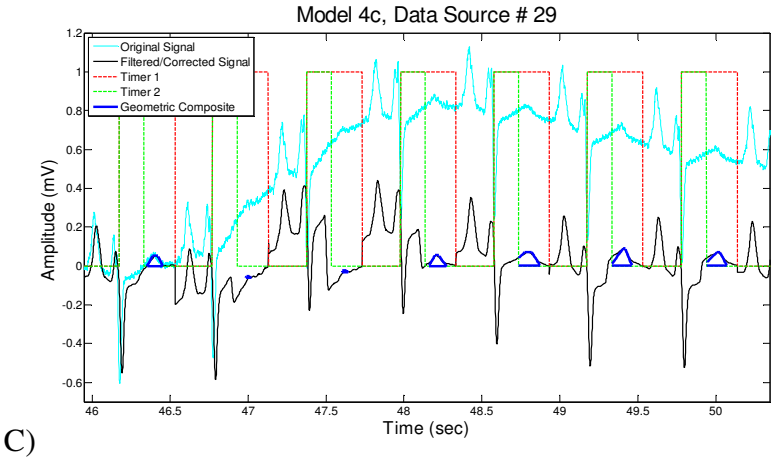

C)

Figure 4.18. Model comparison of ECG signal (data source # 29) with large amounts of baseline drift. Note inverted R-waves, waveshape distortion, and placement of composite T-wave baseline for each model.

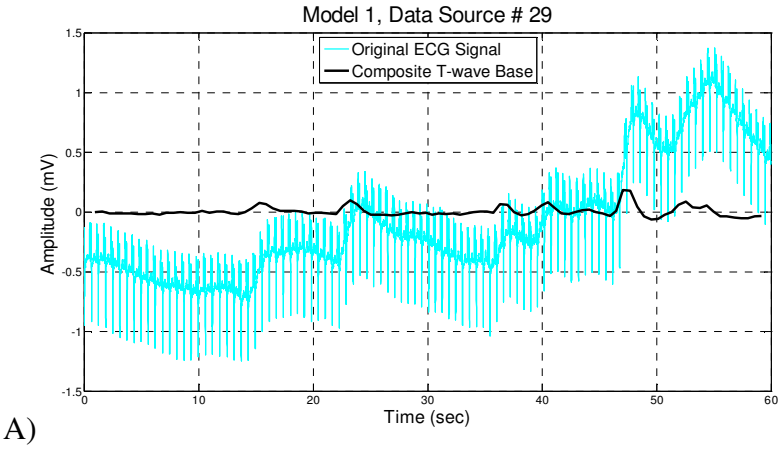

A)

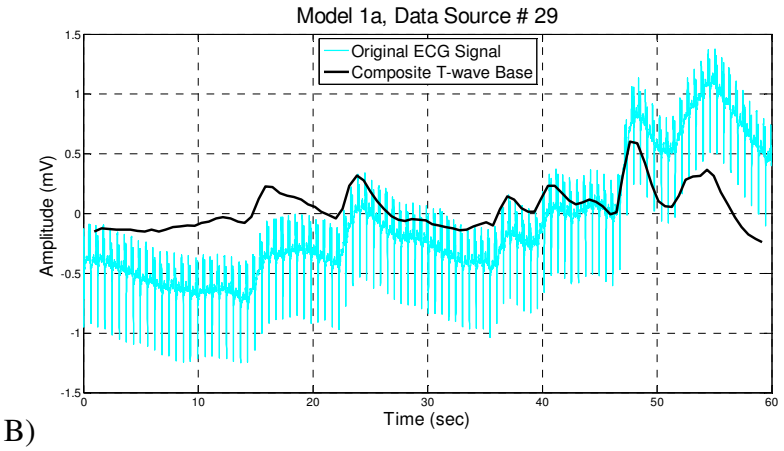

B)

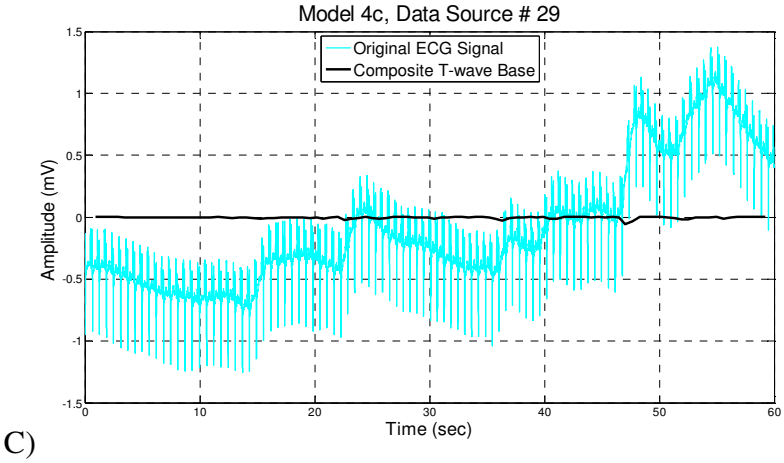

C)

Figure 4.19. Model comparison of composite baseline placement for ECG signal (data source # 29) with large amounts of baseline drift.

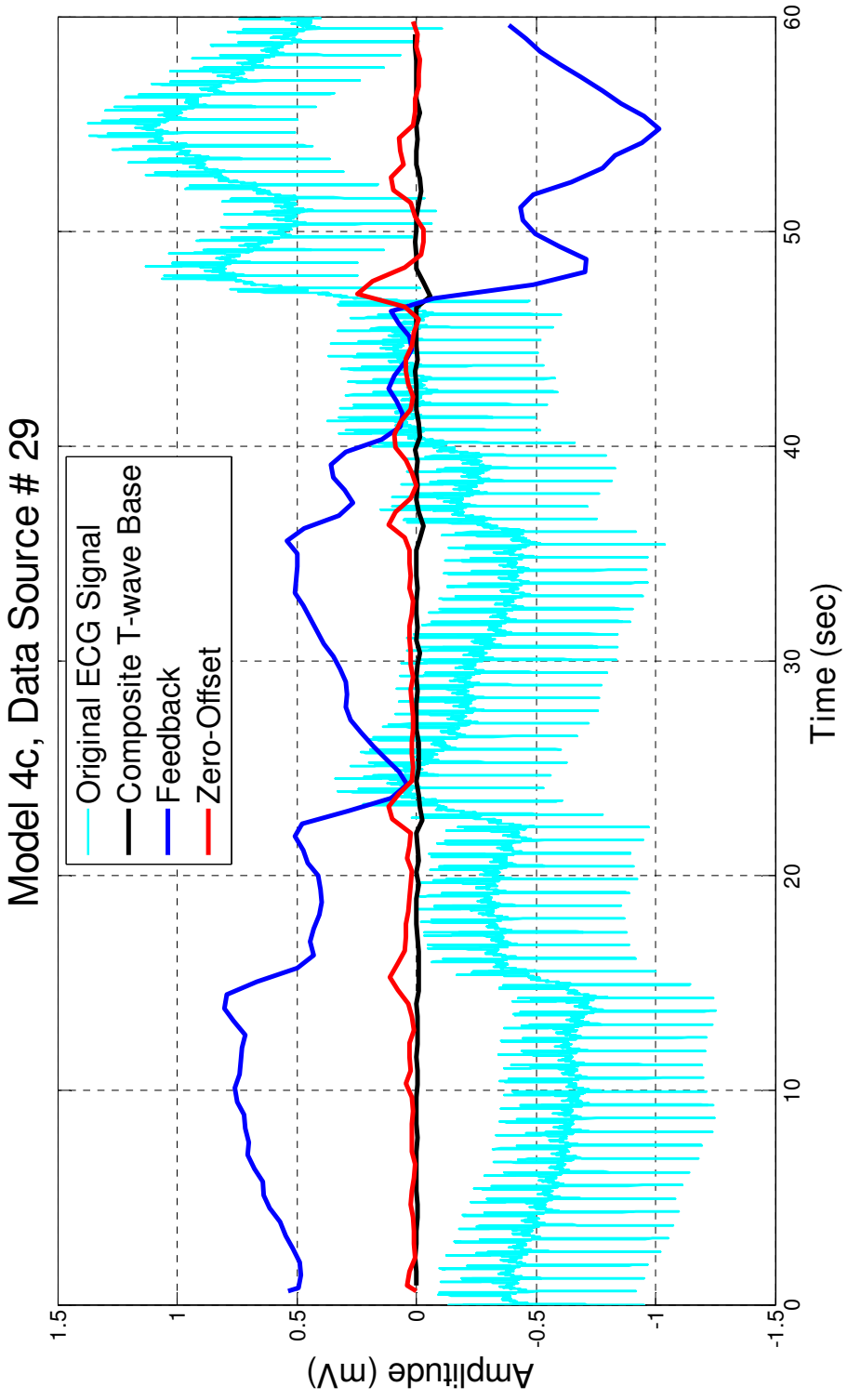

Figure 4.20. Feedback and Zero-Offset signals of Model 4c. Note near mirror image relationship between ECG signal baseline and Feedback signal. Also note the near-zero composite baseline placement throughout.

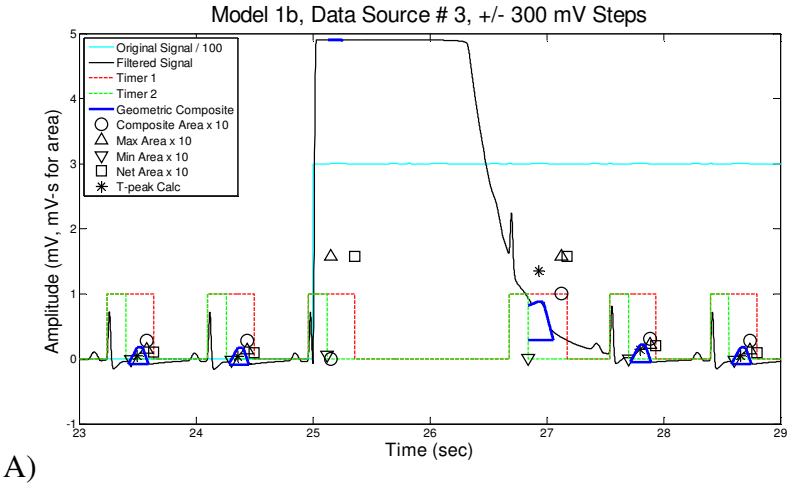

A)

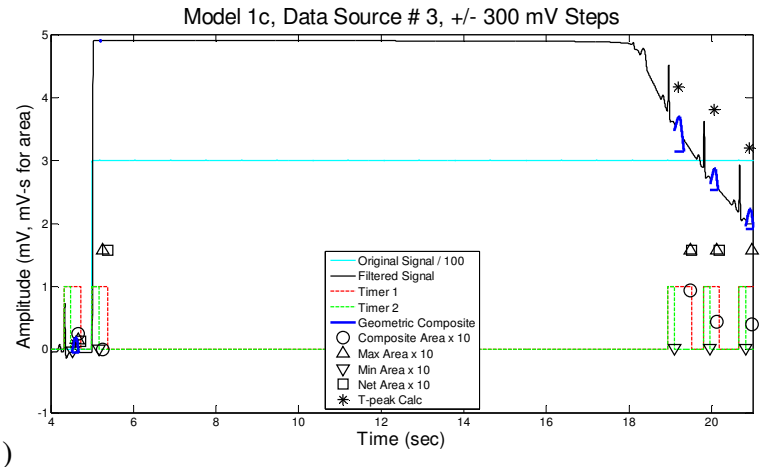

B)

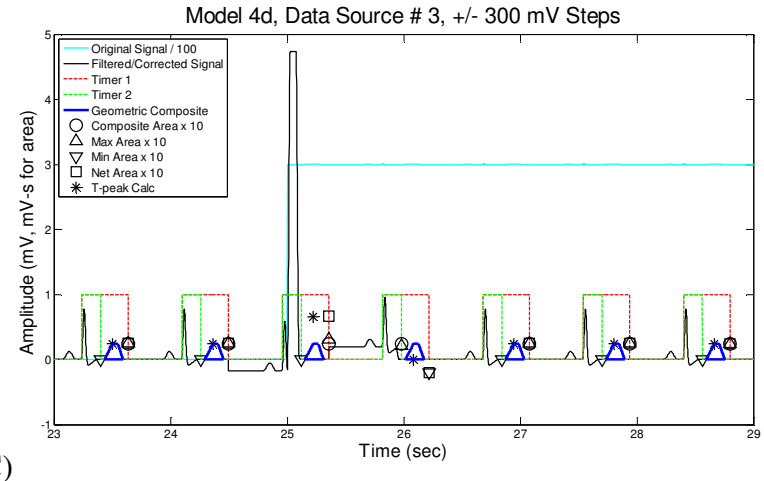

C)

Figure 4.21. Model comparison for transient response to +300 mV step pulse. A) and C) share the same time scale. B) Time course recovery continued in Figure 4.22B. C) Note T-wave recovery in less than one heartbeat. Note waveshape distortion, marker clusters, and placement of composite T-wave baseline for each model.

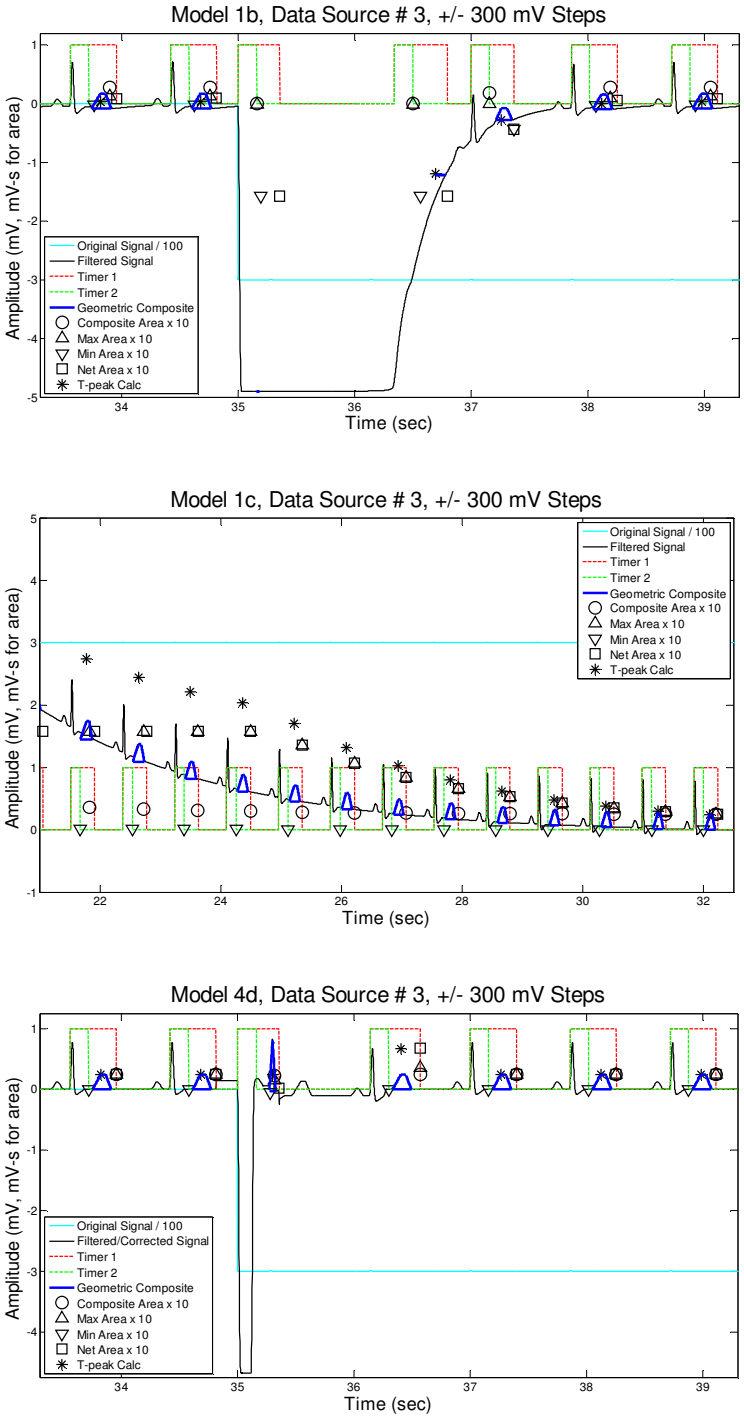

Figure 4.22. A) and C) Model comparison for transient response to -300 mV step pulse. A) and C) share the same time scale. B) Continuation of Model 1c step recovery from Figure 4.21B. Note waveshape distortion, marker clusters, and placement of composite T-wave baseline for each model.

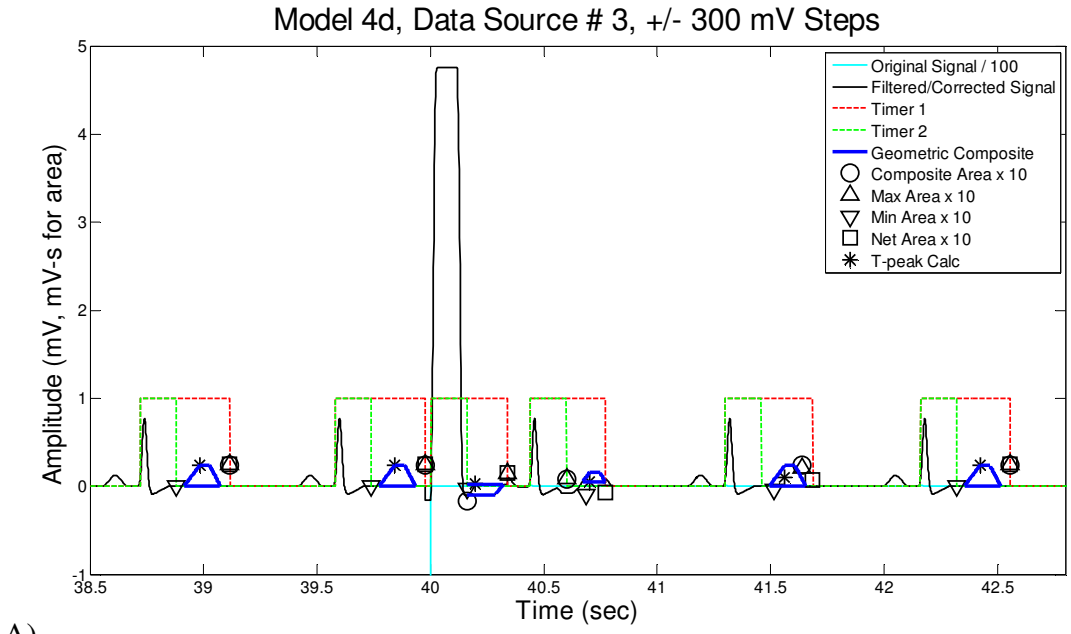

A)

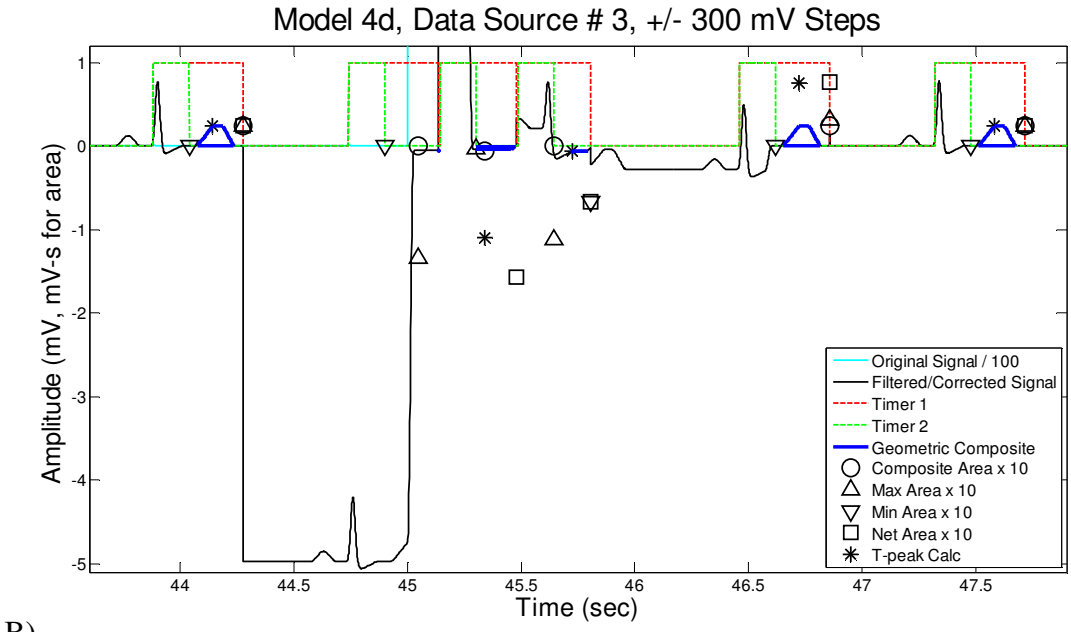

B)

Figure 4.23. Model 4d examples of false trigger events caused by recovery transients.

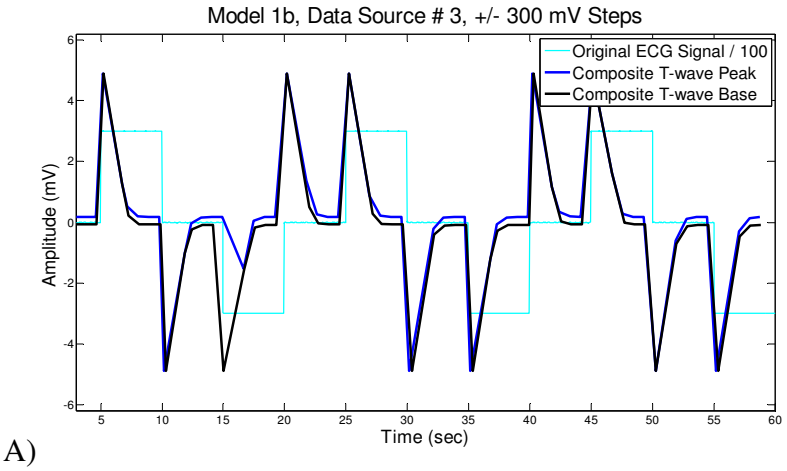

A)

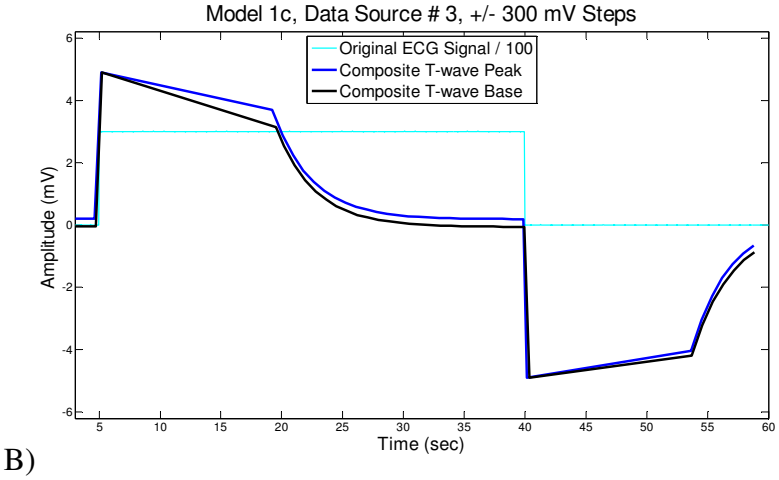

B)

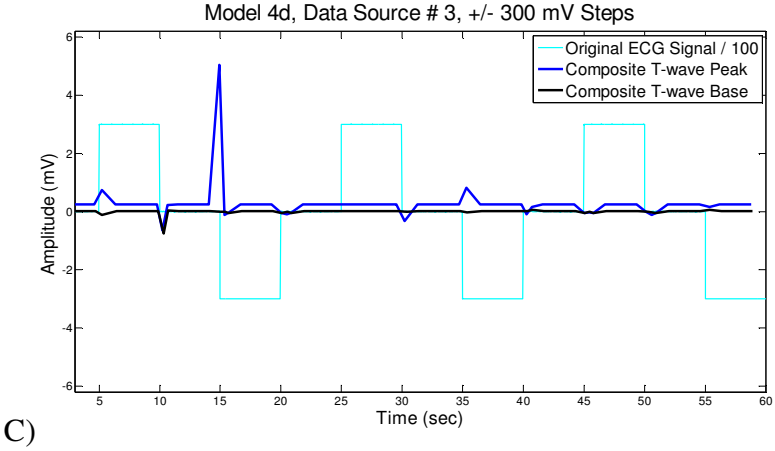

C)

Figure 4.24. Model comparison of composite T-wave peak and baseline placement in response to ±300 mV step pulse inputs.

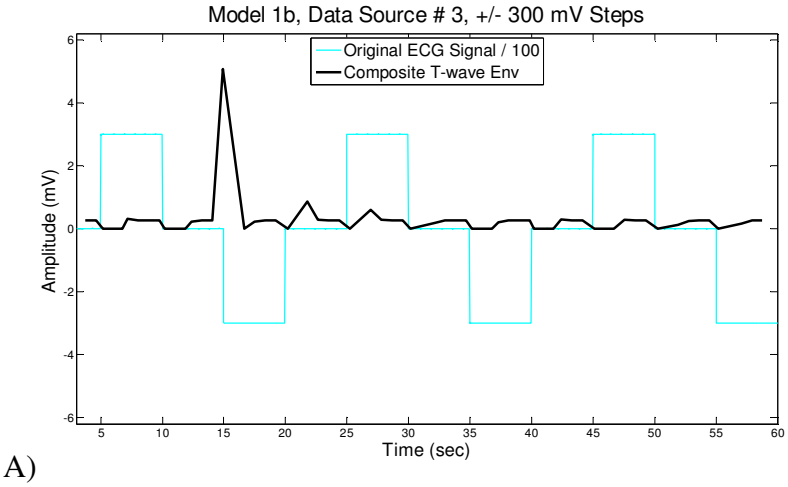

A)

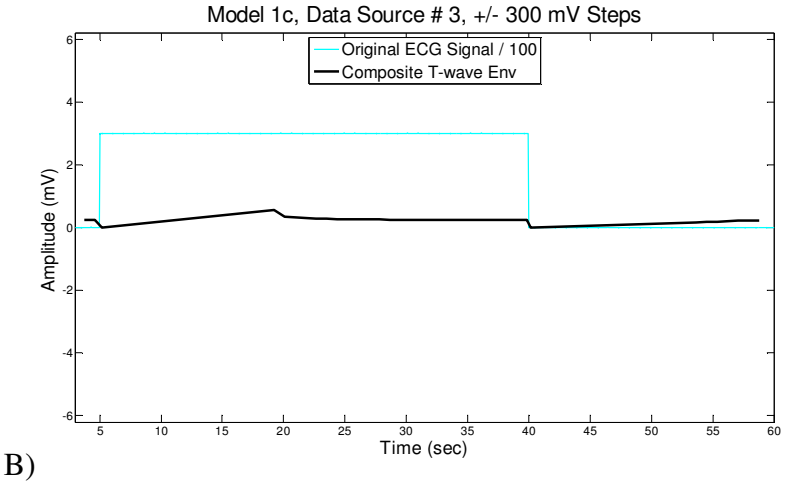

B)

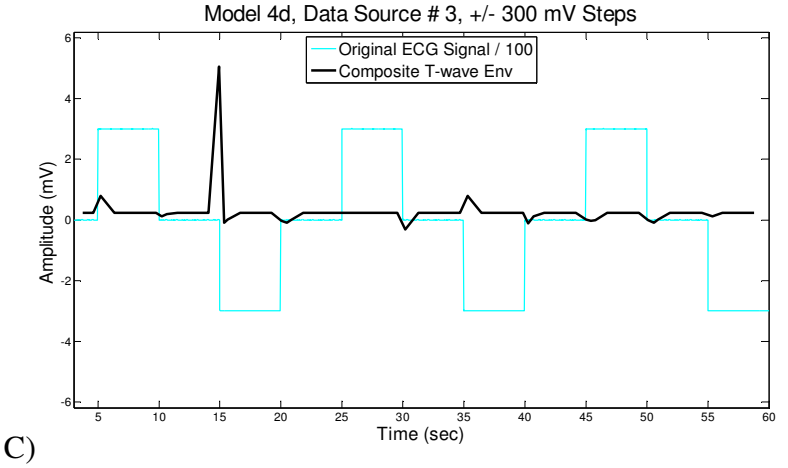

C)

Figure 4.25. Model comparison of composite T-wave envelope height in response to ±300 mV step pulse inputs.

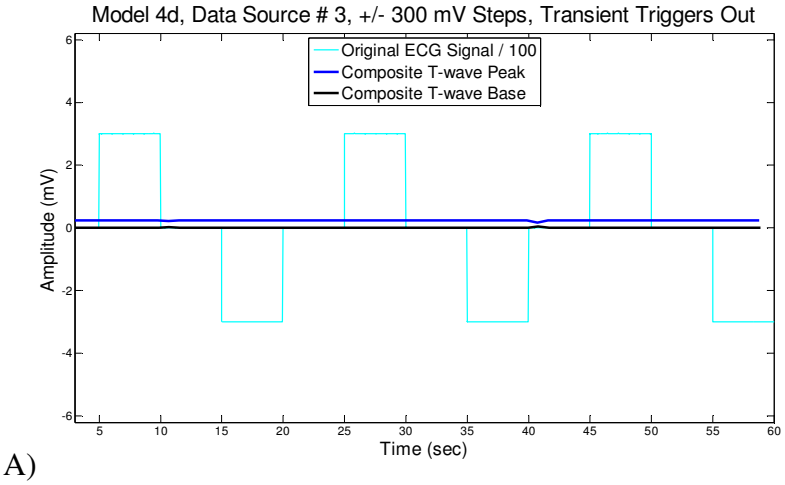

A)

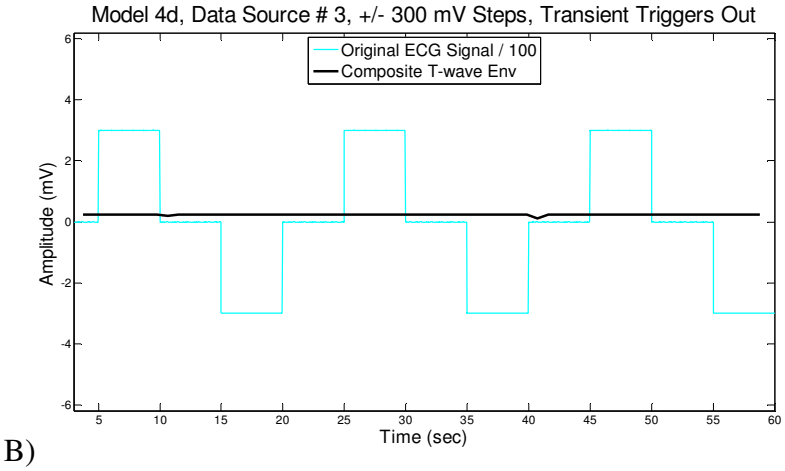

B)

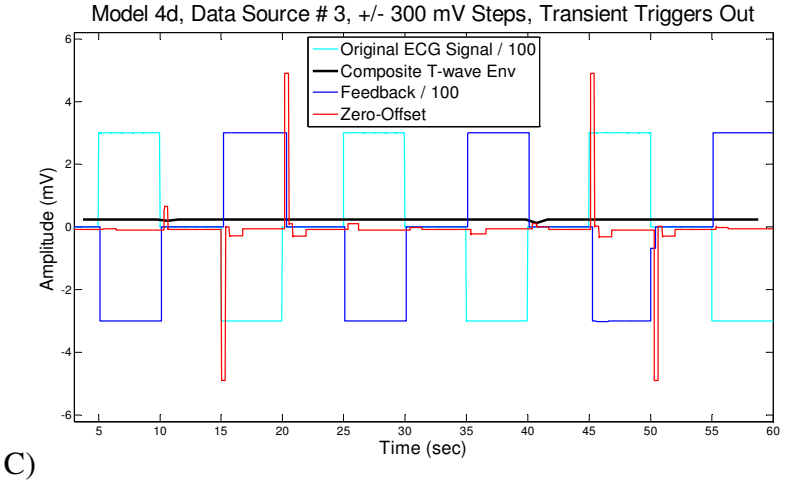

C)

Figure 4.26. Model 4d responding to ±300 mV step pulse inputs with transient triggers ignored. A) Composite T-wave peak and baseline placement. B) Composite T-wave envelope height. C) Nearly flat composite T-wave envelope height shown with underlying Feedback and Zero-Offset baseline correction signals.

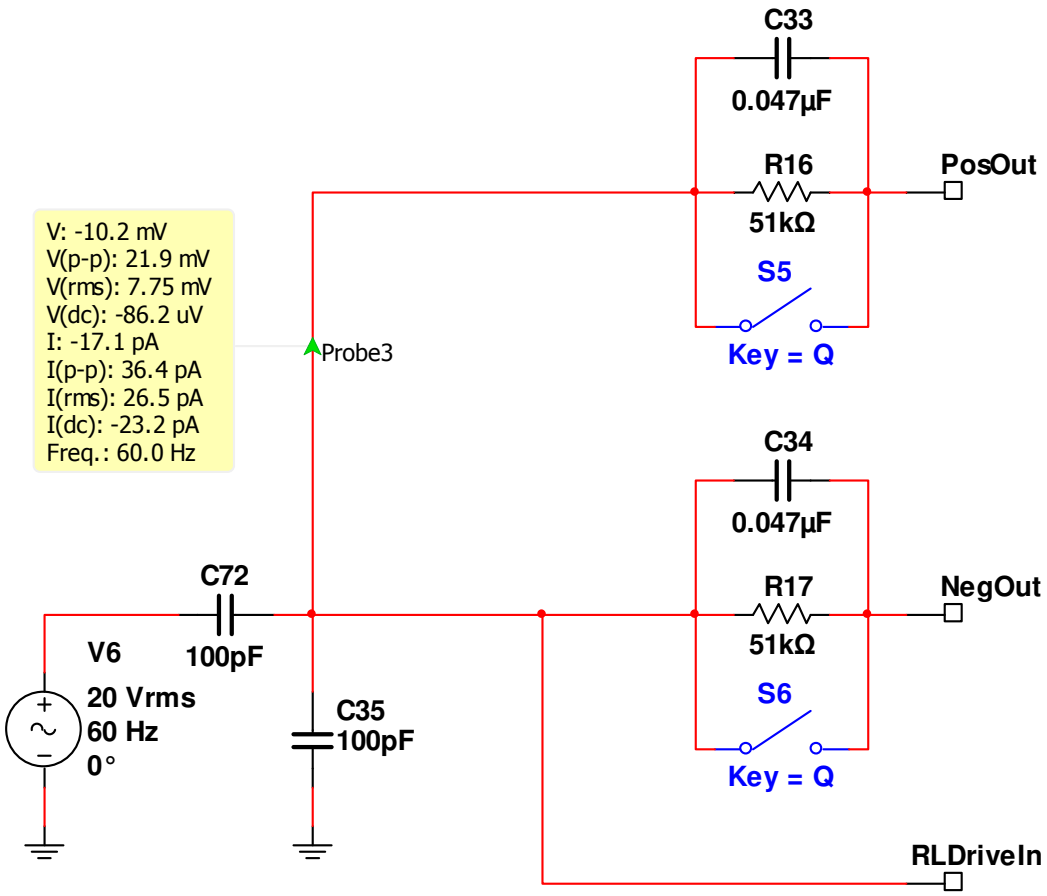

Figure 4.27. Model 4d CMR test showing RLD reduction of 10 Vrms CMV source to 7.75 mVrms (-62.2 dB).

CHAPTER 5

5. DISCUSSION

In Chapter 1, the T-wave was described as a sensitive but non-specific indicator of cardiovascular health. T-waves were shown to be classified descriptively into a small group of morphologies (Figure 1.2), but the characteristic features of even those few waveshapes were poorly quantified in the reference materials examined. Changes in T-wave height and duration were associated with a variety of pathologic and non-pathologic causes, but because specificity was shown to be weak, diagnosis from T-wave observation was described as problematic.

The Model 4c (4d) T-wave monitor as presented herein addresses the issue of T-wave specificity by extracting beat-to-beat quantitative data for T-wave height, leading and trailing edge slopes, and area measures. While not explored here, it is hoped that future analysis will be able to correlate at least some of the extracted T-wave metrics with clinical diagnosis. Further, the T-wave monitor output is highly compressed, providing opportunity to expand the time-course evaluation of progressive changes in T-wave morphology, while using much smaller amounts of data storage. Data compression also potentially reduces system power loading and transmission bandwidth requirements.

Chapter 1 also detailed some of the challenges encountered when trying to record ECG signals at qualities high enough to extract T-wave features accurately. Noise from sources inside and outside the body was described as capable of generating signal magnitudes that can easily overwhelm the electrical activity signals of the heart. Low-pass filtering was stated as an effective means to reduce noise above the T-wave bandwidth, but because of the T-wave's inherent low frequency content, even moderate

high-pass filtering was shown to distort the waveshape of interest (Chapter 3 and Chapter 4). Other methods to remove the low frequency noise of baseline drift, such as the use of curve-fitting spline functions, for example, require an amount of signal history and might not react quickly to transient events.

The lack of high-pass filtering in the Model 4c (4d) T-wave monitor signal path eliminates the HPF T-wave distortion and leaves other very low frequency content – such as respiration and heart rate variability – unaltered. In place of continuous high-pass filtering, the Feedback and Zero-Offset step-change correction functions work to restore the ECG signal isoelectric line to near zero every timer cycle. Recovery from large motion artifact transients is expected to occur within one or two timer cycles, but recovery can complete in less than one heartbeat, as was demonstrated in Figure 4.21C. The reduction of signal saturation found in the transient response test results of Chapter 4 is another benefit of the step-change correction functions.

Unfortunately, high-speed transient recoveries sporadically caused additional non-R-wave timer cycle delays and introduced erroneous T-wave data related to the false trigger events (Figure 4.23). Ignoring the transient trigger T-wave data by magnitude thresholding, however, proved highly successful as tested (Table 4.3). Even with the false trigger events included, though, the percentage of R-wave triggered timer events averaged over 98% for the 2,604 heartbeats tested per model.

Accuracy of the extracted T-wave feature data was provided for a smaller set of 260 heartbeats in Table 4.2. Four data source files of synthetic ECG signals with known T-wave morphologic parameters (Table 3.3) were simulated. T-wave feature errors for Model 4c averaged less than 3%, with most feature data having a less than 2% error. T-

wave monitor models with high-pass filtering generally delivered weaker performance results, especially with regard to T-wave height and area measurements. The worst of these was Model 1's average positive area error of over -58%, owed to larger amounts of HPF waveform distortion and baseline offset.

With correct T-wave state of inversion classification averaging over 99%, the extracted T-wave feature data were combined to form either of the geometric composite T-wave approximations shown in Figure 1.4. Using a *greater than two-thirds* rule as the standard for goodness of fit success, observations of each the almost 2,600 T-waves attempted per model concluded that more than 88% of the geometric figures of Model 4c reasonably approximated the beat-to-beat T-wave morphology. Around 4% of the geometric figures found to be reasonable approximations were also considered better than the ECG waveshape at reflecting the underlying T-wave morphology.

Meaningfulness of the geometric composite T-wave approximations was determined by assessing whether or not clinically relevant information was passed from the ECG signal waveform to the composite figure, or was evident in the figure's constituent data. It was logically argued that if the composite figure were a reasonable approximation of the T-wave in the ECG signal, then the state of cardiovascular health conveyed by observation of one would be conveyed by observation of the other. Meaningfulness of the extracted constituent data was demonstrated in Chapter 4 by showing that MTWA and the effects of oxygen saturation levels (respiration) on T-wave morphology were observable using the extracted T-wave feature data. In addition, the composite T-wave envelope height data was shown to compare well with measured T-wave peak heights, in these cases.

The results in Table 4.2 and elsewhere show that the use of T-wave envelope height instead of peak height eliminates some baseline drift induced error from extracted height and area T-wave feature metrics. It was also found that baseline placement near zero was improved by a factor of about 5, on average, by the Feedback and Zero-Offset step-change correction functions of Model 4c (4d). The results favor Model 4c (4d) by much larger degrees when comparing the three model performances under the extreme baseline drift or input step-pulse conditions of Figure 4.19, Figure 4.24, and Figure 4.26. Here, the consistency of near-zero baseline placement and the speed of transient response recovery for Model 4c (4d) were un-approached by the other two models tested.

The non-inverted geometric composite T-wave approximation results of Table 4.4 provide averaged T-wave feature data for over 1,600 heartbeats, across twenty-two ECG data source files. The T-wave height, slope, and area metrics should prove useful for those interested in T-wave morphologic characterization and for future T-wave monitor development. For example, it is remarkable to note how closely the average T-wave area and R-to-T timing of Table 4.4 matches the synthetic ECG parameters of data source # 3 in Table 3.3. Synthetic T-wave height and slope values would need to be increased to match the sample population more closely, however. The large standard deviations of Table 4.4 make it clear that there is a wide range of T-wave morphologies and timings to consider when arrhythmic data sources are included in the study.

As a consequence, and as was evidenced by the need to modify the timer intervals for several data source files (Table 4.1), improvements can be made to the T-wave monitor design to make it more accepting of arrhythmic ECG signals. For example, the heart rate dependency of Timer 1 could be adjusted to include more of the data markers

of Figure 1.7 as well as operate at the extremes required by the ECG signals of Table 4.1. Timer 2 and possibly Timer 3 require modifications to achieve similar goals.

The interval of Timer 5 could be lengthened, extending the Schmitt trigger disable period to prevent transient recovery trigger events. Alternatively, recovery speeds of the S&H, LPF, and differentiator circuits could be increased. Because non-R-wave triggers also occur from external sources (motion artifacts), however, the thresholding method used here or some other method is needed to ignore false T-wave data.

The present 40 Hz LPF and 60 Hz notch filter combine to create R-wave peak height errors of around -30%. Since the R-wave was not the primary focus of the design, this was not considered significant. However, future T-wave monitor designs could increase the LPF cutoff frequency and the Q of the 60 Hz notch filter to boost the high frequency cutoff to 150 Hz – the diagnostic ECG minimum (Diagnostic 2007).

Future designs could be improved by adding digital control to some of the T-wave monitor functions. For example, heart rate and arrhythmic sensing could be used to generate digital timer intervals. Sample and hold functions could be handled by ADC/DAC devices. Mathematical differentiation and integration functions could be programmed into the microcontroller as part of the signal-processing algorithm. Adding digital control, however, might trade energy efficiency for enhanced versatility.

Whether operated with analog or digital control, it is assured that extracted T-wave feature data will enable beat-to-beat morphologic characterizations that are more descriptive. It is anticipated that greater descriptiveness will add to clinical meaning.

References

ADG441/ADG442/ADG444: LC^{2}MOS quad SPST switches. Analog Devices. Datasheet, C00396-0-5/05(A), rev. A. 2005.

Allen J, Anderson JMcC, Dempsey GJ, Adgey AAJ. Efficient baseline wander removal for feature analysis of electrocardiographic body surface maps. *Int Conf IEEE EMBS*. 1994;2:1316-7.

Baker RJ. CMOS: Circuit design, layout, and simulation. Hoboken, New Jersey: Wiley; 2010.

Cardiac monitors, heart rate meters, and alarms. American National Standards Institute. Assoc. for the Advancement of Medical Instrumentation. ANSI/AAMI EC13:2002. 6 May 2002.

Castiglioni P, Piccini L, Rienzo MDi. Interpolation technique for extracting features from ECG signals sampled at low sampling rates. *Computers in Cardiology*. 2003;30:481-4.

Chow T, Kereiakes DJ, Bartone C, Booth T, Schloss EJ, Waller T, et al. Prognostic utility of microvolt T-wave alternans in risk stratification of patients with ischemic cardiomyopathy. *J Am Coll Cardiol*. 2006;47(9):1820-7.

Darwich A, Fokapu O. The effect of pathologic cardiac events on the spectral content of ECG. *Int Conf IEEE EMBS*. 2007. pp. 674-7.

Diagnostic electrocardiographic devices. American National Standards Institute. Assoc. for the Advancement of Medical Instrumentation. ANSI/AAMI EC11:1991/(R)2001/(R)2007. Aug. 2007.

Dozio R, Baba A, Assambo C, Burke MJ. Time based measurement of the impedance of the skin-electrode interface for dry electrode ECG recording. *Int Conf IEEE EMBS*. 2007. pp. 5001-4.

Ezenwa BM, Gupta MM, Nikforuk PN, Prasad K. A baseline tracking algorithm for drift reduction in electrocardiography. *Int Conf IEEE EMBS*. 1988. pp. 1230-2.

Fuster V, Walsh RA, Harrington RA, eds. Hurst's the heart. 13th ed. New York: McGraw-Hill; 2011.

Gholam-Hosseini H, Nazeran H. Detection and extraction of the ECG signal parameters. *Int Conf IEEE EMBS*. 1998;20(1):127-30.

Giuliani C, Burattini L. A new T-wave frequency based index for discrimination of abnormal repolarization. *Computing in Cardiology*. 2012;39:421-4.

Gold MR, Bloomfield DM, Anderson KP, El-Sherif NE, Wilber DJ, Groh WJ, et al. A comparison of T-wave alternans, signal averaged electrocardiography and programmed ventricular stimulation for arrhythmia risk stratification. *J Am Coll Cardiol*. 2000;36(7):2247-53.

Goldberger AL, Amaral LAN, Glass L, Hausdorff JM, Ivanov PCh, Mark RG, et al. PhysioBank, PhysioToolkit, and PhysioNet: Components of a new research resource for complex physiologic signals. *Circulation*. 2000;101(23):e215-e220.

Gordon LB, Appelt BK, Mitchell JW. The complex dielectric nature of the human body. *Conf on Electrical Insulation and Dielectric Phenomena, IEEE*. Oct. 1998;2:577-80.

Horowitz P, Hill W. The art of electronics. 2nd ed. New York: Cambridge UP; 1989.

Johnson DE, Johnson JR, Hilburn JL, Scott PD. Electric circuit analysis. 3rd ed. Hoboken, New Jersey: Wiley; 1999.

Khan MG. Rapid ECG interpretation. 3rd ed. Ed. Cannon CP. Contemporary cardiology. Totowa, New Jersey: Humana; 2008.

Kitchin C, Counts L. A designer's guide to instrumentation amplifiers. 3rd ed. Analog Devices. G02678-15-9/06(B). 2006.

Kop WJ, Krantz DS, Nearing BD, Gottdiener JS, Quigley JF, O'Callahan M, et al. Effects of acute mental stress and exercise on T-wave alternans in patients with implantable cardioverter defibrillators and controls. *Circulation*. 2004;109:1864-9.

LM555: Timer. National Semiconductor. Datasheet, DS007851. July 2006.

LMC6484: CMOS quad rail-to-rail input and output operational amplifier. National Semiconductor. Datasheet, DS011714. Aug. 2000.

Longo DL, Fauci AS, Kasper DL, Hauser SL, Jameson JL, Loscalzo J, eds. Harrison's principles of internal medicine. 18th ed. New York: McGraw-Hill; 2012.

LT1167: Single resistor gain programmable, precision instrumentation amplifier. Linear Technology. Datasheet, LT1167fb, rev. B. Jan. 2011.

Macfarlane PW, van Oostrom A, Pahlm O, Kligfield P, Janse M, Camm J, eds. Comprehensive electrocardiology. London: Springer-Verlag; 2011.

Malmivuo J, Plonsey R. Bioelectromagnetism: Principles and applications of bioelectric and biomagnetic fields. New York: Oxford UP; 1995.

Mancini R, ed. Op amps for everyone. 2nd ed. Boston: Newnes; 2003.

Marcus FI. Prevalence of T-wave inversion beyond v1 in young normal individuals and usefulness for the diagnosis of arrhythmogenic right ventricular cardiomyopathy/dysplasia. *Am J Cardiol*. 2005;95:1070-1.

Medical electrical equipment – part 2-47: Particular requirements for the safety, including essential performance, of ambulatory electrocardiographic systems. International Electrotechnical Commission. IEC 60601-2-47. 2001-07.

Merrill DR, Bikson M, Jefferys JGR. Electrical stimulation of excitable tissue: design of efficacious and safe protocols. *J Neurosci Meth*. 2005;141:171-98.

Mneimneh MA, Yaz EE, Johnson MT, Povinelli RJ. An adaptive Kalman filter for removing baseline wandering in ECG signals. *Computers in Cardiology*. 2006;33:253-6.

Mohrman DE, Heller LJ. Cardiovascular physiology. 7th ed. New York: McGraw-Hill; 2010.

Myles RC, Jackson CE, Tsorlalis I, Petrie MC, McMurray JJV, Cobbe SM. Is microvolt T-wave alternans the answer to risk stratification in heart failure? *Circulation*. 2007;116:2984-91.

Öberg T. A circuit for contact monitoring in electrocardiography. *IEEE Trans on Biomed Eng*. 1982;29(5):361-4.

Pandit SV. ECG baseline removal through STFT. *Int Conf IEEE EMBS*. 1996;4:1405-6.

Plonsey R, Barr RC. Bioelectricity: A quantitative approach. 3rd ed. New York: Springer; 2007.

Prutchi D, Norris M. Design and development of medical electronic instrumentation: A practical perspective of the design, construction, and test of medical devices. Hoboken, New Jersey: Wiley-Interscience; 2005.

Ruan F, Linghu R, Wang H, Zhang R, Zhou F. Human body impedance model and human age dependence of dielectric properties. *Int Conf on Antennas Propagation and EM Theory, IEEE*. 2010. pp. 718-21.

Schindler DM, Lux RL, Shusterman V, Drew BJ. Karhunen-Loève representation distinguishes ST-T wave morphology differences in emergency department chest pain patients with non-ST elevation myocardial infarction versus non-acute coronary syndrome. *J Electrocardiol*. 2007;40(6 Suppl):S145-9.

Sedra AS, Smith KC. Microelectronic circuits. 5th ed. New York: Oxford UP; 2004.

Smith DW, Nowacki D, Li JK-J. ECG T-wave monitor for potential early detection and diagnosis of cardiac arrhythmias. *Cardiovascular Eng*. 2010;10(4);201-6.

Smith JM, Clancy EA, Valeri CR, Ruskin JN, Cohen RJ. Electrical alternans and cardiac electrical instability. *Circulation*. 1988;77:110-121.

Sörnmo L. Time-varying filtering for removal of baseline wander in exercise ECGs. *Computers in Cardiology*. 1991. pp. 145-8.

[l] Stein PK, Sanghavi D, Sotoodehnia N, Siscovick DS, Gottdiener J. Association of Holter-based measures including T-wave alternans with risk of sudden cardiac death in the community-dwelling elderly: The cardiovascular health study. *J Electrocardiol*. 2010;43(3):251-9.

Thomas LJ, Clark KW, Mead CN, Ripley KL, Spenner BF, Oliver GC. Automated cardiac dysrhythmia analysis. *Proc of the IEEE*. 1979;67(9):1322-37.

Tintinalli JE, Stapczynski JS, Cline DM, Ma OJ, Cydulka RK, Meckler GD, eds. Tintinalli's emergency medicine: A comprehensive study guide. 7th ed. New York: McGraw-Hill; 2011.

Verrier RL, Klingenheben T, Malik M, El-Sherif N, Exner DV, Hohnloser SH, et al. Microvolt T-wave alternans: Physiological basis, methods of measurement, and clinical utility – Consensus guideline by international society for Holter and noninvasive electrocardiology. *J Am Coll Cardiol*. 2011;58(13):1309-24.

Ward LM, Greenwood PE. 1/f noise. *Scholarpedia*. 2007;2(12):1537.

Widmaier EP, Raff H, Strang KT. Vander's human physiology: The mechanisms of body function. 10th ed. New York: McGraw-Hill; 2006.

Winter BB, Webster JG. Driven-right-leg circuit design. *IEEE Trans BME*. 1983;30:62-6.

Appendix A – ECG Source Data

#	Data File	Source	ECG Lead	Description	Demonstrates	Source Sample Freq (Hz)	Simulation Length (sec)	Detected Avg HR (BPM)	Gender	Age
1	**MP35, Ch 3**	RU Cardio Lab	I	Ch 3 analog output of BIOPAC MP35, sent wirelessly to laptop. 60 Hz from BIOPAC preamp.	60 Hz and baseline drift	800	60	82.74	M	50
2	**MP35, Ch 3, w_steps**	RU Cardio Lab	I	Ch 3 analog output of BIOPAC MP35, sent wirelessly to laptop. 60 Hz from BIOPAC preamp.	60 Hz, baseline drift, & ~200 uV step changes @ 5, 10, 15, & 20 sec	800	60	82.74	M	50
3	**Synthetic, Normal**	Multisim	na	Synthetic ECG similar to MP35.	Control data	>/= 2 k	60	69.77	na	na
4	**Synthetic, Biphasic**	Multisim	na	Synthetic ECG with biphasic T-wave.	Biphasic T-wave behavior, with T-wave extending beyond Timer 1 window	>/= 2 k	60	69.77	na	na
5	**Synthetic, Inverted**	Multisim	na	Synthetic ECG with inverted T-wave.	Identification of inverted T-wave	>/= 2 k	60	69.77	na	na
6	**Synthetic, Elevated ST**	Multisim	na	Synthetic ECG with elevated ST.	Positive slope starting within Timer 2 window	>/= 2 k	60	69.77	na	na
7	**APNEAa02er, Minute 79**	PhysioBank	?	Sleep apnea patient	T-wave changes in low oxygen conditions and low amplitude R-waves	100	60	79.31	?	?
8	**APNEAa02er, Minute 85**	PhysioBank	?	Sleep apnea patient	T-wave changes in low oxygen conditions	100	60	77.22	?	?
9	**CHALL2011SETA1002867**	PhysioBank	II	A few types of T-waves in a 10 sec file. Repeated twice in the simulation.	Adaptation to changing T-wave morphologies	500	20	66.31	?	?
10	**CUDBcu17, Minute 5**	PhysioBank	?	Short ST with ventricular fibrillation near end of record. **Needed to adjust Timer 1, Timer 2, & Timer 3 for this record.	Wide QRS and very dynamic T-wave morphology	250	43	90.53	?	?
11	**EDBe0406, Minute 92**	PhysioBank	MLI	Tachycardia, premature beats, T-wave change, depressed ST	Ability to track fast heart with depressed ST segment	250	60	104.67	M	45
12	**EDBe0406, Minute 117**	PhysioBank	MLI	Tachycardia, premature beats, T-wave change, depressed ST	Ability to track fast heart with depressed ST segment	250	60	69.91	M	45
13	**EDBe0409, Minute 94**	PhysioBank	MLI	Tachycardia, depressed ST segment	Ability to track very fast heart with depressed ST segment	250	60	123.25	M	71
14	**EDBe0409, Minute 119**	PhysioBank	MLI	Tachycardia, depressed ST segment	Ability to track very fast heart with depressed ST segment	250	60	135.54	M	71
15	**FANTASIAf1y01, Minute 3**	PhysioBank	MLI	ECG of young, healthy female	Control data	250	60	79.53	F	23
16	**FANTASIAf1y04, Minute 13**	PhysioBank	?	ECG of young, healthy male	Control data. Very slow heart rate.	250	60	46.12	M	31
17	**FANTASIAf2o02, Minute 13**	PhysioBank	?	ECG of older, healthy female	Control data	250	60	55.58	F	75
18	**FANTASIAf2o03, Minute 11**	PhysioBank	?	ECG of older, healthy female	Control data	250	60	56.48	F	85
19	**FANTASIAf2o07, Minute 4**	PhysioBank	?	ECG of older, healthy male	Control data	250	60	50.18	M	77

ECG Source Data, continued

#	Data File	Source	ECG Lead	Description	Demonstrates	Source Sample Freq (Hz)	Simulation Length (sec)	Detected Avg HR (BPM)	Gender	Age
20	**Holter, Start at 25 s**	Univ. of Rochester	MLII	Holter monitor recording with lots of noise artifacts	Holter monitor ECG problems	200	60	74.98	?	?
21	**Holter, Start at 150 s**	Univ. of Rochester	MLII	Holter monitor recording with much less noise artifacts than other sections	Holter monitor ECG problems	200	60	47.54	?	?
22	**LTSTDBs20061, Minute 2232**	PhysioBank	MLII	Tachycardia, depressed ST segment ("ST scooping")	Ability to track very fast heart with depressed ST segment	250	60	113.65	F	33
23	**LTSTDBs20081, Minute 51**	PhysioBank	MLII	Long-term ST database example	Response to premature ventricular contractions (PVCs)	250	60	81.83	F	39
24	**LTSTDBs20101, Minute 1054**	PhysioBank	MLII	Long-term ST database example with regular PVCs	Response to premature ventricular contractions (PVCs)	250	60	64.78	F	62
25	**LTSTDBs20121, Minute 19**	PhysioBank	MLII	Long-term ST database example with regular PVCs & extreme ST depression	Response to premature ventricular contractions (PVCs) & extreme ST depression	250	60	82.83	F	48
26	**LTSTDBs20141, Minute 1615**	PhysioBank	MLII	Long-term ST database example with rate-related T-wave episodes and ST depression	Dynamic T-wave morphology & ST depression	250	60	105.90	F	35
27	**LTSTDBs30661, Minute 1452**	PhysioBank	MLII	Long-term ST database example with ectopic beats and R-on-T episodes	Effect of stated arrhythmias on T-wave	250	60	127.04	M	72
28	**MITDB108, Minute 4**	PhysioBank	MLII	Long QT syndrome, with large amounts of noise and baseline drift. Tall P-wave (creates false triggers) and sometimes inverted (more dominant downward) R-wave. One PVC. **Needed to adjust Timer 1 for this record.	Baseline drift correction	360	60	56.05	F	87
29	**PTBDBpat046s0161lre, Minute 1**	PhysioBank	MLII	Inverted R-wave and large amounts of baseline drift	Response to inverted R-wave & baseline drift correction	1000	60	99.05	F	64
30	**QTDBsel114, Minute 3**	PhysioBank	MLII	ST depression and uniform PVCs	Response to stated arrhythmias	250	60	66.79	F	72
31	**TWADBtwa25**	PhysioBank	II	Synthetic ECG with T-wave alternans. Note that ST time is very short. **Needed to adjust Timer 1, Timer 2, & Timer 3 for this record.	Ability to measure alternans	500	120	123.63	na	na
32	**TWADBtwa81**	PhysioBank	II	Synthetic ECG without T-wave alternans. Note that ST time is very short. **Needed to adjust Timer 1, Timer 2, & Timer 3 for this record.	Control data	500	120	126.47	na	na

Appendix B – MATLAB® Code: Inversion and Slopes

```
% Find the local maximum & minimum value of the slope signal inside the
% tWin windows (Timer 1 On, Timer 2 Off).

l = 1; % l = row index of slopeXXXData. 1 per min detect.
m = find(tWin(:,1),1,'first'); % m = lwr row index of tWin (or start
index)
for k = m:find(tWin(:,1),1,'last') % k <= upr row index of tWin window
    if tWin(k,2) ~= 0 % If Timer 1 is On & Timer 2 is Off,
        if m > 1 % Ensure can do k-1 index in next 'if' statement
            if tWin(k-1,2) == 0 % If previous tWin value = 0,
                m = k; % Set m = lower index of this tWin window
            end
        end
        if k < size(slope,1) % Ensure can do k+1 index in next 'if'
            if tWin(k+1,2) == 0 % If next Timer 2 Off value = 0,
                % Setting slope search windows away from tWin edges to
                % better ignore noise (motion artifacts, etc.).

                % Find duration of this tWin window.
                winTime = sigAdj(k,1) - sigAdj(m,1);
                % Find the index of the positive tPeaks.
                pPeak = find(slope(:,1) == tPeakMaxData(l,1));
                % lwr limit of slope search win
                lwrLim = find(sigAdj(:,1) <= ...
                    (sigAdj(m,1) + 0.05 * winTime),1,'last');
                % lower mid1 of slope search windows
                mid1 = find(sigAdj(:,1) <= ...
                    (sigAdj(m,1) + 0.25 * winTime),1,'last');
                % lower mid2 of slope search windows
                mid2 = find(sigAdj(:,1) <= ...
                    (sigAdj(m,1) + 0.45 * winTime),1,'last');
                % upper mid3 of slope search windows
                mid3 = find(sigAdj(:,1) >= ...
                    (sigAdj(m,1) + 0.55 * winTime),1,'first');
                % upper mid4 of slope search windows
                mid4 = find(sigAdj(:,1) >= ...
                    (sigAdj(m,1) + 0.75 * winTime),1,'first');
                % upper limit of slope search windows
                uprLim = find(sigAdj(:,1) >= ...
                    (sigAdj(m,1) + 0.95 * winTime),1,'first');

                % Trying to determine if T-wave is up (normal) or down
                % (inverted) and ignore noise errors (spikes in diff
                % data).
                if ((mean(slope(lwrLim:mid2,2)) >= 0) && ...
                        (mean(slope(lwrLim:mid2,2)) >= ...
                        mean(slope(mid3:uprLim,2)))) || ...
                        ...
                        ((mean(slope(mid1:mid2,2)) >= 0) && ...
                        (mean(slope(mid1:mid2,2)) >= ...
                        mean(slope(mid3:mid4,2)))) || ...
                        ...
                        (sigAdj(mid2,2) >= sigAdj(lwrLim,2) && ...
                        sigAdj(mid3,2) >= sigAdj(uprLim,2)) || ...
```

```
    ...
    min(slope(lwrLim:uprLim,2) >= 0) || ...
    ...
    ((mean(slope(lwrLim:pPeak,2)) >= ...
    mean(slope(pPeak:uprLim,2))) && ...
    (mean(slope(lwrLim:mid1,2)) >= ...
    mean(slope(mid2:mid4,2)))) || ...
    ...
    ((mean(slope(lwrLim:pPeak,2)) >= ...
    mean(slope(pPeak:uprLim,2))) && ...
    (mean(slope(lwrLim:mid2,2)) >= ...
    mean(slope(mid3:uprLim,2)))) || ...
    ...
    ((mean(slope(lwrLim:pPeak,2)) >= ...
    mean(slope(pPeak:uprLim,2))) && ...
    (mean(slope(mid1:mid3,2)) >= ...
    mean(slope(mid4:uprLim,2))))

% If the pos T-peak is between the lower & upper
  limits
if ((find(slope(:,1) == tPeakMaxData(l,1)) >=
    lwrLim) ...
    && (find(slope(:,1) == tPeakMaxData(l,1)) ...
        <= uprLim))

   % set the middle index to the tPeakMax.
    mid = find(slope(:,1) == tPeakMaxData(l,1));
else
    % else set the middle index to lower mid2.
    mid = mid2;
end
% If T-wave is in the middle of a valley, ...
if ((mean(slope(mid1:mid2,2)) >= 0) && ...
    (mean(slope(mid1:mid2,2)) >= ...
    mean(slope(mid3:mid4,2))))

    % else set the middle index to lower mid2.
    mid = mid2;
end
% If the slope is always <= 0 in the lower window
% section, set the middle index to the upper mid.
if max(slope(lwrLim:mid,2)) <= 0 && mid == mid2
    mid = mid3;
end
% If the slope is always <= 0 in the lower & upper
% mid window sections, set the middle index to the
% upper limit.
if max(slope(lwrLim:mid,2)) <= 0
    mid = uprLim;
end
% p = row index of max slope in 1st window section.
p = (lwrLim - 1) + find(slope(lwrLim:mid,2) == ...
    max(slope(lwrLim:mid,2)),1,'first');
% n = row index of min slope in 2nd search window.
if ((min(slope(mid:uprLim,2)) < 0) && ...
        (min(slope(mid:uprLim,2)) < slope(p,2)))
    n = (mid - 1) + find(slope(mid:uprLim,2) == ...
```

```
                        min(slope(mid:uprLim,2)),1,'first');
                    else
                        n = (lwrLim - 1) + ...
                            find(slope(lwrLim:uprLim,2) == ...
                            min(slope(lwrLim:uprLim,2)),1,'first');
                    end
                    % Store slope time & amplitude data
                    slopeMaxData(l,:) = slope(p,:);
                    slopeMinData(l,:) = slope(n,:);
                else
                    % Else T-wave is inverted and ...
                    if ((find(slope(:,1) == tPeakMinData(l,1)) >=
                        lwrLim) ...
                            && (find(slope(:,1)==tPeakMinData(l,1)) ...
                            <= uprLim))

                        mid = find(slope(:,1) == tPeakMinData(l,1));
                    else
                        mid = mid2;
                    end
                    if ((mean(slope(mid1:mid2,2)) < 0) && ...
                        (mean(slope(mid1:mid2,2)) <= ...
                        mean(slope(mid3:mid4,2))))

                        mid = mid2;
                    end
                    if min(slope(lwrLim:mid,2)) >= 0 && mid == mid2
                        mid = mid3;
                    end
                    if min(slope(lwrLim:mid,2)) >= 0
                        mid = uprLim;
                    end
                    % n = row index of min slope in 1st search window).
                    n = (lwrLim - 1) + find(slope(lwrLim:mid,2) == ...
                        min(slope(lwrLim:mid,2)),1,'first');
                    % p = row index of max slope in 2nd search window.
                    if ((max(slope(mid:uprLim,2)) >= 0) && ...
                        (max(slope(mid:uprLim,2)) > slope(n,2)))

                        p = (mid - 1) + find(slope(mid:uprLim,2) == ...
                            max(slope(mid:uprLim,2)),1,'first');
                    else
                        p = (lwrLim - 1) + ...
                            find(slope(lwrLim:uprLim,2) == ...
                            max(slope(lwrLim:uprLim,2)),1,'first');
                    end
                    % Store slope time & amplitude data
                    slopeMaxData(l,:) = slope(p,:);
                    slopeMinData(l,:) = slope(n,:);
                end
                l = l + 1;
            end
        end
    end
end
```

Appendix C – MATLAB® Code: Composite Base

```
% Finds the base ("zero") of T-wave as the min/max of the signal
% between the T-wave peak (max/min) and the end of the T-wave window.

for k = 1:size(tZeroData,1) % k = row of data

    % If pos slope occurred before neg slope (non-inverted T),
    if slopeMaxReal(k,1) <= slopeMinReal(k,1)

        % Set lower time limit to = time of tPeakMaxData.
        lwrLim = tPeakData(k,1);
        % Set upper time limit to = time of timer1EdgeDnData - 2 ms.
        uprLim = timer1EdgeDnData(k,1) - 0.002;

        % Ensure that uprLim is >= lwrLim
        if uprLim < lwrLim
            uprLim = lwrLim;
        end

        % Find indices of lower and upper time limits in adjusted sig.
        minInd = find(sigAdj(:,1) >= lwrLim, 1, 'first');
        maxInd = find(sigAdj(:,1) <= uprLim, 1, 'last');
        % Find index of local min (from min to max index) of adjusted
        % signal.
        ind = (minInd - 1) + find(sigAdj(minInd:maxInd,2) == ...
            min(sigAdj(minInd:maxInd,2)),1,'first');
        % Create T-zero data using adjusted signal time value & local
        % min amplitude.
        tZeroData(k,:) = sigAdj(ind,:);
    end

    % If positive slope occurred after negative slope (inverted T), ...
    % otherwise, logic similar to that above.
    if slopeMaxReal(k,1) > slopeMinReal(k,1)

        lwrLim = tPeakData(k,1);
        uprLim = timer1EdgeDnData(k,1) - 0.002;

        if uprLim < lwrLim
            uprLim = lwrLim;
        end

        minInd = find(sigAdj(:,1) >= lwrLim, 1, 'first');
        maxInd = find(sigAdj(:,1) <= uprLim, 1, 'last');
        ind = (minInd - 1) + find(sigAdj(minInd:maxInd,2) == ...
            max(sigAdj(minInd:maxInd,2)),1,'first');
        tZeroData(k,:) = sigAdj(ind,:);
    end
end
```

Appendix D – MATLAB® Code: Composite Area

```
% Calculate area of composite T-wave (mV-sec), using a trapezoid,
% rectangle, trapezoid geometric summation.

l = 1; % l = row index of slope lines & composite area. 1 per cycle.
m = 2; % m = col of slope line y-value (amplitude). 4 per cycle.
for k = 1:2:(size(tPeakLines,2)-1) % k = col of line data. 2 per cycle.

    % If positive slope occurred before negative slope (non-inverted T)
    if slopeMaxReal(l,1) <= slopeMinReal(l,1)
        % min height of pos slope line (lead)
        h1 = abs(min(slopeLinesTrim(:,m)) - tZeroLines(1,k+1));
        if isnan(h1)
            h1 = abs(tPeakLines(1,k+1));
        end
        % max hght of T-wave
        h2 = abs(tPeakLines(1,k+1) - tZeroLines(1,k+1));
        % min height of neg slope line(lag)
        h3 = abs(min(slopeLinesTrim(:,m+2)) - tZeroLines(1,k+1));
        if isnan(h3)
            h3 = abs(tPeakLines(1,k+1));
        end
        t1 = min(tZeroLines(:,k)); % start time of T-wave figure
        % time when pos slope line meets T-peak
        t2 = min(tPeakLines(:,k));
        if t2 < t1
            t2 = t1;
        end
        % time when neg slope line meets T-peak
        t3 = max(tPeakLines(:,k));
        if t3 < t2
            t3 = t2;
        end
        t4 = max(tZeroLines(:,k)); % end time of T-wave figure
        if t4 < t3
            t4 = t3;
        end
        area1 = 0.5 * (h1 + h2) * (t2 - t1); % area of trapezoid 1
        area2 = h2 * (t3 - t2); % area of rectangle
        area3 = 0.5 * (h2 + h3) * (t4 - t3); % area of trapezoid 2
        areaComp(l,2) = area1 + area2 + area3; % total composite area
        areaComp(l,1) = areaMaxData(l,1); % time from max area data
    end

    % If positive slope occurred after negative slope (inverted T), ...
    % otherwise logic is similar to above.
    if slopeMaxReal(l,1) > slopeMinReal(l,1)
        % max height of neg slope line(lead)
        h1 = abs(tZeroLines(1,k+1) - max(slopeLinesTrim(:,m+2)));
        if isnan(h1)
            h1 = abs(tPeakLines(1,k+1));
        end
        % max hght of T-wave
        h2 = (tZeroLines(1,k+1) - tPeakLines(1,k+1));
```

```
        % max height of pos slope line (lag)
        h3 = abs(tZeroLines(1,k+1) - max(slopeLinesTrim(:,m)));
        if isnan(h3)
            h3 = abs(tPeakLines(1,k+1));
        end
        t1 = min(tZeroLines(:,k));
        t2 = min(tPeakLines(:,k));
        if t2 < t1
            t2 = t1;
        end
        t3 = max(tPeakLines(:,k));
        if t3 < t2
            t3 = t2;
        end
        t4 = max(tZeroLines(:,k));
        if t4 < t3
            t4 = t3;
        end
        area1 = 0.5 * (h1 + h2) * (t2 - t1);
        area2 = h2 * (t3 - t2);
        area3 = 0.5 * (h2 + h3) * (t4 - t3);
        areaComp(l,2) = -(area1 + area2 + area3);
        areaComp(l,1) = areaMinData(l,1);
    end

    l = l + 1;
    m = m + 4;
end

if ~isempty(tEdgeStart)
    % Find the first areaComp entry that follows the tEdgeStart time
    % and add it as third and fourth column entries.
    for k = 1:size(tEdgeStart,1)
        tEdgeStart(k,3:4) = ...
            areaComp(find(areaComp(:,1)>=tEdgeStart(k,1),1,'first'),:);
    end
end

if ~isempty(tEdgeEnd)
    % Find the last areaComp entry that precedes the tEdgeEnd time and
    % add it as third and fourth column entries.
    for k = 1:size(tEdgeEnd,1)
        tEdgeEnd(k,3:4) = ...
            areaComp(find(areaComp(:,1) <= tEdgeEnd(k,1),1,'last'),:);
    end
end
```

Appendix E – MATLAB® Code: Transient Trigger Filter

```
% Eliminate data from transient (non-R-wave) triggers

% Create data copies for filtered results
rPeakMaxDataFilt = rPeakMaxData;
rPeakMinDataFilt = rPeakMinData;
tPeakDataFilt = tPeakData;
tPeakMaxDataFilt = tPeakMaxData;
tPeakMinDataFilt = tPeakMinData;
areaCompFilt = areaComp;
areaMaxRealAdjFilt = areaMaxRealAdj;
areaMinRealAdjFilt = areaMinRealAdj;
areaNetRealFilt = areaNetReal;
slopeMaxRealFilt = slopeMaxReal;
slopeMinRealFilt = slopeMinReal;
tZeroDataFilt = tZeroData;
timer1EdgeDnDataFilt = timer1EdgeDnData;
timer1EdgeUpDataFilt = timer1EdgeUpData;
timer2EdgeDnDataFilt = timer2EdgeDnData;
tPeakLinesFilt = tPeakLines;
tZeroLinesFilt = tZeroLines;
slopeLinesFilt = slopeLines;
slopeLinesTrimFilt = slopeLinesTrim;
tPeakCalcFilt = tPeakCalc;
trRatioMaxFilt = trRatioMax;
trRatioEnvFilt = trRatioEnv;

% Define thresholds for R & T-waves (events outside threshold ignored)
rThresh1 = 10;
rThresh2 = 10;
rThresh3 = 0.15;
tThresh1 = 2;
tThresh2 = 2;

% Find indices of values above or below threshold
indRmax = find(abs(rPeakMaxData(:,2)) >= rThresh1);
indRmin = find(abs(rPeakMinData(:,2)) >= rThresh1);
indRenvMax = find(abs(rPeakMaxData(:,2)-rPeakMinData(:,2))>=rThresh2);
indRenvMin = find(abs(rPeakMaxData(:,2)-rPeakMinData(:,2))<=rThresh3);
indTmax = find(abs(tPeakMaxData(:,2)) >= tThresh1);
indTmin = find(abs(tPeakMinData(:,2)) >= tThresh1);
indTenvMax = find(abs(tPeakMaxData(:,2)-tPeakMinData(:,2))>=tThresh2);

for l = 1:size(rPeakMaxData,1)

    % If counter l matches any of the indices, zero/NaN that row
    if          any(l == indRmax) ...
            || any(l == indRmin) ...
            || any(l == indRenvMax) ...
            || any(l == indRenvMin) ...
            || any(l == indTmax) ...
            || any(l == indTmin) ...
            || any(l == indTenvMax)
```

```
            rPeakMaxDataFilt(l,:) = 0;
            rPeakMinDataFilt(l,:) = 0;
            tPeakDataFilt(l,:) = 0;
            tPeakMaxDataFilt(l,:) = 0;
            tPeakMinDataFilt(l,:) = 0;
            areaCompFilt(l,:) = 0;
            areaMaxRealAdjFilt(l,:) = 0;
            areaMinRealAdjFilt(l,:) = 0;
            areaNetRealFilt(l,:) = 0;
            slopeMaxRealFilt(l,:) = 0;
            slopeMinRealFilt(l,:) = 0;
            tZeroDataFilt(l,:) = 0;
            timer1EdgeDnDataFilt(l,:) = 0;
            timer1EdgeUpDataFilt(l,:) = 0;
            timer2EdgeDnDataFilt(l,:) = 0;
            tPeakLinesFilt(:,((2*l-1):(2*l))) = 0;
            tZeroLinesFilt(:,((2*l-1):(2*l))) = 0;
            slopeLinesFilt(:,((4*l-3):(4*l))) = 0;
            slopeLinesTrimFilt(:,((4*l-3):(4*l))) = 0;
            tPeakCalcFilt(l) = NaN;
            trRatioMaxFilt(l) = NaN;
            if l >= threeSecR
                trRatioEnvFilt(l-threeSecR+1) = NaN;
            end
        end
    end

    % Remove non-value (zeros/NaN in all columns) entries from data.
    rPeakMaxDataFilt(all(rPeakMaxDataFilt == 0,2),:) = [];
    rPeakMinDataFilt(all(rPeakMinDataFilt == 0,2),:) = [];
    tPeakDataFilt(all(tPeakDataFilt == 0,2),:) = [];
    tPeakMaxDataFilt(all(tPeakMaxDataFilt == 0,2),:) = [];
    tPeakMinDataFilt(all(tPeakMinDataFilt == 0,2),:) = [];
    areaCompFilt(all(areaCompFilt == 0,2),:) = [];
    areaMaxRealAdjFilt(all(areaMaxRealAdjFilt == 0,2),:) = [];
    areaMinRealAdjFilt(all(areaMinRealAdjFilt == 0,2),:) = [];
    areaNetRealFilt(all(areaNetRealFilt == 0,2),:) = [];
    slopeMaxRealFilt(all(slopeMaxRealFilt == 0,2),:) = [];
    slopeMinRealFilt(all(slopeMinRealFilt == 0,2),:) = [];
    tZeroDataFilt(all(tZeroDataFilt == 0,2),:) = [];
    timer1EdgeDnDataFilt(all(timer1EdgeDnDataFilt == 0,2),:) = [];
    timer1EdgeUpDataFilt(all(timer1EdgeUpDataFilt == 0,2),:) = [];
    timer2EdgeDnDataFilt(all(timer2EdgeDnDataFilt == 0,2),:) = [];
    tPeakLinesFilt(:,all(tPeakLinesFilt == 0,1)) = [];
    tZeroLinesFilt(:,all(tZeroLinesFilt == 0,1)) = [];
    slopeLinesFilt(:,all(slopeLinesFilt == 0,1)) = [];
    slopeLinesTrimFilt(:,all(slopeLinesTrimFilt == 0,1)) = [];
    tPeakCalcFilt(all(isnan(tPeakCalcFilt),2),:) = [];
    trRatioMaxFilt(all(isnan(trRatioMaxFilt),2),:) = [];
    trRatioEnvFilt(all(isnan(trRatioEnvFilt),2),:) = [];
```